S2
Sinta Score

e-ISSN 2503-5010
p-ISSN 2087-0965

Accredited by Ristekdikti: Nomor 158/E/KPT/2021

JURNAL RISET TEKNOLOGI PENCEGAHAN PENCEMARAN INDUSTRI

Research Journal of Industrial Pollution Prevention Technology

Vol. 14, No. 1, May 2023

JURNAL RISET Teknologi Pencegahan Pencemaran Industri	Vol.14	No. 1	Page 1 - 52	Semarang, May 2023	ISSN No. 2087-0965

Kementerian Perindustrian
REPUBLIK INDONESIA

Published by :
BADAN STANDARDISASI DAN KEBIJAKAN JASA INDUSTRI
BALAI BESAR STANDARDISASI DAN PELAYANAN JASA PENCEGAHAN PENCEMARAN INDUSTRI

Jurnal Riset
Teknologi Pencegahan Pencemaran Industri

Volume 14 No. 1, May 2023

FOCUS AND SCOPE

Jurnal Riset Teknologi Pencegahan Pencemaran Industri (Research Journal of Industrial Pollution Prevention Technology) seeks to promote and disseminate original research as well as review, related to following area:

Environmental Technology : within the area of air pollution technology, wastewater treatment technology, and management of solid waste and harzardous toxic substance.

Process Technology and Simulation : technology and/or simulation in industrial production process aims to minimize waste and environmental degradation.

Design Engineering : device engineering to improve process efficiency, measurement accuracy and to detect pollutant.

Material Fabrication : environmental friendly material fabrication as subtitution material for industry.

Energy Conservation : process engineering/ technology/ conservation of resources for energy generation.

ENSURED EDITOR

Dr. Sidik Herman, S.Sn., M.M.
Center for Standardization and Industrial Pollution Prevention Services

DIRECTOR

Dedy Widya Asiyanto, S.Si, M.Si.
Center for Standardization and Industrial Pollution Prevention Services
Any Kurnia, S.Si, M.Si.
Center for Standardization and Industrial Pollution Prevention Services

CHIEF EDITOR

Ikha Rasti Julia Sari, S.T., M.Si.
Center for Standardization and Industrial Pollution Prevention Services

PEER REVIEWER

Prof. Dr. Ir. Eddy Hermawan, M.Sc.
National Research and Innovation Agency
Prof. Dr.rer,nat. Karna Wijaya, M.Eng.
Gadjah Mada University
Prof. Dr. Ir. Purwanto, Dipl.EP., DEA
Diponegoro University
Prof. Tutuk Djoko Kusworo, S.T., M.Eng., Ph.D.
Diponegoro University
Prof. Puji Lestari, Ph.D.
Bandung Institute of Technology
Prof. Dr. Ir. Yunardi, MASc
Syiah Kuala University
Prof. Dr. Yuli Yetri M.Si
State Polytechnic of Padang
Dr. Ir. Edwan Kardena
Bandung Institute of Technology
Dr. Qomarudin Helmy, S.Si., M.T.
Bandung Institute of Technology
Dr. Haryono Setiyo Huboyo, S.T., M.T.
Diponegoro University
Dr. Oman Zuas
National Research and Innovation Agency
Dr. Moch. Arief Albachrony, M.Sc.Tech
National Research and Innovation Agency
Dr. Gerson N Njurumana, S.Hut., M.Sc.
National Research and Innovation Agency
Dr. Ir. Nani Harihastuti, M.Si.
National Research and Innovation Agency
Dr. Aris Mukimin. S.Si., M.Si.
National Research and Innovation Agency
Dr. Linda Hevira, M.Si.
University of Mohammad Natsir
Dr. Ir. Ratnawati, M.Eng.Sc., IPM
Indonesian Institute of Technology
Alex Lukmanto Suherman, MRSC, D. Phil
Ministry of Health Republic of Indonesia

Ir. Nilawati
National Research and Innovation Agency

Moch. Syarif Romadhon, S.Si., M.Sc.
National Research and Innovation Agency

Bekti Marlena, S.T., M.Si.
Center for Standardization and Industrial Pollution Prevention Services

Rame, S.Si., M.Si.
Center for Standardization and Industrial Pollution Prevention Services

Novarina I. Handayani, S.Si., M.Si.
Center for Standardization and Industrial Pollution Prevention Services

Ir. Nasuka, M.M.
Center for Standardization and Industrial Pollution Prevention Services

Januar Arif Fatkhurrahman S.T., M.T.
Center for Standardization and Industrial Pollution Prevention Services

Rustiana Yuliasni, S.T., M.Sc.
National Research and Innovation Agency

Silvy Djayanti, S.T., M.Si.
National Research and Innovation Agency

Hanny Vistanty, S.T., M.T.
National Research and Innovation Agency

Nanik Indah Setianingsih, S.TP., M.Ling.
National Research and Innovation Agency

Evana Yuanita, S.T., M.T.

Center for Standardization and Services of Chemical, Pharmaceutical and Packaging Industries

Ella Kusumastuti, S.Si., M.Si.

Universitas Negeri Semarang

Jurnal Riset

Teknologi Pencegahan Pencemaran Industri

Volume 14 No. 1, May 2023

IMPRINT

JRTPPI published by Center for Standardization and Industrial Pollution Prevention Services (BBSPJPPI) – Agency for Standardization and Industrial Services (BSKJI), Ministry of Industry. JRTPPI is published online twice in every year.
ISSN print edition : 2087-0965
ISSN electronic edition : 2503-5010
Electronic edition available on :
ejournal.kemenperin.go.id/jrtppi

INDEXING

JRTPPI has been covered by these following indexing services :
Crossref, Indonesian Scientific Journal Database (ISJD), Mendeley, Infobase Index, Indonesian Publication Index (IPI), Bielefeld Academic Search Engine (BASE), Google Scholar, Directory of Research Journals Indexing (DRJI).

MAILING ADDRESS

Center for Standardization and Industrial Pollution Prevention Services.
Jl. Ki Mangunsarkoro No. 6 Semarang, Central Java, 50136 Indonesia.
Telp. +62 24 8316315
Fax. +62 24 8414811
e-mail: jurnalrisettppi@kemenperin.go.id
Working hour : Monday - Friday
07.30 – 16.00 GMT+7

EDITORIAL BOARD

Drs. Krus Haryanto, M.Si.
Center for Standardization and Industrial Pollution Prevention Services
Ericha Fatma Yuniati, S.T., M.T.
Center for Standardization and Industrial Pollution Prevention Services
Agus Purwanto, S.T., M.Ling.
Center for Standardization and Industrial Pollution Prevention Services
Farida Crisnaningtyas, S.T., M.Eng.
Center for Standardization and Industrial Pollution Prevention Services
Rizal Awaludin Malik, S.Si., M.Si.
Center for Standardization and Industrial Pollution Prevention Services
Adi Prasetio, S.Si.
Center for Standardization and Industrial Pollution Prevention Services
Ningsih Ika Pratiwi, S.T.
Center for Standardization and Industrial Pollution Prevention Services
Yose Andriani, S.T.
Center for Standardization and Industrial Pollution Prevention Services

MANAGING EDITOR

Nur Zen, S.T., M.T.
Center for Standardization and Industrial Pollution Prevention Services
Erwin Setya Kurnaiawan, S.T.
Center for Standardization and Industrial Pollution Prevention Services

COPY EDITOR

Sidqi Ahmad, S.Si.
Center for Standardization and Industrial Pollution Prevention Services
Abinubli Tariswafi Mawarid, S.Si.
Center for Standardization and Industrial Pollution Prevention Services
Charis Achmad Tajuddin, S.T.
Center for Standardization and Industrial Pollution Prevention Services

LAYOUT EDITOR

Surya Aji Prassetya, S.T.
Center for Standardization and Industrial Pollution Prevention Services
Nur Hamid, S.Si.
Center for Standardization and Industrial Pollution Prevention Services

PROOFREADER

Charis Achmad Tajuddin, S.T.
Center for Standardization and Industrial Pollution Prevention Services
Surya Aji Prassetya, S.T.
Center for Standardization and Industrial Pollution Prevention Services

Jurnal Riset

Teknologi Pencegahan Pencemaran Industri

Volume 14 No. 1, May 2023

PREFACE

Thanks to Allah, the Most Gracious and Most Merciful, the Journal of Industrial Pollution Prevention Technology (JRTPPI) has published its 14th volume, first edition. This journal contains scientific articles, particularly in the fields of environmental technology, process technology and simulation, design engineering, material fabrication, and energy conservation. We would like to express our sincere appreciation to the head of the Center for Standardization and Industrial Pollution Prevention Services, Ministry of Industry, for their continuous support of JRTPPI. We also extend our gratitude to the authors, editorial board, and reviewers who have actively participated in maintaining the consistency of quality and timely publication.

This edition consists of five full-text English scientific articles. This is part of the editorial board's commitment to improving the authors' performance in delivering the results of their research and making it easily accessible to a broader audience to increase the number of citations. This policy is also aimed at realizing our goal of JRTPPI being a globally indexed international journal.

The articles in this edition include a study on low-cost instruments to monitor Sulphur Dioxide emissions based on the DOAS method, a study on pH-electrodeposition-dependant Iron Oxide towards the physicochemical characteristics and electrochemical performance in biorefractory pollutant degradation, the impact of reduced activator concentration and curing method on the compressive strength of metakaolin/fly ash-based geopolymer mortar, an evaluation of diesel engine performance using biodiesel from cooking oil waste, and the potential of biodiesel production from locally used frying oil through the electrocatalysis method. These five manuscripts were accepted and published in this edition from researchers and lecturers in Indonesia. The submission, review, and editing process for these manuscripts ranged from 1 to 6 months.

Hopefully, these scientific articles will provide new knowledge and experiences for readers in academia, research, industry, and society at large. We realize that nothing is perfect until all parties have continuously improved.

Semarang, May 2023

Chief Editor

Jurnal Riset
Teknologi Pencegahan Pencemaran Industri
Volume 14 No. 1, May 2023

TABLE OF CONTENT

Jurnal Riset
Teknologi Pencegahan Pencemaran Industri
Volume 14 No. 1, May 2023

ABSTRACT

Nur Zen*[1,2], Haryono Setiyo Huboyo[1], Moch. Syarif Romadhon[3,4], Januar Arif Fatkhurrahman[2], Sidna Kosim Amrulah[2]

([1]Department of Environmental Engineering, Diponegoro University
[2]Center for Standardization and Industrial Pollution Prevention Services
[3]National Research and Innovation Agency
[4]Atmospheric, Oceanic and Planetary Physics Department, University of Oxford)

A Low-Cost Instrument to Monitor Sulphur Dioxide Emissions Based on The DOAS Method

Jurnal Riset Teknologi Pencegahan Pencemaran Industri, May 2023, Vol. 14, No. 1, p. 1-7, 5 ill, 1 tab, 15 ref

Various techniques to measure SO_2 concentration based on Differential Optical Absorption Spectroscopy (DOAS) have been widely developed and applied for various measurements. However, most of the applications are still relatively expensive. Some efforts have been made to reduce the cost by using Ultraviolet Light Emitting Diodes (LEDs) as light sources, showing promising results. Further reductions can be possibly made by providing an alternative to replace high spectral resolution spectrometers widely used in DOAS applications since those spectrometers are commercially expensive. This paper studies the feasibility of a DOAS instrument using a low-cost spectrometer and UV-LEDs as light sources. The resolution of the spectrometer is 0.7 nm. With this resolution, it is expected that the instrument hardly captures narrow band structures of SO_2 optical absorption in the spectral range between 280 nm and 320 nm when measuring SO_2 gas concentration lower than the limits of SO_2 emissions regulated by the Indonesian government. To compensate for this drawback, narrow and broad bands of optical absorption structures are considered in the data analysis to achieve a detection limit far below the regulated limits. To capture the broadband structures, four UV-LEDs are used to cover spectral absorption from 250 nm to 320 nm. The instrument was calibrated using eight different standard concentrations of SO_2. The correlation between the readings and the standard concentrations is high, indicated by the Pearson correlation coefficient of 0.9999. It was also found that the lowest concentration the instrument can distinguish from blank samples or the Limit of Detection is 16 ppm. However, the instrument can precisely measure concentrations higher than or equal to 25 ppm with a standard deviation of less than 10% of the mean concentration measured from five measurements. This is far below the required legal limits, below 229 ppm. After the calibration, the DOAS instrument was used to measure SO_2 sampled from the emission of burning coals. To compare, a commercial SO_2 sensor was used to measure the same gas. The results indicate that the difference in the readings between the two instruments is around 6% of the concentration.

(Author)

Keywords: DOAS, Emission, Sulphur Dioxide

Widya Ernayati Kosimaningrum*[1,2], Heri Heriyanto[1], Meri Yulvianti[1], Alia Badra Pitaloka[1,3], Muhammad Raja Najahtama[1], Muhammad Aditya Wibisana[1], Yulis Sutianingsih[4]

([1]Chemical Engineering Department, Faculty of Engineering, Universitas Sultan Ageng Tirtayasa, Cilegon 42435, Banten, Indonesia
[2]Center for Local Food Innovation, PUI-PT, Universitas Sultan Ageng Tirtayasa, Serang, Banten, Indonesia
[3]Biomass Valorization Laboratory, Center of Excellence, Faculty of Engineering, Universitas Sultan Ageng Tirtayasa, Cilegon 42435, Banten, Indonesia
[4]Magister of Chemical Engineering Department, Faculty of Engineering, Universitas Sultan Ageng Tirtayasa, Cilegon 42435, Banten, Indonesia)

The pH-electrodeposition-dependant of Iron Oxide Toward The Physicochemical Characteristics and Electrochemical Performance in Biorefractory Pollutant Degradation

Jurnal Riset Teknologi Pencegahan Pencemaran Industri, May 2023, Vol. 14, No. 1, p. 8-18, 7 ill, 0 tab, 41 ref

Electrodeposition of the iron oxide (Fe_xO_y) nanoparticles on the graphite felt was prepared from a mixture of iron (II) and iron (III) precursor solution with various pHs (2, 7, and 10) by applying a constant current (galvanostatic) of 0.1 A for 30 minutes. Each resulting sample was coded GF/Fe_xO_y -2, GF/Fe_xO_y -7, and GF/Fe_xO_y -10, respectively. Graphite felt without modification, Raw-GF, was used as control. The mass of iron oxide (Fe_xO_y) deposited ranged from 0.02 to 0.03 grams. The product characterisation using a Scanning

Electron Microscope (SEM) showed the distribution of 500 nm particles on the surface of the graphite felt for the GF/Fe_xO_y -2 sample. In comparison, the distribution of larger particles (1 – 2 µm) was observed in the samples of GF/Fe_xO_y -7 and GF/Fe_xO_y -10, respectively. Spectrum resulting from an X-ray Diffraction Spectroscopy (XRD) showed the formation of iron oxides (Fe_xO_y) such as magnetite (Fe_3O_4), haematite (Fe_2O_3), goethite (FeOOH), and lepidocrocite (FeO(OH)). Fourier Transform Infra-Red (FTIR) spectrum also confirmed the presence of Fe_2O_3 in the GF/Fe_xO_y -2 sample, Fe_3O_4 in the GF/Fe_xO_y -7 and GF/Fe_xO_y -10 samples, and FeOOH in all three samples. Applying the iron oxide modified graphite felt in the electro-Fenton approach process without aeration showed that it can degrade bio-refractory pollutants, such as methyl orange. The observed degradations of methyl orange were a decrease in the colour intensity up to 81.37% and a decrease in the COD up to 49.85%.

(Author)

Keywords: Biorefractory Pollutant, Electrochemical Degradation, Electrodeposition, Iron Oxide, Nanoparticles

---

Andrie Harmaji*[1], Alexander Syahlendra Haimir[2], Bambang Sunendar[3]

([1]Department of Metallurgical Engineering, Faculty of Engineering and Design, Institut Teknologi Sains Bandung, Cikarang 17530, Indonesia.
[2]Department of Materials Engineering, Faculty of Mechanical and Aerospace Engineering, Institut Teknologi Bandung, Bandung 40132, Indonesia.
[3]Department of Engineering Physics, Faculty of Industrial Technology, Institut Teknologi Bandung, Bandung 40132, Indonesia.)

Impact of Reduced Activator Concentration and Curing Method on Compressive Strength of Metakaolin/Fly Ash-based Geopolymer Mortar

Jurnal Riset Teknologi Pencegahan Pencemaran Industri, May 2023, Vol. 14, No. 1, p. 19-28, 12 ill, 5 tab, 21 ref

The demand for cement is increasing each year, but the manufacture of 1 tonne of cement produces an equal number of carbondioxide (CO_2) gas which is directly related to the increase in global warming. Therefore, we need a substitute material, namely geopolymer. This material has relatively superior properties compared to cement. However, one of the drawbacks of geopolymers is that the production costs are relatively more expensive compared to the manufacture of pre-cast cement because it requires chemical solutions such as sodium hydroxide (NaOH) and sodium silicate (Na_2SiO_3) to activate the precursor. This research was conducted to replace a specific ratio of alkali activator with water to reduce the use of alkaline hydroxide solutions and sodium silicate while reducing production costs.

The experiment was carried out by replacing the activator solution with water at a certain amount with a different curing method. Mechanical properties, X-Ray Diffraction (XRD), and Fourier Transform Infrared (FTIR) spectroscopy characterization were used to analyze the effect of additional water in geopolymer. The compressive test result shows that the maximum water content that can replace the activator solution is 20% by activator mass for fly ash-based geopolymers and 30% by activator mass for metakaolin-based geopolymers, with sealed and bare curing conditions before the compressive strength was decreased sharply. Substitution of 10% water in fly ash-based geopolymer increases the compressive strength to 17.20 MPa. Compressive test results and characterization showed that the optimal curing condition for fly ash-based geopolymer was sealed curing and bare curing for metakaolin-based geopolymer. The strength increase is due to O-C-O bonds representing sodium carbonate (Na_2CO_3), which affects the compressive strength of fly ash-based and metakaolin-based geopolymers.

(Author)

Keywords: Geopolymer, Fly Ash, Metakaolin, Alkali Activator, Sodium Carbonate

---

Suardi, Wira Setiawan, Andi Mursyd Nugraha, Alamsyah, Rodlian Jamal Ikhwani

([1]Shipping Engineering Study Program, Institut Teknologi Kalimantan, Balikpapan, Indonesia)

Evaluation of Diesel Engine Performance Using Biodiesel from Cooking Oil Waste (WCO)

Jurnal Riset Teknologi Pencegahan Pencemaran Industri, May 2023, Vol. 14, No. 1, p. 29-39, 8 ill, 6 tab, 22 ref

The increasing use of fossil fuels will cause the world's oil reserves to be depleted. In this case, it is necessary to increase the use of alternative renewable fuels, one of which is biodiesel waste cooking oil (WCO). The method used is an experimental test with a mixture of used cooking oil biodiesel and fuel. Before testing, the temperature of each fuel is increased to determine the effect of temperature on the density and viscosity values. The highest density value is found in B50 fuel at 26 °C, with a density of 0.854 gr/ml, while the lowest density is found in diesel fuel at 60 °C, with a density of 0.822 gr/ml. The highest viscosity value is found in B50 fuel at 26 °C and 60 °C, which is 3.26 cSt. After that, testing was carried out on a diesel engine, which produced the highest thermal efficiency value of 21.16% on B50 fuel with a temperature of 60 °C at 1000 rpm rotation and a load of 4000 watts. The lowest thermal efficiency of 6.43% was found in B50 fuel with a temperature of 26 °C at 800 rpm and a load of 1000 watts. The lowest consumption was found in B30 with a temperature of 60 °C at 1200 rpm, which was 420.78 gr/kWh. From the results of the tests that have been carried out, it can be concluded that the lower the density and viscosity of the fuel, the better the performance of the diesel engine on average. High temperatures effectively make the engine performance value better than normal temperatures (26 °C), and the performance of diesel engines is better with WCO fuel, especially in SFC.

(Author)

Keywords: Biodiesel, Diesel Engine, Engine Performance, Fuel Temperature, Waste Cooking Oil (WCO)

Haris Numan Aulia

([1]Polytechnic of Energy and Mineral (PEM) Akamigas, Cepu, Indonesia)

The Potency of Biodiesel Production from The Local Used Frying Oil Through The Electrocatalysis Method

Jurnal Riset Teknologi Pencegahan Pencemaran Industri, May 2023, Vol. 14, No. 1, p. 40-52, 13 ill, 6 tab, 29 ref

The objective of this study was to optimize the operating conditions for an electrocatalytic method of producing biodiesel from local used frying oil (UFO). The effects of electrical voltages (5-30 V), methanol-to-oil molar ratios (4:1-8:1), KOH catalyst concentrations (0.5-1.25% w/w), and electrolysis time (30-120 min) on biodiesel yield were investigated. The highest biodiesel yield of 95.3% was obtained at a voltage of 30 V, methanol-to-oil molar ratio of 6:1, catalyst concentration of 1% w/w, and electrolysis time of 120 min. A regression model was developed to predict the optimum operating conditions, resulting in a maximum biodiesel yield of 95.54%. The predicted optimum operating conditions were a voltage of 24.4 V, methanol-to-oil molar ratio of 5.8:1, catalyst concentration of 1% w/w, and electrolysis time of 120 min. The net profit of the biodiesel business using local UFO as a feedstock was estimated to be IDR 738,000 per month based on a simple economic calculation. These findings demonstrate the potential for using electrocatalytic methods to produce biodiesel from local UFO, and the economic feasibility of producing biodiesel in small-scale industries.

(Author)

Keywords: Biodiesel, Electrocatalyst, Methanol, Used Frying Oil, Yield

Vol. 14 No. 1 (2023) 1-7

Jurnal Riset
Teknologi Pencegahan Pencemaran Industri

Journal homepage : https://www.jrtppi.id

Kementerian
Perindustrian
REPUBLIK INDONESIA

A Low-Cost Instrument to Monitor Sulphur Dioxide Emissions Based on The DOAS Method

Nur Zen*[1,2], Haryono Setiyo Huboyo[1], Moch. Syarif Romadhon[3,4], Januar Arif Fatkhurrahman[2], Sidna Kosim Amrulah[2]

[1] Department of Environmental Engineering, Diponegoro University.
[2] Center for Standardization and Industrial Pollution Prevention Services.
[3] National Research and Innovation Agency.
[4] Atmospheric, Oceanic and Planetary Physics Department, University of Oxford.

ARTICLE INFO

Article history:
Received September 29, 2022
Received in revised form December 06, 2022
Accepted December 15, 2022
Available online May 02, 2023

Keywords :
DOAS
Emission
Sulphur Dioxide

ABSTRACT

Various techniques to measure SO_2 concentration based on Differential Optical Absorption Spectroscopy (DOAS) have been widely developed and applied for various measurements. However, most of the applications are still relatively expensive. Some efforts have been made to reduce the cost by using Ultraviolet Light Emitting Diodes (LEDs) as light sources, showing promising results. Further reductions can be possibly made by providing an alternative to replace high spectral resolution spectrometers widely used in DOAS applications since those spectrometers are commercially expensive. This paper studies the feasibility of a DOAS instrument using a low-cost spectrometer and UV-LEDs as light sources. The resolution of the spectrometer is 0.7 nm. With this resolution, it is expected that the instrument hardly captures narrow band structures of SO_2 optical absorption in the spectral range between 280 nm and 320 nm when measuring SO_2 gas concentration lower than the limits of SO_2 emissions regulated by the Indonesian government. To compensate for this drawback, narrow and broad bands of optical absorption structures are considered in the data analysis to achieve a detection limit far below the regulated limits. To capture the broadband structures, four UV-LEDs are used to cover spectral absorption from 250 nm to 320 nm. The instrument was calibrated using eight different standard concentrations of SO_2. The correlation between the readings and the standard concentrations is high, indicated by the Pearson correlation coefficient of 0.9999. It was also found that the lowest concentration the instrument can distinguish from blank samples or the Limit of Detection is 16 ppm. However, the instrument can precisely measure concentrations higher than or equal to 25 ppm with a standard deviation of less than 10% of the mean concentration measured from five measurements. This is far below the required legal limits, below 229 ppm. After the calibration, the DOAS instrument was used to measure SO_2 sampled from the emission of burning coals. To compare, a commercial SO_2 sensor was used to measure the same gas. The results indicate that the difference in the readings between the two instruments is around 6% of the concentration.

1. INTRODUCTION

One of the major pollutants in the atmosphere is Sulfur Dioxide (SO_2). The sources of atmospheric SO_2 can be anthropogenic and natural activities such as fuel combustion (Akimoto & Narita, 1994) and volcanic activities (Bani et al., 2022). In general, the formation of SO_2 in the combustion process follows the following reaction:

$$S_{(s)} + O_{2\,(g)} \rightarrow SO_{2\,(g)} \qquad (1)$$

---

*Correspondence author.
E-mail : nurzen.st@gmail.com (Nur Zen)

doi : https://10.21771/jrtppi.2023.v14.no.1.p1-7

Accreditation number : (Ristekdikti) 158/E/KPT/2021

Atmospheric SO_2 can have adverse effects on the environment and human health. For example, SO_2 can be oxidized to form sulfuric acid (Laaksonen et al., 2008) and sulfate aerosols that lead to environmental acidification (Rodhe, 1999). Meanwhile, exposure to high concentrations of SO_2 can cause irritation and malfunction of the human respiratory system (Kampa & Castanas, 2008). The presence of SO_2 in the atmosphere can cause acid rain with pH < 7 (Yunita & Kiswandono, 2017) because of the reaction below:

$$\tfrac{1}{2}O_{2\,(g)} + SO_{2\,(g)} + H_2O_{\,(l)} \rightarrow H_2SO_{4\,(g)} \qquad (2)$$

To tackle the negative impacts of atmospheric SO_2, some regulations were issued by the Indonesia Ministry of Environment. For example, legal limits for SO2 emitted from internal combustion engines were introduced in 2019 (MenLHK RI, 2019), and some of the limits are listed in Table 1. However, the measurement standard approved by the ministry is either not environmentally friendly since they produce chemical waste (Badan Standardisasi Nasional Indonesia, 2005, 2009) or expensive since they require periodic maintenance (EPA CTM-022, 1995). Furthermore, there is a need to measure SO_2 continuously at emission sources, as long-term measurements can provide a reliable assessment of the contribution of emission sources to the level of atmospheric SO_2 around the sources. None of the approved measurements are economically practical for continuous measurements. For example, based on USEPA CFR 40 part 75, continuous measurements can be done using chemical reagents such as sulphuric acid and hydrogen peroxide or an instrumental analyzer. The first method produces chemical wastes, and the second method is expensive since the corresponding instrument can cost between $20,000-$50,000 with periodic maintenance and calibration required.

An alternative to measure SO_2 is using Differential Optical Absorption Spectroscopy (DOAS). Using this method, gases can be continuously measured with minimal maintenance and no chemical waste produced. The method is based on the optical absorption structure of SO_2 with no direct interaction between the sample and light sensors (Stutz & Platt, 1996). DOAS method works in a wide range of wavelengths, from UV to visible (Fatkhurrahman et al., 2020). Furthermore, this technique does not require complex sample preparation and can use Light Emitting Diodes (LEDs) as light sources. These characteristics make DOAS suitable for a low-cost and environmentally friendly continuous measurement system.

Further cost reductions in a DOAS instrument can be made by providing an alternative to replace high spectral resolution spectrometers widely used in DOAS applications since those spectrometers are commercially expensive. For example, a spectrometer with 0.02 nm resolution can cost more than $30,000. This paper studies the feasibility of a compact DOAS instrument using a low-cost spectrometer designed to measure SO_2 from emission sources. The spectrometer used in the instrument has less than 2.0 nm of spectral resolution and costs around $3,000. With this resolution, the spectrometer is unlikely to measure SO_2 concentration far below the legal limits when it is used in a compact instrument with a short light path for light absorption. Therefore, the combination of the narrow and broadband structures of SO_2 absorption is used to determine SO_2 concentration to achieve a detection limit far below that regulated by the Indonesian government listed in Table 1.

Table 1. Limits of SO_2 in Inner Combustion Engine based on the Regulation of Indonesia Ministry of Environment Number 15 of 2019

Capacity	Fuel	Limits	
		mg/Nm^3	Ppm
< 3000 KW	Refined Fuel Oil	1800	687
	Diesel Oil	800	305
> 3000 KW	Refined Fuel Oil	1200	458
	Diesel Oil	600	229

2. METHODS

The central idea of the DOAS method is to retrieve gas concentration based on the spectral structure of optical absorption by the gas. The optical absorption, denoted as A, can be determined experimentally using two light intensities: those emitted by a light source, denoted as I_o (λ), and those absorbed by the gas, denoted as I(λ). The absorbance can be expressed mathematically as

$$A_{exp} = \ln[I(\lambda)] - \ln[I_o(\lambda)] \qquad (3)$$

where A_{exp} is experimentally determined absorbance. Optical absorption can be modelled as the absorption of light by gas. In a simple system where the length of optical absorption is relatively short, and there is only one gas that absorbs the light with no particles interfering with the absorption, then the absorption can be formulated as

$$A_{mod} = s\sigma(\lambda) + P(\lambda) \qquad (4)$$

where A_{mod} is modelled absorbance; $\sigma(\lambda)$ is the absorption cross-section of the gas (cm^2); $P(\lambda)$ is a linear function of λ representing interferences by other processes; s is a coefficient calculated by

$$s = nL \qquad (5)$$

where n is the density of gas molecules (particles/cm^3); L is the length of optical absorption (cm). The density can be derived from gas concentration as follow:

$$n = \frac{xN}{10^6} \qquad (6)$$

where x is the gas concentration (ppm); N is the density of air molecules (1/cm^3). In normal conditions, N is equal to 2.68×10^{19} particles/cm^3.

There are two components of $\sigma(\lambda)$: narrow and broad band cross-section denoted as $\sigma^n(\lambda)$ and $\sigma^b(\lambda)$, respectively. Mathematically, $\sigma(\lambda)$ can be expressed as

$$\sigma(\lambda) = \sigma^n(\lambda) + \sigma^b(\lambda) \qquad (7)$$

Most DOAS applications separate $\sigma^n(\lambda)$ from $\sigma^b(\lambda)$ as $\sigma^b(\lambda)$ is susceptible to interferences from light scattering due to air molecules and particles. In a condition where the scattering is minimized, such as in a relatively short light path, separation can be avoided. This condition is an advantage for an instrument using a low-resolution spectrometer, as the spectrometer is unlikely to resolve the structure of $\sigma^n(\lambda)$ when measuring optical absorption by low-concentration gas.

Three parameters are defined to characterize the performance of an instrument. The parameters are the Limit of Blank, Limit of Detection, and Limit of Quantification, denoted as LoB, LoD, and LoQ, respectively. The definition used in this study is as explained by Armbruster (Armbruster & Pry, 2008). The value of LoB and LoD can be determined as

$$LoB = \bar{c}_0 + 1.645\,\delta c_0 \qquad (8)$$

$$LoD = LoB + 1.645\,\delta c_{low} \qquad (9)$$

Where $\overline{c}_0$ is the mean of measured concentrations when the instrument measures blank samples; δc_0 and δc_{low} are the standard deviation of measured concentrations when the instrument measures blank samples and the lowest concentration distinguishable from blank samples, respectively. The value of LoQ can be defined as the lowest concentration the instrument can precisely measure. Two parameters can indicate the instrument's ability to precisely measure SO_2 of a particular concentration: the standard deviation of repetitive measurements and the Signal Noise Ratio (SNR) value. A minor standard deviation with Higher SNR can indicate the high ability of the instrument to precisely measure the concentration of interest. In the case of DOAS, the value of SNR can be calculated from the ratio between the sum of optical absorbance and the sum of residue signal. The residue signal is the difference between optical absorbance and A_{ext} and A_{mod}. There is no strict rule for the threshold of SNR. However, many consider the SNR of 1.0 is the threshold to indicate high-precision measurements.

3. INSTRUMENT DESIGN

The basic principle of the design is to measure $I_o(\lambda)$ and $I(\lambda)$ with minimum interference from other gases or particles. This requirement leads to a design with three major components: light sources, a cell, and a spectrometer. The design of the instrument is shown in Figure 1. As shown in the figure, SO_2 gas flows through the cell made of acrylic with a length of 30 cm. To capture $\sigma(\lambda)$ over a broad spectral range, four UV-LEDs with different spectral profiles are used to illuminate the gas. On the other side, a spectrometer is installed to measure transmitted light. The spectrometer used in the instrument is a CCS200 Spectrometer made by Thorlabs. The measurement range of the spectrometer is from 200 nm to 1000 nm with spectral accuracy lower than 2 nm. The spectrometer was calibrated using a mercury lamp, and it was concluded that its spectral accuracy is around 0.7 nm, evaluated at the spectral line of 365.0 nm. This spectral accuracy was used to convolve high-resolution SO_2 absorption cross-sections downloaded from the HITRAN database (Hermans, Vandaele, & Fally, 2009) ("HITRANonline - Absorption Cross Section Search," 2022). The high-resolution cross-section is shown as a blue line in Figure 2.a. The convolution was done for a range between 275 nm and 315 nm, and the results are shown as a red line in Figure 2.a. The UV-LED emission spectra were measured using the spectrometer, and the results are shown in Figure 2.b.

The depth of broad and narrow band structures is illustrated as dashed lines in Figure 2.a. As shown in the figure, the depth of the narrow structure significantly decreases when a low resolution of the spectrometer is used, while that of the broad structure only slightly changes. Therefore, the data analysis in this study uses both structures to ensure that the instrument has a significant sensitivity when measuring low concentrations of SO_2.

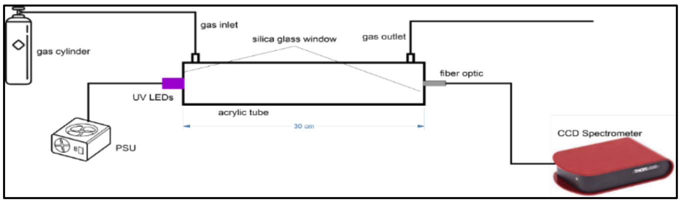

Figure 1. The DOAS instrument used in this study and its calibration setup.

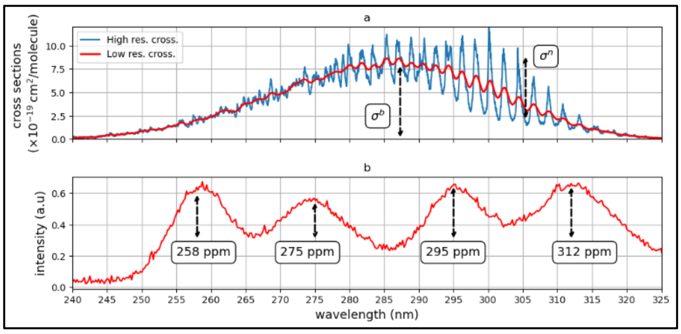

Figure 2. (a) The high and low resolution of SO_2 absorption cross-sections are shown as blue and red lines, respectively. As seen in the figure, there are broad and narrow band structures over a wide spectral range between 240 and 325 nm. One example of narrow band structures is indicated at absorption cross-sections around the wavelength of 305 nm. (b). The spectral intensity of the four UV-LEDs used in the DOAS instrument. It can be seen that the intensity covers the strong SO_2 spectral absorption between 250 nm and 320 nm.

4. CALIBRATION OF INSTRUMENT

The instrument was calibrated using eight different concentrations of SO_2. The concentrations are 0, 25, 50, 75, 100, 300, 500, and 1000 ppm. For each concentration, five measurements were performed. Based on the measurements, A_{exp} and A_{mod} were determined. To illustrate, some of the measurements are shown in Figure 3. The standard and measured SO_2 concentrations are indicated in the figure denoted as c_{std} and c_{mea}, respectively. As can be seen from the figure, $\sigma^b(\lambda)$ is predominant in the measurements of a concentration lower than 50 ppm. In the measurements of those higher than or equal to 75 ppm, both of $\sigma^b(\lambda)$ and $\sigma^n(\lambda)$ can be identified.

Based on the measurements, a calibration curve can be determined. The curve can be seen as a dashed blue line in Figure 4 with the corresponding scale on the left. In the figure, the mean and the standard deviations of the concentrations measured by the DOAS instrument are also indicated. As seen from the figure, the slope of the curve is nearly one, and the intercept is -6.4 ppm. The Pearson correlation coefficient between standard and measured concentrations is 0.93. Also, the ratio between the standard deviations and the mean of measured concentrations is lower than 2% of the mean concentration when the instrument measures concentrations higher than or equal to 300 ppm. For example, the standard deviation is 3 ppm when the instrument measured 300 ppm of SO2 five times with the mean of measured concentration 293 ppm. This higher precision when measuring high concentration can be due to the strong absorption structures for both broad and narrow absorption structures.

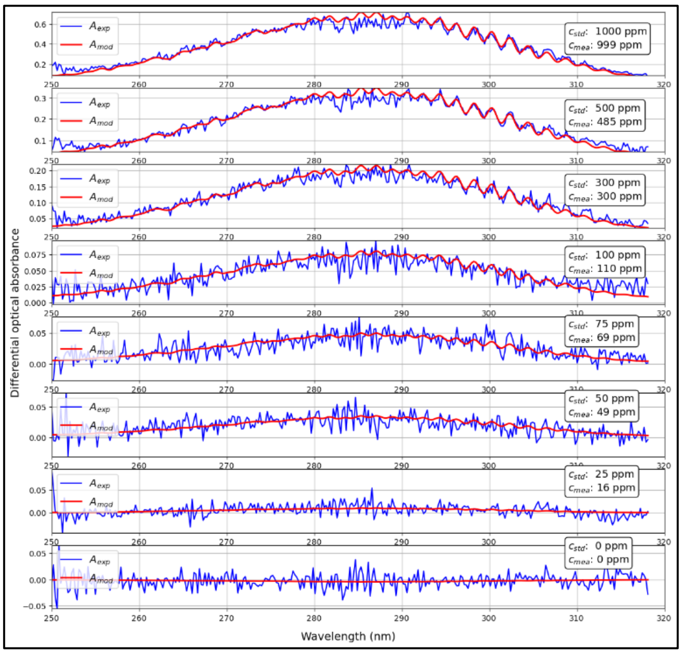

Figure 3. Some examples of optical absorption measurement for various SO_2 concentrations in the DOAS instrument calibration. The measured and modelled optical absorption are shown as blue and red lines, respectively. The concentrations were retrieved from the fitting between measured and modelled optical absorption. The results are indicated in the figure with c_{std} and c_{mea} denote the concentration of the gas standard and measured by the instrument, respectively.

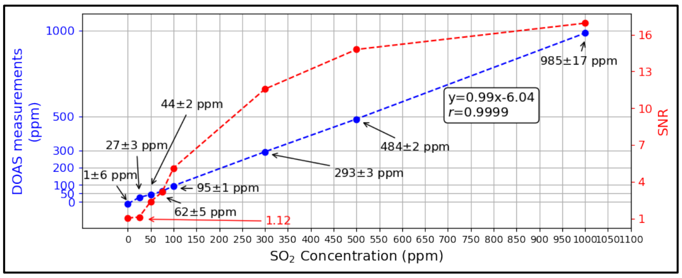

Figure 4. The calibration curve and the SNR of the measured optical depth.

Based on the calibration results, the value of the instrument's LoB, LoD, and LoQ can be determined. The mean concentration measured by the instrument was 1 ppm with a standard deviation of 6 ppm when the instrument measured blank samples. Using Eq. 8, the LoB of the instrument was calculated, and the result was around 11 ppm. The instrument also showed its ability to distinguish the concentration of 25 ppm from the blank, with a mean concentration of 27 ppm and a standard deviation of 3 ppm. So, LoD can be determined from the measurements of this concentration. Using Eq. 9, the value of LoD was calculated, and the result was around 16 ppm. The SNR of the measurements was calculated to analyze the LoQ of the instrument. The results are shown as a red line in Figure 4 with the corresponding scale on the right. Based on the figure, the SNR when the instrument measured a gas concentration of 25 ppm is slightly higher than 1. So, it can be safely assumed that the LoQ of the instrument is 25 ppm.

5. THE MEASUREMENTS OF SO_2 SAMPLED FROM INDUSTRY

The instrument was used to measure SO_2 gas sampled from coal-burning emissions. The gas was collected using a bag sampler. The measurements were done by transporting the gas into the cell of the DOAS instrument, and, as a comparison, a calibrated SO_2 commercial sensor was installed at the outlet of the instrument. To keep the air pressure inside the DOAS instrument at the ambient level, a T connector was installed at the outlet to split the flow into the commercial sensor and the ambient.

The commercial sensor used in this measurement was a PCA 3 Gas Analyzer made by Bacharach Inc. The gas analyzer has a measurement range of SO_2 between 0 ppm and 3000 ppm with a resolution of 1 ppm. It measures gas by drawing a small volume of the gas and passing it into an SO_2 sensor. The sensing mechanism of the sensor is based on an electrochemical reaction between SO_2 and SO_2-sensitive-material of the sensor generating electrical currents proportional to the concentration of SO_2.

The measurements can be divided into three stages. The first stage was the measurement of a blank sample. The blank sample was an ambient sample with a negligible concentration of SO_2. The second stage was the increasing concentration in the cell when the SO_2 sample started to flow into the cell. The third stage was the stable concentration when the SO_2 was well mixed inside the cell. The measurement results are shown in Figure 5. In the first stage, the reading of the DOAS instrument is around 25 ppm, indicated by a dashed line. This reading corresponds to the LoQ of the instrument. In the second stage, the reading of the DOAS instrument and the gas analyzer increased at a different rates. In the third stage, the reading of both instruments started to level off with a small amount of fluctuation. In the third stage, the average reading of the DOAS instrument and the gas analyzer were 211 ppm and 225 ppm, respectively. The difference is around 12 ppm or around 6% of the concentration.

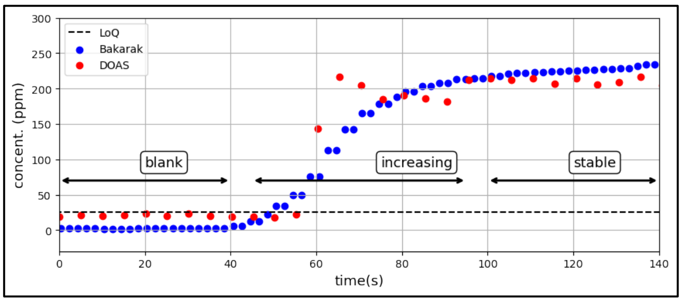

Figure 5. The measurement of SO2 sampled from the emission of coal burning.

6. CONCLUSION

The feasibility study of a low-cost instrument to measure SO_2 using a low-cost spectrometer and UV-LEDs as light sources were performed. The spectral range of the UV-LEDs is from 250 nm to 320 nm and can be used to measure a broad band structure of SO_2 absorption in this range. The low-cost spectrometer has a relatively low spectral resolution and is unlikely to resolve narrow band structures when measuring relatively low SO_2 concentration. Hence, in this study, broad band structures of SO_2 absorption were included in DOAS data analysis. The instrument's calibration shows the instrument's ability to measure concentrations higher than 25 ppm. Next, the instrument was used to measure SO_2 sampled from the emission of coal burning. As a comparison, a commercial SO_2 sensor was installed at the outlet of the DOAS instrument and measured the sampled gas when the gas left the cell. The results indicate that the DOAS instrument deviated from around 6% of that measured by the commercial sensor.

REFERENCE

Akimoto, H., & Narita, H. (1994). Distribution of SO_2, NOx and CO_2 emissions from fuel combustion and industrial activities in Asia with 1° × 1° resolution. Atmospheric Environment, 28(2), 213–225. https://doi.org/10.1016/1352-2310(94)90096-5

Armbruster, D. A., & Pry, T. (2008). Limit of blank, limit of detection and limit of quantitation. The Clinical Biochemist Reviews, 29 (Suppl 1), S49.

Badan Standardisasi Nasional Indonesia. (2005). Emisi Gas Buang – Sumber Tidak Bergerak – Bagian 3: Oksida-Oksida Sulfur (SOx) - Seksi 1 : Cara Uji Dengan Metoda Turbidimetri Menggunakan Spektofotometer.

Badan Standardisasi Nasional Indonesia. (2009). Emisi Gas Buang – Sumber Tidak Bergerak – Bagian 18 : Cara Uji Sulfur Dioksida (SO_2) Secara Turbidimetri Menggunakan Spektrofotometer.

Bani, P., Oppenheimer, C., Tsanev, V., Scaillet, B., Primulyana, S., Saing, U. B., Marlia, M. (2022). Modest volcanic SO_2 emissions from the Indonesian archipelago. Nature Communications 2022 13:1, 13(1), 1–15. https://doi.org/10.1038/s41467-022-31043-7

EPA CTM-022. (1995). EPA CTM-022.

Fatkhurrahman, J. A., Rasti, I., Sari, J., Andriani, Y., Romadhon, M. S., Zen, N., & Prasetio, A. (2020). Jurnal Riset Teknologi Pencegahan Pencemaran Industri DOAS Calibration Technique for SO_2 Emission Measurement Based on H_2SO_4 and Na_2SO_3 Reaction, 11(1), 36–45.

Hermans, C., Vandaele, A. C., & Fally, S. (2009). Fourier transform measurements of SO_2 absorption cross sections:: I. Temperature dependence in the 24 000–29 000 cm− 1 (345–420 nm) region. Journal of Quantitative Spectroscopy and Radiative Transfer, 110(9–10), 756–765.

HITRANonline - Absorption Cross Section Search. (2022).

Kampa, M., & Castanas, E. (2008). Human health effects of air pollution. Environmental Pollution, 151(2), 362–367.

Laaksonen, A., Kulmala, M., Berndt, T., Stratmann, F., Mikkonen, S., Ruuskanen, A., Viisanen, Y. (2008). Atmospheric Chemistry and Physics SO_2 oxidation products other than H_2SO_4 as a trigger of new particle formation. Part 2: Comparison of ambient and laboratory measurements, and atmospheric implications. Atmos. Chem. Phys, 8, 7255–7264.

MenLHK RI. (2019). Peraturan MenLHK RI No. 15 Tahun 2019 Tentang Baku Mutu Emisi Mesin Dengan Pembakaran Dalam.

Rodhe, H. (1999). Human impact on the atmospheric sulfur balance, 51–110. https://doi.org/10.3402/tellusa.v51i1.12309

Stutz, J., & Platt, U. (1996). Numerical analysis and estimation of the statistical error of differential optical absorption spectroscopy measurements with least-squares methods. Applied Optics, 35(30), 6041–6053.

Yunita, R. D., & Kiswandono, A. A. (2017). Kajian Indeks Standar Pencemar Udara (ISPU) Sulfur Dioksida (SO_2) Sebagai Polutan Udara Pada Tiga Lokasi Di Kota Bandar Lampung. Analit: Analytical and Environmental Chemistry, 2(1).

Vol. 14 No. 1 (2023) 8-18

Jurnal Riset
Teknologi Pencegahan Pencemaran Industri

Journal homepage : https://www.jrtppi.id

Kementerian
Perindustrian
REPUBLIK INDONESIA

The pH-electrodeposition-dependant of Iron Oxide Toward The Physicochemical Characteristics and Electrochemical Performance in Biorefractory Pollutant Degradation

Widya Ernayati Kosimaningrum*[1,2], Heri Heriyanto[1], Meri Yulvianti[1], Alia Badra Pitaloka[1,3], Muhammad Raja Najahtama[1], Muhammad Aditya Wibisana[1], Yulis Sutianingsih[4]

[1] Chemical Engineering Department, Faculty of Engineering, Universitas Sultan Ageng Tirtayasa, Cilegon 42435, Banten, Indonesia.

[2] Center for Local Food Innovation, PUI-PT, Universitas Sultan Ageng Tirtayasa, Serang, Banten, Indonesia.

[3] Biomass Valorization Laboratory, Center of Excellence, Faculty of Engineering, Universitas Sultan Ageng Tirtayasa, Cilegon 42435, Banten, Indonesia.

[4] Magister of Chemical Engineering Department, Faculty of Engineering, Universitas Sultan Ageng Tirtayasa, Cilegon 42435, Banten, Indonesia.

ARTICLE INFO

Article history:

Received August 19, 2022

Received in revised form November 11, 2022

Accepted November 17, 2022

Available online May 02, 2023

Keywords :

Biorefractory Pollutant

Electrochemical Degradation

Electrodeposition

Iron Oxide

Nanoparticles

ABSTRACT

Electrodeposition of the iron oxide (Fe_xO_y) nanoparticles on the graphite felt was prepared from a mixture of iron (II) and iron (III) precursor solution with various pHs (2, 7, and 10) by applying a constant current (galvanostatic) of 0.1 A for 30 minutes. Each resulting sample was coded GF/Fe_xO_y -2, GF/Fe_xO_y -7, and GF/Fe_xO_y -10, respectively. Graphite felt without modification, Raw-GF, was used as control. The mass of iron oxide (Fe_xO_y) deposited ranged from 0.02 to 0.03 grams. The product characterisation using a Scanning Electron Microscope (SEM) showed the distribution of 500 nm particles on the surface of the graphite felt for the GF/Fe_xO_y -2 sample. In comparison, the distribution of larger particles (1 – 2 μm) was observed in the samples of GF/Fe_xO_y -7 and GF/Fe_xO_y -10, respectively. Spectrum resulting from an X-ray Diffraction Spectroscopy (XRD) showed the formation of iron oxides (Fe_xO_y) such as magnetite (Fe_3O_4), haematite (Fe_2O_3), goethite (FeOOH), and lepidocrocite (FeO(OH)). Fourier Transform Infra-Red (FTIR) spectrum also confirmed the presence of Fe_2O_3 in the GF/Fe_xO_y -2 sample, Fe_3O_4 in the GF/Fe_xO_y -7 and GF/Fe_xO_y -10 samples, and FeOOH in all three samples. Applying the iron oxide modified graphite felt in the electro-Fenton approach process without aeration showed that it can degrade bio-refractory pollutants, such as methyl orange. The observed degradations of methyl orange were a decrease in the colour intensity up to 81.37% and a decrease in the COD up to 49.85%.

1. INTRODUCTION

Biorefractory pollutants contain recalcitrant organic compounds that cannot be decomposed through conventional biological processes (Barrera-Díaz, Linares-Hernández, Roa-Morales, Bilyeu, & Balderas-Hernández, 2009; Rajoriya, Carpenter, Saharan, & Pandit, 2016). These compounds contain azo bonds (-N=N-) (Guivarch, Trevin, Lahitte, & Oturan, 2003), which are difficult to digest by microorganisms. Biorefractory organic pollutants are also toxic and carcinogenic to macro- and micro-organisms (X. Yu, Zhou, Hu, Groenen Serrano, & Yu, 2014). Various industries such as textiles, dyes, pesticides, and pharmaceuticals continuously produce large amounts of organic pollutants (Rajoriya et al., 2016), which simultaneously trigger serious pollution problems in both

---

*Correspondence author.

E-mail : widya.ernayati@untirta.ac.id (Widya Ernayati Kosimaningrum)

doi : https://10.21771/jrtppi.2023.v14.no.1.p8-18

Accreditation number : (Ristekdikti) 158/E/KPT/2021

surface water and groundwater (X. Yu et al., 2014). Industrial wastes have passed through the treatment system, but the remnants of biorefractory compounds still potentially endanger the health of ecosystems, animals, and humans, even in tiny amounts (X. Yu et al., 2014). Therefore, the existence of a waste treatment system that effectively degrades biorefractory compounds needs to be developed.

Biorefractory organic waste treatment methods that have been developed include adsorption (Iwuozor, Ighalo, Emenike, Ogunfowora, & Igwegbe, 2021), ozonation (Baig & Liechti, 2001), membranes (W. Liu, Howell, Arnot, & Scott, 2001), electrochemical methods (Ganiyu et al., 2018), and advanced oxidation process (AOP) (Rajoriya et al., 2016). The electrochemical method with the AOP approach, the so-called electro-Fenton, is quite effective in degrading the biorefractory compounds of coloured azo compounds such as methyl orange, methyl red, and azo benzene (Guivarch et al., 2003). The electro-Fenton involves the reduction of oxygen at a cathode to generate hydrogen peroxide (HOOH), which can then be decomposed into hydroxide radicals (●OH) in the presence of a Fenton catalyst (Fe^{2+}) (Le et al., 2019). Hydroxide radicals are powerful oxidising agents for the AOP process, which can even degrade various and persistent organic compounds (Rajoriya et al., 2016).

The electro-Fenton process requires oxygen to generate H_2O_2, Fenton catalysts, and suitable electrodes that can facilitate the oxygen reduction reaction to H_2O_2. The oxygen in the water as dissolved oxygen is about 9 mg/L (Tai, Yang, Liu, & Li, 2012). The oxygen is usually supplied by purging oxygen gas or compressed atmospheric air to increase its saturation during the electro-Fenton process (Le et al., 2019). In a conventional electro-Fenton, a Fenton catalyst is added to the solution at a pH of 3 (Le et al., 2015). Carbon-based electrode materials are widely used as electrodes to generate H_2O_2, namely, graphite felt (Kosimaningrum et al., 2017; Miao, Zhu, Tang, Chen, & Wan, 2014), carbon felt (Huong Le, Bechelany, & Cretin, 2017), and activated carbon fibre (X. Yu et al., 2014). Various modifications of the carbon electrode were also carried out to improve its performance in the electro-Fenton process, one of which is by loading nanoparticles catalyst (Lian, Huang, Liang, Li, & Xi, 2019; K. Liu, Yu, Dong, Wu, & Hoffmann, 2018).

Iron oxide (Fe_xO_y) nanoparticles, such as haematite (Fe_2O_3) and magnetite (Fe_3O_4), are materials commonly applied to water and wastewater treatment (Petrov et al., 2020; Stoia, Păcurariu, Istratie, & Nižňanský, 2015). The iron oxide nanoparticles are potential catalysts in the electro-Fenton process (Ben Hafaiedh, Fourcade, Bellakhal, & Amrane, 2020). The iron oxide nanoparticles can be loaded onto carbon-based cathode materials through various processes such as chemical precipitation (Huiqun, Meifang, & Yaogang, 2006), adsorption (Gupta, Agarwal, & Saleh, 2011), encapsulation (Z. Wu, Li, Webley, & Zhao, 2012), and electrodeposition (M.-S. Wu, Ou, & Lin, 2010). In the electro-Fenton process, the iron oxide can be dissociated into Fe^{2+} and Fe^{3+} ions, which catalyse the breakdown of hydrogen peroxide to form hydroxide radicals in the solution (Ben Hafaiedh et al., 2020).

The electrodeposition method has successfully developed the preparation of iron oxide nanostructure, as reported elsewhere (Aghazadeh & Ganjali, 2018; Martinez et al., 2007; M.-S. Wu et al., 2010). This electrochemical method enables the regulation of the deposited nanomaterial by controlling the composition of precursor solution, pH, deposition mode, salt, and bath type. The electrodeposition method reveals a simple one-step process at room temperature, even without an additional capping agent to fabricate iron oxide nanoparticles. The conventional chemical method involves expensive materials, high temperatures, multi-step processes, and long-time synthesis. Thus, in general, electrochemical synthesis has been taken into account as a preferred method in the development of nanostructure materials due to its many advantages over the standard chemical method (Aghazadeh, 2019).

The advantages of the electrodeposition method are as follows; the mild operating conditions that can be carried out at room temperature and pressure, the use of fewer chemicals both in quantity and type, and fast reaction rates. Therefore, this study aimed to synthesise iron oxide, Fe_xO_y, which was carried out using a simple cathodic electrodeposition method on graphite felt carbon substrate in a mixture of iron(II) and iron(III) precursor solutions with various pHs. The electrodeposition product was then tested for its performance as a cathode in the electrochemical degradation of methyl orange through the electro-Fenton process. During the electro-Fenton process, neither oxygen gas nor compressed air was bubbled into the synthetic wastewater solution for aeration purposes. The novelty of this research was the study of the effect of precursor solution pH on the characteristics of the as-resulted iron oxide modified graphite felt and its performance in the electrochemical degradation of biorefractory compounds.

2. METHODS

2.1. Materials

The materials used in this study were commercial graphite felt technical grade, ethanol (96%) purchased from Bratachem, iron sulfate heptahydrate, $FeSO_4.7H_2O$ (99%), iron nitrate nonahydrate, $Fe(NO_3)_3.9H_2O$ (99%), methyl orange, sodium sulfate anhydrous, and sodium hydroxide were purchased from Merck.

2.2. Graphite felt sample preparation

Graphite felt was the basic carbon material to be modified in this study. The graphite felt was washed with 96% ethanol to remove the contaminants. The graphite felt was cut into pieces, 5 × 10 cm, soaked in 96% ethanol, and then ultrasonicated for 30 minutes. Next, the graphite felt was separated from the ethanol and washed with distilled water three times. The graphite felt was dried in an oven at 60°C for 24 hours. Furthermore, the cleaned and dried graphite felt was stored in a silica gel container.

2.3. Electrodeposition of iron oxide on graphite felt

Iron oxide was coated on graphite felt using the electrodeposition method developed by Aghazadeh & Ganjali (Aghazadeh & Ganjali, 2018) with several modifications. The electrodeposition was carried out in an electrochemical cell containing 125 mL of a 0.005 M precursor solution in the form of a mixture of Fe (II), from $FeSO_4.7H_2O$, and Fe (III), from $Fe(NO_3)_3.9H_2O$ with pH variations of 2, 7, and 10, respectively. The graphite felt as a cathode, and the titanium mesh coated with platinum as an anode were set in the cell at a fixed distance of 3 cm. The electrodeposition was carried out, without stirring, by flowing a constant current of 0.1 A (2.4 mA/cm^2) for 30 minutes at room temperature and pressure. The resulting modified graphite felt was dried in a vacuum oven at 60°C for 24 hours. The mass of graphite felt before and after electrodeposition was weighed to determine the mass of iron oxide deposited on the graphite felt. The iron oxide modified graphite felts, Fe_xO_y, produced from the precursor solution with variations in pH of 2, 7, and 10, were coded as GF/ Fe_xO_y -2, GF/ Fe_xO_y -7, and GF/ Fe_xO_y -10, respectively. Meanwhile, Raw-GF, graphite felt without modification, was used as the experimental control.

2.4. Physicochemical Analysis

The morphology of the electrosynthesis product samples was scanned with a Jeol JSM-6510 scanning electron microscope (SEM). At the same time, the material structure was analysed using an X-Ray Diffraction Spectrophotometer, XRD, Shimadzu XRD-7000, and a Fourier-Transform Infra-Red, FTIR, Perkin Elmer.

2.5. The electrochemical degradation process of synthetic waste

The resulting iron oxide coated graphite felt sample was used as an electrode in the degradation process of synthetic waste. Each sample was cut to a 0.5 × 1 10 cm size with an iron oxide coated area of about 0.5 × 1 × 3.5 cm. This iron oxide modified graphite felt was used as a cathode, and the platinum-coated titanium was used as an anode in the electro-Fenton process. The electro-Fenton was carried out on 125 mL of 0.1 mM methyl orange synthetic waste in 0.05 M sodium sulfate solution for 1 hour with a constant current of 0.2 A and continuous stirring. Before and after the electro-Fenton process, the synthetic waste's colour and Chemical Oxygen Demand (COD) were analysed. The colour of the synthetic waste was determined based on the absorbance value of the methyl orange solution measured using a UV-Visible spectrophotometer at a wavelength of 470 nm. Furthermore, the COD of the synthetic waste was measured using the Standard Method 5220D. The colour and COD removal efficiencies were calculated using equations 1 (Parshetti, Telke, Kalyani, & Govindwar, 2010) and 2 (Yang, Liang, Zhang, & Liang, 2016), respectively.

$$\%\ \textit{colour removal} = \frac{\textit{(Initial absorbance-Final absorbance)}}{\textit{Initial absorbance}} \times 100\% \quad (1)$$

$$\%\ \textit{COD removal} = \frac{Initial\ COD - final\ COD}{Initial\ COD} \times 100\ \% \quad (2)$$

3. RESULT AND DISCUSSION

Figure 1 shows a mixed solution of iron(II) and iron(III), as referred to by Aghazadeh et al. (Aghazadeh &

Ganjali, 2018) at pH of 2, 7, and 10 as a representation of acidic, neutral, and basic conditions. A mixed solution of iron (II) and iron (III) had a pH of 2.36. The solution pH was adjusted to 7 and 10 by adding 5 M NaOH solution dropwise. An increase in pH caused a change in the colour of the solution to dark brown. The solution was brown at a pH of 7 and black at a pH of 10. This indicated that iron(II) and iron(III) ions reacted with hydroxide ions, as stated by Koo et al. in equation 3 (Koo, Ismail, Othman, Rahman, & Sheng, 2019).

$Fe^{2+} + Fe^{3+} + 8OH^- \rightarrow Fe(OH)_2 + 2Fe(OH)_3 \rightarrow Fe_3O_4 + 4H_2O$ (3)

The observed colour of the pH-7 solution was brown, resulting from the mixture of the $Fe(OH)_2$ solution (green) and the $Fe(OH)_3$ solution (brick red) (Ghernaout et al., 2009). While the colour observed in the pH-10 solution, black, indicated the formation of iron oxide magnetite, Fe_3O_4 (Koo et al., 2019).

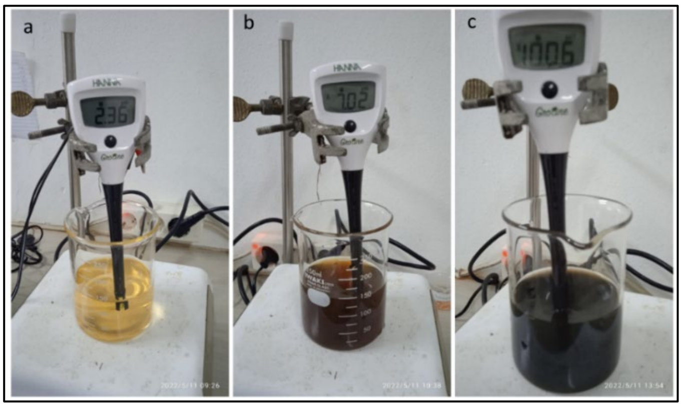

Figure 1. Profile of the mixture of iron (II) and iron (III) precursor solutions at (a) acidic, (b) neutral, and (c) basic pH

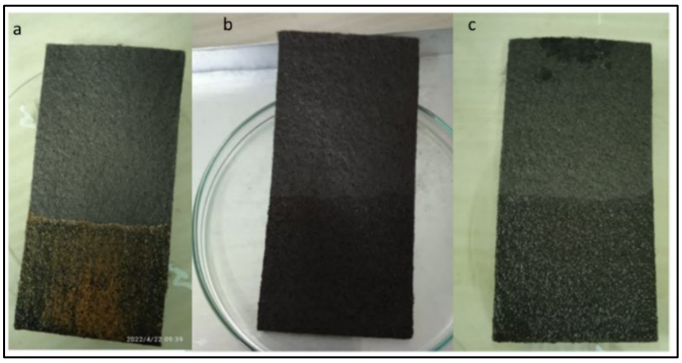

Figure 2. The resulting iron oxide modified graphite felt from the precursor solution at various pH; a. GF/Fe_xO_y -2, b. GF/Fe_xO_y -7, dan c. GF/Fe_xO_y -10

The electrodeposition in each precursor solution was carried out using the galvanostatic method at 2.4 mA/cm^2 for 30 minutes. Applying the current can cause the oxidation of ferrous ions to ferric oxide. The reaction at the graphite felt cathode was the reduction of water to hydroxide ions and hydrogen gas (equation 4) and the reduction of Fe^{3+} ions to Fe^{2+} ions (equation 5) (Aghazadeh & Ganjali, 2018).

$H_2O + 2e^- \rightarrow 2OH^- + H_2$ (4)

$Fe^{3+} + e^- \rightarrow Fe^{2+}$ (5)

The presence of OH^- ions and Fe^{2+} and Fe^{3+} ions can stimulate the formation of iron oxide magnetite (Fe_3O_4) deposits based on equation 6 on the cathode surface (Aghazadeh & Ganjali, 2018).

$Fe^{3+} + Fe^{2+} + OH^- \rightarrow Fe_3O_4$ (6)

Figure 2 shows the electrodeposition of graphite felt in a solution of iron ion precursors under acidic, neutral, and basic conditions, respectively. On each surface of the graphite felt, the presence of a coating, which was a deposit of iron oxide (Fe_xO_y), can be observed. The deposits formed in the GF/Fe_xO_y -2 sample (Figure 2a) were brown with a mass of 0.02 grams. The brownish iron oxide indicated the iron oxide hematite, Fe_2O_3. The black deposits in the samples of GF/Fe_xO_y -7 (Figure 2b) and GF/Fe_xO_y-10 (Figure 2c) that weighed 0.03 and 0.02 grams, respectively, indicated the formation of iron oxide magnetite, Fe_3O_4. Based on the XRD and FTIR spectrum (Fig. 5a and 5b), the GF/Fe_xO_y -7 contains a mixture of haematite and magnetite, which may cause a slightly higher mass than the two other products.

Figure 3 shows the morphology of clean graphite felt (Raw-GF) and the three samples of electrodeposition products, namely GF/Fe_xO_y-2, GF/Fe_xO_y-7, and GF/Fe_xO_y-10 at 1000× magnification. Graphite felt as a support material was composed of carbon fibres with a diameter of about 20 μm. The Raw-GF sample (Figure 3a), which was a sample without modification, showed clean carbon fibres. The GF/Fe_xO_y -2 sample (Figure 3b) showed the distribution of white dots deposited around the carbon fibres. In contrast, the GF/Fe_xO_y -7 (Figure 3c) and GF/Fe_xO_y -10 samples (Figure 3d) showed the presence of deposits on the surface of the carbon fibres in the form of larger particles or lumps.

Figure 4 shows the SEM result of each modified FexOy electrode with a magnification of 5000× – 10000×. According to Buzea et al., nanoparticles have a size below 1 μm (<1000 nm), while microparticles have a size above 1 μm

(>1000 nm) (Buzea, Pacheco, & Robbie, 2007). Nanoparticle-sized deposits (<500 nm) tended to form in the GF/Fe_xO_y -2 sample (Figures 4a,b), which was produced by electrodeposition in the precursor solution at a pH of 2. Electrodeposition in the precursor solution with pH of 7 produced the deposit of particles, with an approximate size of 500 – 1000 nm (Figures 4c,d), and electrodeposition at pH 10 resulted in the deposit of larger particles size (Figures 4e,f). In an acidic environment, the ions were more dissociated so that the iron ions could quickly spread throughout the surface of the graphite felt. Once the iron ions arrive on the graphite surface, they can react with hydroxide ions as-resulted of water reduction (Aghazadeh & Ganjali, 2018) to form small particles ($\leqslant$ 500 nm), then were deposited on the surface of the graphite felt. The external addition of hydroxide ions to the solution caused an uncontrolled reaction with iron(II) and iron(III) in the precursor solution. It allowed the formation of larger particles (> 500 nm) which can be deposited as lumps on the graphite felt surface.

Figure 5a shows the spectrum of XRD measurement results. The increase in the pH of the electrodeposition precursor solution increased the intensity in the theta area of 20-30°. Based on the Reference Database Library, the peak at the mentioned area was FeOOH, interpreted as goethite and lepidocrocite, as can be observed in equation 7 (Martinez et al., 2007).

$$Fe^{2+} + 2H_2O \rightarrow Fe\text{-}OOH + e + 3H^+ \qquad (7)$$

The peak observed in the area between 40 – 50° indicated the existence of iron oxide magnetite, Fe_3O_4. This peak was visible in the electrodeposition sample at a pH of 10. The formation of Fe_3O_4, black deposits on the surface of graphite felt, was effective at a pH above 8. At pH of 7 and 2, magnetite peaks did not appear clearly. Meanwhile, at pH 7 and 2, the 37° area peak was interpreted as forming Fe_2O_3. Furthermore, at a pH of 2, the reddish-brown layer formed was characterised as haematite. The FTIR spectrum of the GF/Fe_xO_y -2 sample (Figure 5b) showed a sharp stretching peak of Fe-O at wave number 594 cm^{-1} (Fard, Mirjalili, & Najafi, 2018) and 450 cm^{-1} (Sobhanardakani, Jafari, Zandipak, & Meidanchi, 2018) which were typical for Fe_2O_3. The spectra of GF/Fe_xO_y -7 and GF/Fe_xO_y -10 (Figure 5b) were quite similar to each other, which shows the broad weak peak in the area between 500 cm^{-1} and 700 cm^{-1} as the Fe-O stretching peak of Fe_3O_4(Raghu et al., 2017).

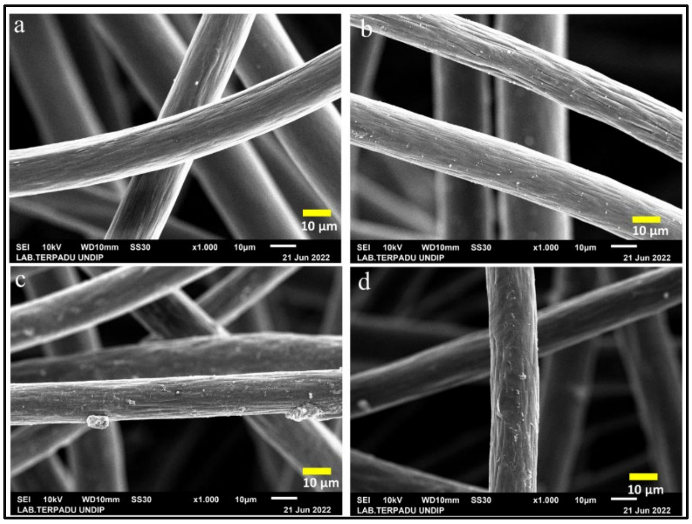

Figure 3. Morphological profile of the sample based on SEM measurements at 1000× magnification for the samples; a) control sample, coded Raw-GF or graphite felt without modification, b. sample GF/Fe_xO_y -2, c. sample GF/Fe_xO_y -7, and d. GF/Fe_xO_y -10.

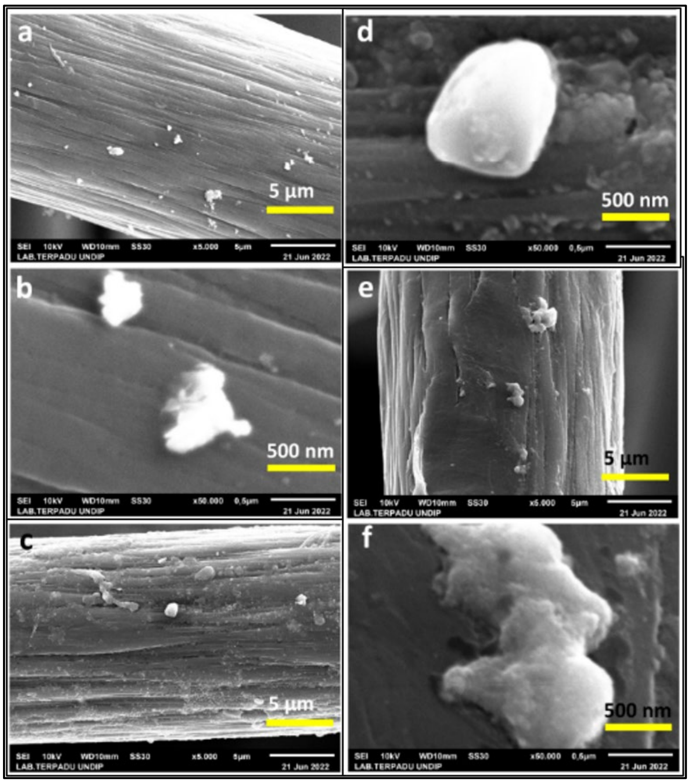

Figure 4 Morphological profile of the samples based on SEM measurements at a magnification of 5000× and 10,000× for the samples; a, b. sample GF/Fe_xO_y -2, c, d. sample GF/ Fe_xO_y -7, and e,f. GF/Fe_xO_y -10.

Methyl orange is an organic compound with an azo bond (-N=N-) in its structure, so it is hardly degraded through the conventional microbial degradation method (Han et al., 2015). Furthermore, the ionic sulphonate group makes it very soluble in water (Han et al., 2015), which can quickly spread in aquifers, making it difficult to remove. Therefore, methyl orange can be classified as a biorefractory organic waste that can increase water's chemical oxygen demand (COD) (Guivarch et al., 2003).

In this study, methyl orange was electrochemically degraded using the GF/Fe_xO_y -2, GF/Fe_xO_y -7, and GF/Fe_xO_y -10 samples. Figure 6a shows the methyl orange synthesis waste solution before and after electrochemical treatment. Samples of Raw-GF, GF/Fe_xO_y -2, GF/Fe_xO_y -7, and GF/Fe_xO_y -10 were used as the cathode, and platinum-coated titanium was used as the anode, respectively. Visually, the processed solution showed a significant decrease in colour intensity. Measurements with a UV-Vis spectrophotometer at a wavelength of 470 nm also showed a sharp decrease in absorbance in the post-treatment solution. The average colour loss based on the absorbance measurement results was between 77.69 – 81.43 % for the three modified and the control electrodes (Figure 6b).

The GF/Fe_xO_y -7 resulted in a higher colour removal efficiency than the GF/Fe_xO_y -2. The formerly contained magnetite (Fe_3O_4), and the latter contained haematite (Fe_2O_3). It showed that Fe_3O_4 had a higher catalytic activity than Fe_2O_3. This result was in line with the study of Prasetyo et al. reporting that Fe_3O_4 was more effective than Fe_2O_3 in the Fenton reaction (Prasetyo, Akbar, Prabandari, & Ariyanto, 2019). However, the GF/Fe_xO_y -10 resulted in a lower colour removal efficiency than the GF/Fe_xO_y -2, although the former dominantly contained Fe_3O_4 and the latter dominantly contained Fe_2O_3. The particle size of the materials caused this. The GF/Fe_xO_y -10 and GF/Fe_xO_y -2 had microparticle and nanoparticle sizes, respectively. The GF/Fe_xO_y -2 was more effective than the GF/Fe_xO_y -10 because the former had a smaller particle size, namely nanoparticle. Graphite felt, a material composed of carbon fibers, can adsorb methyl orange compound in the solution, so the colour of the solution fades. The presence of iron oxide can aid in colour removal by catalysing the breakdown of azo bonds in methyl orange compounds (Han et al., 2015).

In this study, iron oxide's role was insignificant compared to raw graphite felt (Figure 6b). So, in this case, the colour removal can be inferred to be dominated by the adsorption process. Figure 6b also shows that colour removal was not in line with the COD removal. Concentration, color removal, and COD removal should be in harmony in the case of dilution but not in the case of oxidation. In this research, methyl orange experienced oxidative degradation through a series of breakdowns to form small organic fragments as intermediates and CO_2 and H_2O as the expected final product.

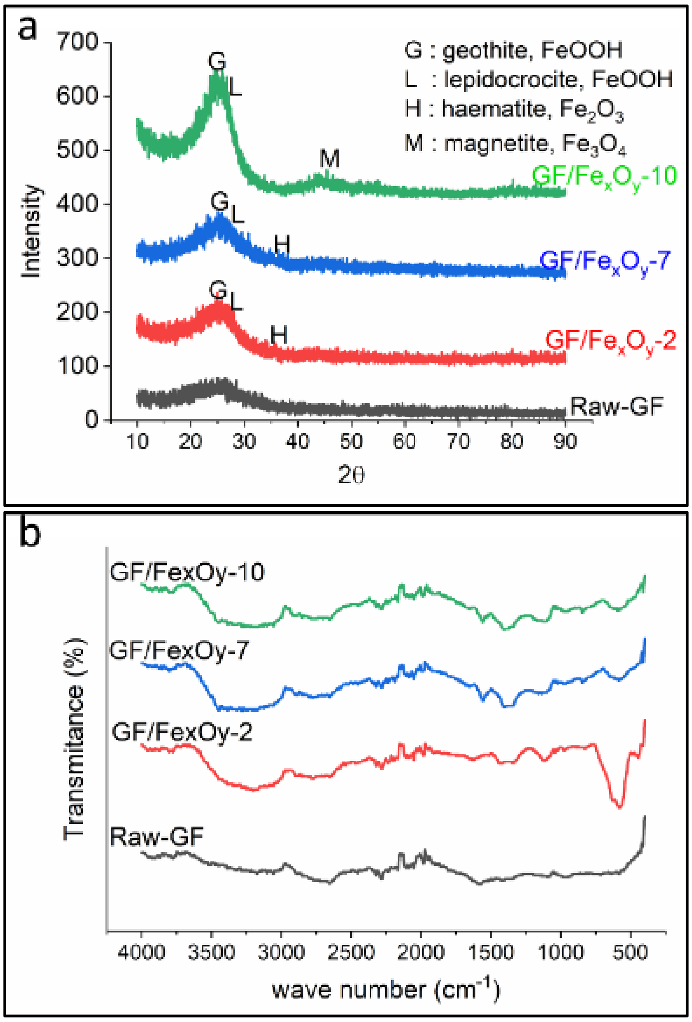

Figure 5. The spectrum of the control and the FexOy modified graphite felt samples; a. XRD dan b. FTIR

The detailed mechanism of methyl orange degradation has been proposed by Kgatle et al., as shown in Figure 7. Hydroxyl radical attacks the azo bond of the methyl orange, which splits methyl orange into N-N dimethyl-p-phenyl diamine and sulphanilic acid. The radical attacks continue the breakdown of these intermediate compounds into many smaller and aliphatic organic fragments. The hydroxyl radicals are expected to oxidize all organic fragments to carbon dioxide completely and water(Kgatle, Sikhwivhilu, Ndlovu, & Moloto, 2021) hence eliminating COD. However, incomplete oxidation can occur, which leaves a high content of small organic fragments and make the COD remain high or increase. In this case, decolourisation can be occurred due to the change of organic compound composition instead of dilution. Initially, methyl orange contains a chromophore group in its structure which is responsible for its colour that absorbs visible light. After the breakdown, the small organic fragments may not contain the chromophore group anymore, and thus, the colour disappears. Herein, the resulting fade colour of the post-oxidation solution may not mean a low COD or organic compound concentration.

The effect of iron oxide was seen in the COD measurement results correlated with the content of organic compounds in the solution (Guivarch et al., 2003). The decrease in COD indicated the presence of mineralization/oxidative degradation of methyl orange with hydroxyl radicals to the inorganic residue, as briefly shown in equation 8. The expected end products are only carbon dioxide and water. However, some other side products, such as SO2 or acid, considered pollutant compounds, can be emerged. Therefore, other treatments should be conducted before effluent discharge to avoid environmental hazards.

$$2C_{14}H_{14}N_3SO_3Na + 82OH\cdot \rightarrow 28CO_2 + 14H_2O + 3N_2 + 2SO_2 + 82H^+ \quad (8)$$

The Raw-GF sample was only able to reduce COD by 20.11 % (Figure 6b), which conforms with the work by Yu et al. (F. Yu, Zhou, & Yu, 2015). The COD removal capability of Raw-GF is predicted due to its adsorptive process. Although Raw-GF also produces hydrogen peroxide (Zhou, Zhou, Hu, Bi, & Serrano, 2014), the formation of hydroxyl radicals for mineralisation is unfeasible due to the lack of a catalyst. In this research, the addition of iron oxide to graphite felt has affected the methyl orange degradation performance. Iron oxides catalyze the Fenton reaction, which is the breakdown of H_2O_2 to hydroxyl radical and performs oxidative degradation. Herein, The GF/Fe_xO_y -2 sample gave the best COD reduction up to 49.84 %. This result is slightly higher than Santana et al. work which utilized Fe_2O_3/MCM for methyl orange degradation that reached 45 % of COD removal (Sidney Santana, Freire Bonfim, da Cruz, da Silva Batista, & Fabiano, 2021).

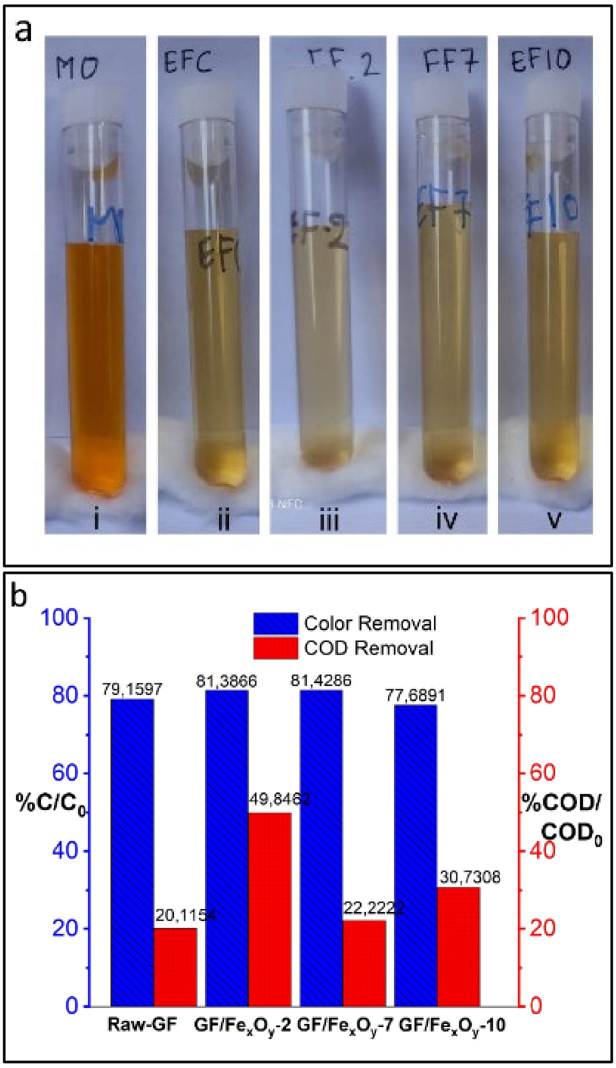

Figure 6. Performance of the iron oxide (Fe_xO_y) modified graphite felt samples upon electrochemical degradation of methyl orange waste; a. the colour of the waste before (i) and after the process (ii – v), b. the colour and COD removal efficiencies

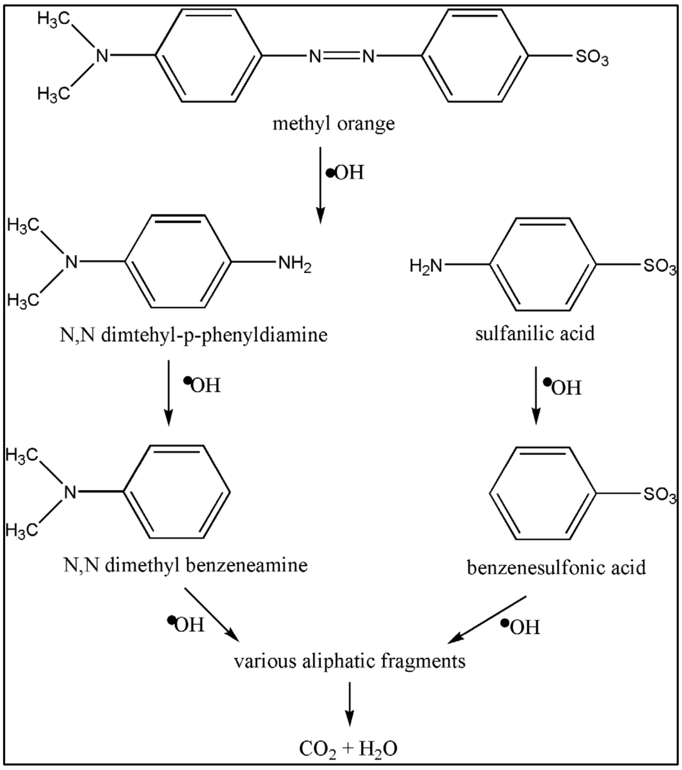

Figure 7 The proposed oxidative methyl orange degradation (Kgatle et al., 2021)

The nanoparticle size of the iron oxide formed on the graphite felt contributes to a better effectivity of the catalyst in the hydroxyl radical generation to conduct mineralisation. The GF/Fe_xO_y -10 sample reduced COD by 30.73%, close to the Jiang et al. work result that used Fe_3O_4 catalyst in methyl orange degradation and reached 32 % of total organic carbon removal(Jiang, Sun, Feng, & Wang, 2016). The GF/Fe_xO_y -10 was indicated to contain iron oxide as magnetite, Fe_3O_4, which has been reported as an effective catalyst in the Fenton reaction (Prasetyo et al., 2019). However, the GF/Fe_xO_y -7 shows only 22.22 % of COD removal. According to its physicochemical characterization, GF/Fe_xO_y -7 contains a mixture of Fe_2O_3 and Fe_3O_4, each having different catalytic properties. The combination of Fe_2O_3 and Fe_3O_4 is predicted to lead to an adverse reaction and incomplete oxidation, leaving abundant small organic fragments and increasing the COD in the post-treatment solution. Thus, the effectiveness of iron oxide on the degradation of methyl orange waste depends on the particle size, the kind, and the composition controlled by the pH (Aghazadeh, 2019) during synthesis.

4. CONCLUSION

The pH of the precursor solution affected the characteristics of the iron oxide (Fe_xO_y) deposited on the graphite felt. In an acid solution (pH of 2), the iron oxide formed indicated the dominant type of FeOOH (goethite and lepidocrocite) and Fe_2O_3 (haematite) as 500 nm. The synthesized iron oxide in neutral (pH of 7) and basic (pH of 10) solutions also indicated the type of FeOOH (goethite and lepidocrocite) and Fe_3O_4 (magnetite) with a particle size of more than 500 nm. The colour removal performances of Raw-GF, GF/Fe_xO_y -2, GF/Fe_xO_y -7, and GF/Fe_xO_y -10 were 79.16 %, 81.39 %, 81.43 %, and 77.69 %, respectively. The GF/Fe_xO_y -2 sample gave a dominant COD reduction of up to 49.84 %, while the GF/Fe_xO_y -7 and the GF/Fe_xO_y -10 sample reduced COD by 22.22 % and 30.73%, respectively. The non-modified graphite felt, Raw-GF, the sample was only able to reduce COD by 20.11 %.

ACKNOWLEDGEMENT

We want to thank the University of Sultan Ageng Tirtayasa, Banten- Indonesia, for the research funding through the 2022 Intermediate Lecturer Research project (PDM 2022).

REFERENCE

Aghazadeh, M. (2019). Electrochemical Synthesis of Dextran-and Polyethyleneimine-Coated Superparamagnetic Iron Oxide Nanoparticles and Investigation of their Physico-chemical Characters. ANALYTICAL & BIOANALYTICAL ELECTROCHEMISTRY, 11(3), 362–372.

Aghazadeh, M., & Ganjali, M. R. (2018). Samarium-doped Fe_3O_4 nanoparticles with improved magnetic and supercapacitive performance: a novel preparation strategy and characterization. Journal of Materials Science, 53(1), 295–308. https://doi.org/10.1007/s10853-017-1514-7

Baig, S., & Liechti, P. A. (2001). Ozone treatment for biorefractory COD removal. Water Science and Technology, 43(2), 197–204. https://doi.org/10.2166/wst.2001.0090

Barrera-Díaz, C., Linares-Hernández, I., Roa-Morales, G., Bilyeu, B., & Balderas-Hernández, P. (2009). Removal of Biorefractory Compounds in Industrial Wastewater by Chemical and Electrochemical Pretreatments. Industrial & Engineering Chemistry Research, 48(3), 1253–1258. https://doi.org/10.1021/ie800560n

Ben Hafaiedh, N., Fourcade, F., Bellakhal, N., & Amrane, A. (2020). Iron oxide nanoparticles as heterogeneous electro-Fenton catalysts for the removal of AR18 azo dye. Environmental Technology, 41(16), 2146–2153. https://doi.org/10.1080/09593330.2018.1557258

Buzea, C., Pacheco, I. I., & Robbie, K. (2007). Nanomaterials and nanoparticles: Sources and toxicity. Biointerphases, 2(4), MR17–MR71. https://doi.org/10.1116/1.2815690

Fard, G. C., Mirjalili, M., & Najafi, F. (2018). Preparation of nano-cellulose/A-Fe_2O_3 hybrid nanofiber for the cationic dyes removal: Optimization characterization, kinetic, isotherm and error analysis. Bulgarian Chemical Communications, 50(August), 251–261.

Ganiyu, S. O., Huong Le, T. X., Bechelany, M., Oturan, N., Papirio, S., Esposito, G., … Oturan, M. A. (2018). Electrochemical mineralization of sulfamethoxazole over wide pH range using FeIIFeIII LDH modified carbon felt cathode: Degradation pathway, toxicity and reusability of the modified cathode. Chemical Engineering Journal, 350, 844–855. https://doi.org/https://doi.org/10.1016/j.cej.2018.04.141

Ghernaout, D., Ghernaout, B., Boucherit, A., Naceur, M. W., Khelifa, A., & Kellil, A. (2009). Study on mechanism of electrocoagulation with iron electrodes in idealised conditions and electrocoagulation of humic acids solution in batch using aluminium electrodes. Desalination and Water Treatment, 8(1–3), 91–99. https://doi.org/10.5004/dwt.2009.668

Guivarch, E., Trevin, S., Lahitte, C., & Oturan, M. A. (2003). Degradation of azo dyes in water by Electro-Fenton process. Environmental Chemistry Letters, 1(1), 38–44. https://doi.org/10.1007/s10311-002-0017-0

Gupta, V. K., Agarwal, S., & Saleh, T. A. (2011). Chromium removal by combining the magnetic properties of iron oxide with adsorption properties of carbon nanotubes. Water Research, 45(6), 2207–2212. https://doi.org/https://doi.org/10.1016/j.watres.2011.01.012

Han, L., Xue, S., Zhao, S., Yan, J., Qian, L., & Chen, M. (2015). Biochar supported nanoscale iron particles for the efficient removal of methyl orange dye in aqueous solutions. PLoS ONE, 10(7). https://doi.org/10.1371/journal.pone.0132067

Huiqun, C., Meifang, Z., & Yaogang, L. (2006). Decoration of carbon nanotubes with iron oxide. Journal of Solid State Chemistry, 179(4), 1208–1213. https://doi.org/https://doi.org/10.1016/j.jssc.2005.12.040

Huong Le, T. X., Bechelany, M., & Cretin, M. (2017). Carbon felt based-electrodes for energy and environmental applications: A review. Carbon, 122, 564–591. https://doi.org/https://doi.org/10.1016/j.carbon.2017.06.078

Iwuozor, K. O., Ighalo, J. O., Emenike, E. C., Ogunfowora, L. A., & Igwegbe, C. A. (2021). Adsorption of methyl orange: A review on adsorbent performance. Current Research in Green and Sustainable Chemistry, 4, 100179. https://doi.org/https://doi.org/10.1016/j.crgsc.2021.100179

Jiang, H., Sun, Y., Feng, J., & Wang, J. (2016). Heterogeneous electro-Fenton oxidation of azo dye methyl orange catalyzed by magnetic Fe3O4 nanoparticles. Water Science and Technology, 74(5), 1116–1126. https://doi.org/10.2166/wst.2016.300

Kgatle, M., Sikhwivhilu, K., Ndlovu, G., & Moloto, N. (2021). Degradation Kinetics of Methyl Orange Dye in Water Using. Catalysts, 11, 428.

Koo, K. N., Ismail, A. F., Othman, M. H. D., Rahman, M. A., & Sheng, T. Z. (2019). Preparation and characterization of superparamagnetic magnetite (Fe3O4) nanoparticles: A short review. Malaysian Journal of Fundamental and Applied Sciences, 15(1), 23–31.

Kosimaningrum, W. E., Le, T. X. H., Holade, Y., Bechelany, M., Tingry, S., Buchari, B., … Cretin, M. (2017).

Surfactant- and Binder-Free Hierarchical Platinum Nanoarrays Directly Grown onto a Carbon Felt Electrode for Efficient Electrocatalysis. ACS Applied Materials & Interfaces, 9(27), 22476–22489. https://doi.org/10.1021/acsami.7b04651

Le, T. X. H., Bechelany, M., Lacour, S., Oturan, N., Oturan, M. A., & Cretin, M. (2015). High removal efficiency of dye pollutants by electron-Fenton process using a graphene based cathode. Carbon, 94, 1003–1011. https://doi.org/10.1016/j.carbon.2015.07.086

Le, T. X. H., Cowan, M. G., Drobek, M., Bechelany, M., Julbe, A., & Cretin, M. (2019). Fe-nanoporous carbon derived from MIL-53(Fe): A heterogeneous catalyst for mineralization of organic pollutants. Nanomaterials, 9(4), 1–11. https://doi.org/10.3390/nano9040641

Lian, T., Huang, C., Liang, F., Li, X., & Xi, J. (2019). Simultaneously Providing Iron Source toward Electro-Fenton Process and Enhancing Hydrogen Peroxide Production via a Fe_3O_4 Nanoparticles Embedded Graphite Felt Electrode. ACS Applied Materials & Interfaces, 11(49), 45692–45701. https://doi.org/10.1021/acsami.9b16236

Liu, K., Yu, J. C.-C., Dong, H., Wu, J. C. S., & Hoffmann, M. R. (2018). Degradation and Mineralization of Carbamazepine Using an Electro-Fenton Reaction Catalyzed by Magnetite Nanoparticles Fixed on an Electrocatalytic Carbon Fiber Textile Cathode. Environmental Science & Technology, 52(21), 12667–12674. https://doi.org/10.1021/acs.est.8b03916

Liu, W., Howell, J. A., Arnot, T. C., & Scott, J. A. (2001). A novel extractive membrane bioreactor for treating biorefractory organic pollutants in the presence of high concentrations of inorganics: application to a synthetic acidic effluent containing high concentrations of chlorophenol and salt. Journal of Membrane Science, 181(1), 127–140. https://doi.org/https://doi.org/10.1016/S0376-7388(00)00496-8

Martinez, L., Leinen, D., Martín, F., Gabas, M., Ramos-Barrado, J. R., Quagliata, E., & Dalchiele, E. A. (2007). Electrochemical Growth of Diverse Iron Oxide (Fe[sub 3]O[sub 4], α-FeOOH, and γ-FeOOH) Thin Films by Electrodeposition Potential Tuning. Journal of The Electrochemical Society, 154(3), D126. https://doi.org/10.1149/1.2424416

Miao, J., Zhu, H., Tang, Y., Chen, Y., & Wan, P. (2014). Graphite felt electrochemically modified in H_2SO_4 solution used as a cathode to produce H_2O_2 for pre-oxidation of drinking water. Chemical Engineering Journal, 250, 312–318. https://doi.org/https://doi.org/10.1016/j.cej.2014.03.043

Parshetti, G. K., Telke, A. A., Kalyani, D. C., & Govindwar, S. P. (2010). Decolorization and detoxification of sulfonated azo dye methyl orange by Kocuria rosea MTCC 1532. Journal of Hazardous Materials, 176(1–3), 503–509. https://doi.org/10.1016/j.jhazmat.2009.11.058

Petrov, D. A., Lin, C. R., Ivantsov, R. D., Ovchinnikov, S. G., Zharkov, S. M., Yurkin, G. Y., … Lyubutin, I. S. (2020). Characterization of the iron oxide phases formed during the synthesis of core-shell Fe_xO_y@C nanoparticles modified with Ag. Nanotechnology, 31(39). https://doi.org/10.1088/1361-6528/ab9af2

Prasetyo, I., Akbar, F., Prabandari, A. W., & Ariyanto, T. (2019). Fenton Oxidation using Easily Recoverable Catalyst of Magnetite (Fe_3O_4) as an Efficient Approach to Treatment of Rhodamine B Dyeing Effluent in Traditional Fabrics Industry. ASEAN Journal on Science and Technology for Development, 36(3), 103–108. https://doi.org/10.29037/ajstd.592

Raghu, M. S., Yogesh Kumar, K., Prashanth, M. K., Prasanna, B. P., Vinuth, R., & Pradeep Kumar, C. B. (2017). Adsorption and antimicrobial studies of chemically bonded magnetic graphene oxide-Fe_3O_4 nanocomposite for water purification. Journal of Water Process Engineering, 17(March), 22–31. https://doi.org/10.1016/j.jwpe.2017.03.001

Rajoriya, S., Carpenter, J., Saharan, V. K., & Pandit, A. B. (2016). Hydrodynamic cavitation: An advanced oxidation process for the degradation of bio-refractory pollutants. Reviews in Chemical Engineering, 32(4), 379–411. https://doi.org/10.1515/revce-2015-0075

Sidney Santana, C., Freire Bonfim, D. P., da Cruz, I. H., da Silva Batista, M., & Fabiano, D. P. (2021). Fe2O3/MCM-41 as catalysts for methyl orange degradation by Fenton-like reactions. Environmental Progress & Sustainable Energy, 40(2), e13507. https://doi.org/https://doi.org/10.1002/ep.13507

Sobhanardakani, S., Jafari, A., Zandipak, R., & Meidanchi, A. (2018). Removal of heavy metal (Hg(II) and Cr(VI)) ions from aqueous solutions using Fe_2O_3@SiO_2 thin films as a novel adsorbent. Process Safety and Environmental Protection, 120(October), 348–357. https://doi.org/10.1016/j.psep.2018.10.002

Stoia, M., Pәcurariu, C., Istratie, R., & Nižňanský, D. (2015). Solvothermal synthesis of magnetic FexOy/C nanocomposites used as adsorbents for the removal of methylene blue from wastewater. Journal of Thermal Analysis and Calorimetry, 121(3), 989–1001. https://doi.org/10.1007/s10973-015-4641-x

Tai, H., Yang, Y., Liu, S., & Li, D. (2012). A Review of Measurement Methods of Dissolved Oxygen in Water BT - Computer and Computing Technologies in Agriculture V. In D. Li & Y. Chen (Eds.) (pp. 569–576). Berlin, Heidelberg: Springer Berlin Heidelberg.

Wu, M.-S., Ou, Y.-H., & Lin, Y.-P. (2010). Electrodeposition of iron oxide nanorods on carbon nanofiber scaffolds as an anode material for lithium-ion batteries. Electrochimica Acta, 55(9), 3240–3244. https://doi.org/https://doi.org/10.1016/j.electacta.2009.12.100

Wu, Z., Li, W., Webley, P. A., & Zhao, D. (2012). General and controllable synthesis of novel mesoporous magnetic iron oxide@carbon encapsulates for efficient arsenic removal. Advanced Materials, 24(4), 485–491. https://doi.org/10.1002/adma.201103789

Yang, H., Liang, J., Zhang, L., & Liang, Z. (2016). Electrochemical oxidation degradation of methyl orange wastewater by Nb/PbO_2 electrode. International Journal of Electrochemical Science, 11(2), 1121–1134.

Yu, F., Zhou, M., & Yu, X. (2015). Cost-effective electro-Fenton using modified graphite felt that dramatically enhanced on H_2O_2 electro-generation without external aeration. Electrochimica Acta, 163, 182–189. https://doi.org/https://doi.org/10.1016/j.electacta.2015.02.166

Yu, X., Zhou, M., Hu, Y., Groenen Serrano, K., & Yu, F. (2014). Recent updates on electrochemical degradation of bio-refractory organic pollutants using BDD anode: a mini review. Environmental Science and Pollution Research, 21(14), 8417–8431. https://doi.org/10.1007/s11356-014-2820-0

Zhou, L., Zhou, M., Hu, Z., Bi, Z., & Serrano, K. G. (2014). Chemically modified graphite felt as an efficient cathode in electro-Fenton for p-nitrophenol degradation. Electrochimica Acta, 140, 376–383. https://doi.org/10.1016/j.electacta.2014.04.090

Vol. 14 No. 1 (2023) 19-28

Jurnal Riset
Teknologi Pencegahan Pencemaran Industri

Journal homepage : https://www.jrtppi.id

Kementerian
Perindustrian
REPUBLIK INDONESIA

Impact of Reduced Activator Concentration and Curing Method on Compressive Strength of Metakaolin/Fly Ash-based Geopolymer Mortar

Andrie Harmaji*[1], Alexander Syahlendra Haimir[2], Bambang Sunendar[3]

[1] Department of Metallurgical Engineering, Faculty of Engineering and Design, Institut Teknologi Sains Bandung, Cikarang 17530, Indonesia.

[2] Department of Materials Engineering, Faculty of Mechanical and Aerospace Engineering, Institut Teknologi Bandung, Bandung 40132, Indonesia.

[3] Department of Engineering Physics, Faculty of Industrial Technology, Institut Teknologi Bandung, Bandung 40132, Indonesia.

ARTICLE INFO

Article history:
Received June 24, 2022
Received in revised form September 14, 2022
Accepted November 22, 2022
Available online May 02, 2023

Keywords :
Geopolymer
Fly Ash
Metakaolin
Alkali Activator
Sodium Carbonate

ABSTRACT

The demand for cement is increasing each year, but the manufacture of 1 tonne of cement produces an equal number of carbondioxide (CO_2) gas which is directly related to the increase in global warming. Therefore, we need a substitute material, namely geopolymer. This material has relatively superior properties compared to cement. However, one of the drawbacks of geopolymers is that the production costs are relatively more expensive compared to the manufacture of pre-cast cement because it requires chemical solutions such as sodium hydroxide (NaOH) and sodium silicate (Na_2SiO_3) to activate the precursor. This research was conducted to replace a specific ratio of alkali activator with water to reduce the use of alkaline hydroxide solutions and sodium silicate while reducing production costs.

The experiment was carried out by replacing the activator solution with water at a certain amount with a different curing method. Mechanical properties, X-Ray Diffraction (XRD), and Fourier Transform Infrared (FTIR) spectroscopy characterization were used to analyze the effect of additional water in geopolymer. The compressive test result shows that the maximum water content that can replace the activator solution is 20% by activator mass for fly ash-based geopolymers and 30% by activator mass for metakaolin-based geopolymers, with sealed and bare curing conditions before the compressive strength was decreased sharply. Substitution of 10% water in fly ash-based geopolymer increases the compressive strength to 17.20 MPa. Compressive test results and characterization showed that the optimal curing condition for fly ash-based geopolymer was sealed curing and bare curing for metakaolin-based geopolymer. The strength increase is due to O-C-O bonds representing sodium carbonate (Na_2CO_3), which affects the compressive strength of fly ash-based and metakaolin-based geopolymers.

1. INTRODUCTION

One of the primary human needs is a place to live, generally in the form of a house, or other structure, which is used as a place of shelter and residence for a long time. In addition, along with the times, the demand for buildings that support productivity in earning a living, such as offices, factories, warehouses, and other structures, is also increasing. Cement is one of the raw materials in the manufacture of concrete, which in turn becomes the building block of these structures, resulting in the demand for cement production increasing with a ten-fold increase in

---

*Correspondence author.
E-mail : harmaji.a@gmail.com (Andrie Harmaji)

doi : https://10.21771/jrtppi.2023.v14.no.1.p19-28

Accreditation number : (Ristekdikti) 158/E/KPT/2021

global consumption during the last 65 years [1,2]. Cement production is a process that requires much energy because of the high temperature required. Manufacturing 1 tonne of cement requires 4.7 million British Thermal Unit (BTU) of energy, equivalent to burning 400 lbs of coal, which produces about 1 tonne of CO_2 [3,4]. Therefore, it is necessary to provide a substitute material for cement that is more environmentally friendly and has a similar compound as cement (pozzolanic materials).

Fly ash is a residual material produced by burning coal. The residual material consists of fine particles carried by flue gas. Fly ash is also the primary component (more than 58%) formed from coal combustion [5,6]. The chemical content of fly ash varies depending on the coal burned, affecting the calcium oxide (CaO) content. Fly ash mainly consists of SiO_2, $Al2O_3$, and some trace oxides such as Fe_2O_3 and Na_2O. Metakaolin is a calcination product of kaolinite clay-based minerals such as kaolin at a temperature of 600°C - 850°C [7,8]. In this kaolin calcination process, the water between the SiO_2 and $Al2O_3$ layers will evaporate and change the kaolin into an amorphous phase, namely metakaolin. Both of these materials are common precursors in the formation of geopolymers [9,10]. Geopolymer is a zero cement material consisting of a chain or network of mineral molecules connected by covalent bonds. These chains generally consist of molecular units that contain elements such as silicon (Si), aluminum Al), and oxygen (O). The manufacturing process of geopolymer is called geopolymerization, which is strongly influenced by temperature and time.

The use of fly ash-based geopolymers and metakaolin-based geopolymers as cement substitutes is increasing because they are more environmentally friendly. The physical, chemical, and mechanical properties of geopolymer are almost the same as those of conventional concrete, even relatively better, such as compressive strength, resistance to hot and cold temperatures, and corrosion resistance [11-15]. Geopolymer concrete (GPC) is estimated to reduce 80% of the carbon footprint in construction projects compared with ordinary portland cement [16]. The disadvantage of geopolymers is that they are relatively expensive to process because they require an alkali solution to activate the aluminosilicate materials, which usually consist of alkaline compounds, compared to traditional cement-based concrete only needs water to undergo hydration. The expensive process makes the geopolymer final product cost 10-15% more than conventional concrete, which only needs water to hydrate the cement [17-19]. Several studies have already been conducted to substitute alkali activators with other liquids, such as seawater [20]. This study is conducted to replace a percentage of alkali activators with water, which will reduce the cost of the geopolymer manufacturing process. The curing method in this study was also variated. The effect on mechanical properties and microscopical characterization of geopolymer was analyzed using Compressive Test, XRD, and FTIR.

2. METHODS

The class-F fly ash was obtained from Suralaya Coal Fired Power Plant Banten. The kaolin was obtained from Bangka and fired at 850°C for 24 hours to obtain metakaolin. The oxides composition of these materials is shown in Table 1 by using X-Ray Fluorescence (XRF) method.

Figure 1. Fly ash (left) and metakaolin (right)

Table 1. Chemical composition of fly ash and metakaolin (mass%)

Oxide	Fly Ash	Metakaolin
SiO_2	52.30	65.00
Al_2O_3	26.57	33.00
CaO	6.00	0.08
Fe_2O_3	7.28	0.56
Na_2O	1.41	0.06
SO_3	0.70	-

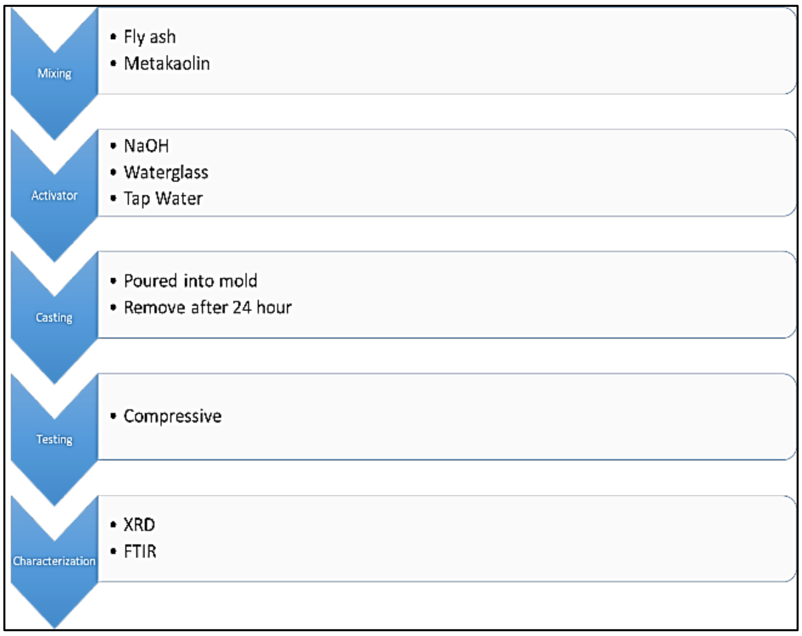

Figure 2. Flowchart of Geopolymer manufacturing

Table 2. Mix Design of fly ash-based geopolymer

No	Code	FA (g)	MK (g)	Sand (g)	NaOH (g)	Na_2SiO_3 (g)	Water (g)	Curing Method
1	FAS100	315	0	472.5	52.5	105	0	Sealed
2	FAS1090	315	0	472.5	42	84	31.5	Sealed
3	FAS2080	315	0	472.5	31.5	63	63	Sealed
4	FAS3070	315	0	472.5	21	42	94.5	Sealed
5	FAS4060	315	0	472.5	10.5	21	126	Sealed
6	FAB100	315	0	472.5	52.5	105	0	Bare
7	FAB1090	315	0	472.5	42	84	31.5	Bare
8	FAB2080	315	0	472.5	31.5	63	63	Bare
9	FAB3070	315	0	472.5	21	42	94.5	Bare
10	FAB4060	315	0	472.5	10.5	21	126	Bare

The sand for light aggregate was obtained from the local building store in Bandung. Technical grades of sodium hydroxide and water glass were purchased from a chemical store in Bandung. The flowchart and mix design for geopolymers is listed in Figure 2, Table 2, and Table 3, respectively.

The method of determining the parameter values in Tables 2 and 3 was based on the main objective of substituting alkali activator solution weight from 0-40%, because higher water content above 40% will disrupt the geopolymerization and specimens will not be hardened. The mass ratio of sodium silicate to sodium hydroxide was kept constant at 2.0. The alkali activator was prepared by mixing a NaOH solution of 12M with Na_2SiO_3. Geopolymer was made by mixing fly ash or metakaolin, an alkali activator, and water to create a slurry. It was then poured into a cubical mold with a size of 50 mm x 50 mm x 50 mm, which was in accordance with ASTM C109 “Standard Test Method for Compressive Strength of Hydraulic Cement Mortars (Using 2-in. or [50-mm] Cube Specimens)”. The specimens were cured under air exposure without protection (bare) and kept in a vacuum bag (sealed) conditions for 28 days. The hardened geopolymer's compressive strength was measured using a tensile testing machine confirmed to ASTM C-39. Debris from compression strength was collected for characterization purposes. The X-Ray Diffraction (XRD) and Fourier Transform Infrared (FTIR) Spectroscopy measurement was performed at the Instrument and Analytical Laboratory, Chemical Engineering, Institut Teknologi Bandung. The resulting diffraction pattern was compared to the Joint Committee on Powder Diffraction Standards (JCPDS).

Table 3. Mix Design of metakaolin-based geopolymer

No	Code	FA (g)	MK (g)	Sand (g)	NaOH (g)	Na_2SiO_3 (g)	Water (g)	Curing Method
1	MKS100	0	200	150	113	226	0	Sealed
2	MKS1090	0	200	150	102	203	34	Sealed
3	MKS2080	0	200	150	90	180	48	Sealed
4	MKS3070	0	200	150	79	158	102	Sealed
5	MKS4060	0	200	150	68	136	136	Sealed
6	MKB100	0	200	150	113	226	0	Bare
7	MKB1090	0	200	150	102	203	34	Bare
8	MKB2080	0	200	150	90	180	48	Bare
9	MKB3070	0	200	150	79	158	102	Bare
10	MKB4060	0	200	150	68	136	136	Bare

3. RESULT AND DISCUSSION

3.1. Compressive Strength

The compressive test produces data in the form of the maximum load the sample can receive before it is crushed, then the load is divided by the sample's surface area to get the compressive strength of each sample. The compressive strength obtained from the test for each specimen can be summarized in Table 4. In contrast, the breakdown of the effect of each precursor on the compressive strength of the geopolymer is represented in Figure 3 and Figure 4.

The compressive test results of fly ash-based geopolymers are shown in Figure 3. Water substitution for the activator decreases the compressive strength of fly ash-based geopolymer, both in sealed and bare curing. Addition of water will reduce the pH of activator, thereby reducing the presence of the geopolymerization. It also decreases pozzolanic reactivity and produces a non-solid and weak matrix caused by the addition of void spaces and unreacted particles. The compressive strength of fly ash-based geopolymer with bare curing conditions is relatively lower than the sealed cured condition, even with the same amount of water. The low compressive strength is caused by the surface of the geopolymer reacting with free air that has carbondioxide (CO_2) gas that reacts with sodium from the geopolymer, producing salt on the surface.

Suppose the curing is carried out for a long time. In that case, the reaction will not only occur on the surface but also propagate below the surface, penetrating the geopolymer, inhibiting the geopolymerization, and weakening the compressive strength.

Table 4. Compressive test results

No	Code	Water content (%)	Activator content (%)	fc (MPa)
1	FAS100	0	100	34.40
2	FAS1090	10	90	27.93
3	FAS2080	20	80	16.40
4	FAS3070	30	70	1.73
5	FAS4060	40	60	0.80
6	FAB100	0	100	16.80
7	FAB1090	10	90	17.20
8	FAB2080	20	80	13.46
9	FAB3070	30	70	2.73
10	FAB4060	40	60	0.40
11	MKS100	0	100	17.60
12	MKS1090	10	90	15.60
13	MKS2080	20	80	14.70
14	MKS3070	30	70	13.86
15	MKS4060	40	60	0.46
16	MKB100	0	100	22.53
17	MKB1090	10	90	18.46
18	MKB2080	20	80	15.80
19	MKB3070	30	70	12.13
20	MKB4060	40	60	0.67

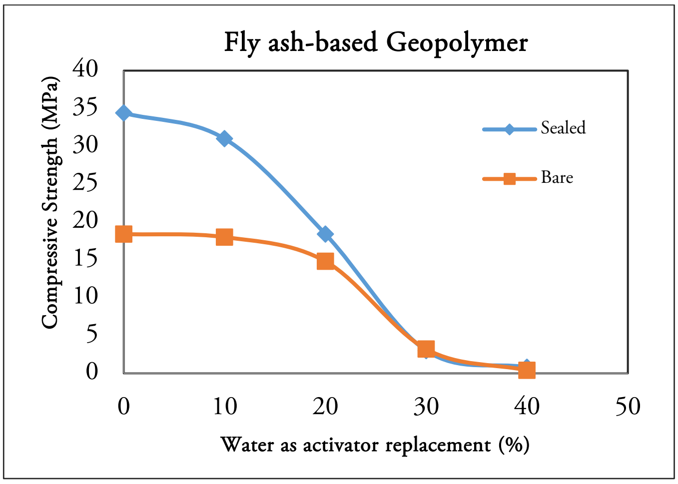

Figure 3. Compressive strength of Fly ash based geopolymer

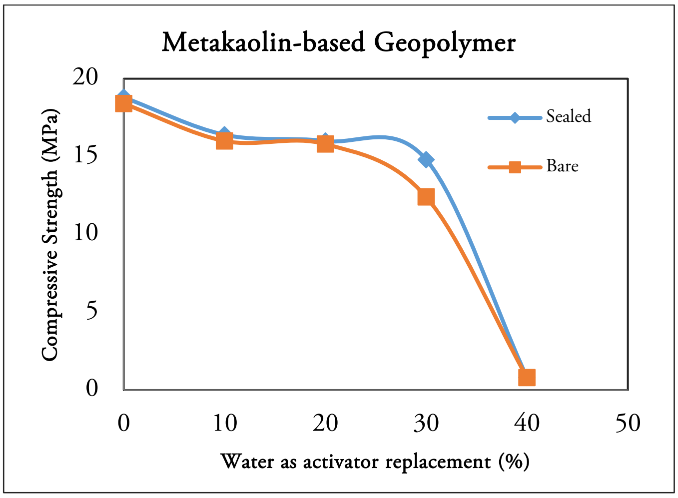

Figure 4. Compressive strength of metakaolin-based geopolymer

The compressive test results of metakaolin-based geopolymers are shown in Figure 4. It can be concluded that the compressive strength of the metakaolin-based geopolymer decreased along with an increase in the water content as an activator substitution. The compressive strength reduction is due to the reduced pozzolanic reactivity along with the increase in water content which also happened to fly ash-based Geopolymers in Figure 3 [21]. There is only a slight compressive strength difference between the bare and sealed curing method conditions, which is higher than the compressive strength of fly ash-based in the sealed curing condition. The difference is due to the relatively higher SiO_2 content in metakaolin compared to fly ash and relatively less content of other trace oxides so that water does not react with other alkali oxides (Na_2O, K_2O) to form salts. The less CaO content in metakaolin means the heat generated by geopolymer will be less than fly ash-based. Metakaolin also has a lower density than fly ash, so in the bare curing condition, the water is more easily released through the cavities between the particles, resulting in higher compressive strength. This fact also causes a less significant decrease in compressive strength with the addition of water compared to fly ash-based geopolymers.

3.2. XRD Analysis

XRD characterization was carried out on powders resulting from compression testing with a total water content of 0%, 20%, and 40% for each curing method and type of binder. XRD characterization data that has been processed with XPowder software for fly ash-based geopolymers is shown in Figures 5 and 6.

Figures 5 and 6 show that there are peaks that stand out and differ from the others. These peaks have been compared with the characteristics of the compounds in the XPowder software database. Symbols indicate the compounds formed in fly ash-based geopolymers on the fly ash-based geopolymer above the peak of the curve. The circular symbol (○) indicates the peak characterization of the mineral quartz, the star (☆) symbol indicates the peak characterization of the compound sodium alumino silicate hydrate or $Na_6(Al,Si)_{6.4}H_2O$, and the square symbol (☐) represents the mineral albite. Quartz is one of the polymorph of SiO_2 contained in fly ash.

XRD results still show the presence of quartz because the SiO2 content in the geopolymer comes from sand aggregate in the most significant amount in a geopolymer relative to the mass ratio. The compound sodium alumino silicate hydrate (NASH) has a chemical formula similar to the chemical formula for geopolymers in general, thereby proving the presence of geopolymer compounds (Na-K)-n(Si-O-)-(Si-O-Al-) or geopolymerization in each batch of fly ash-based geopolymers. The result shows that even though the amount of water is increased, the activator will still be able to react with the binders and fillers sufficiently to form geopolymers, but in less activation capacity so that they cannot produce geopolymers with high compressive strength. Similarly, albite ($NaAlSi_3O_8$) is a mineral that contains similar elements to a geopolymer structure, which are Na, Al, Si, and O.

XRD characterization data that has been processed with XPowder software for metakaolin-based geopolymers is shown in Figures 7 and 8. Similar to the characterization results on fly ash-based geopolymers, some peaks stand out more than others, and these peaks are identified using X-Powder software as certain compounds. The Quartz, NASH, and Albite are used as indicators for the formation of geopolymers or the occurrence of geopolymerization with two different binders.

Both metakaolin and fly ash are aluminosilicate compounds with almost the same Si:Al ratio (2:1), so the compounds formed after the geopolymerization process are similar. SiO_2 compounds were still detected because the amount of Si in the composition of the mixture that formed the metakaolin-based geopolymer is large. It contains metakaolin, sodium silicate, and also from sand. The intensity of SiO_2 was increased along with the addition of water content in the activator caused by the non reactant of the remaining SiO_2 compounds from metakaolin and sand, thereby reducing the compressive strength of the geopolymer. Figure 5-8 shows that quantitatively, the geopolymer with a pure alkali activator has a more amorphous phase than the geopolymer that uses water as a partial alkali activator replacement. The result explains why both compressive strengths generally decreased because water increased the crystallinity of the resulting geopolymer.

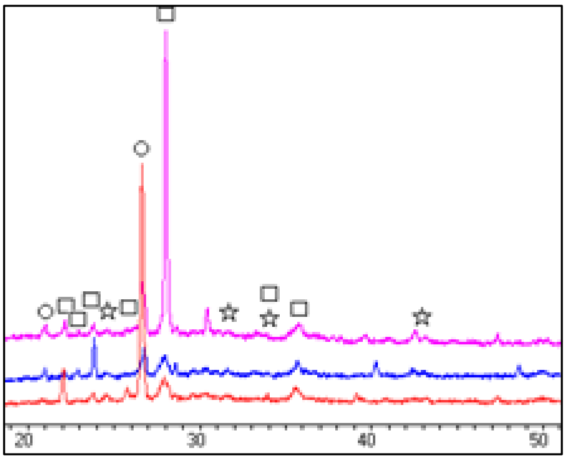

Figure 5. XRD diffractogram of fly ash-based geopolymer with sealed curing

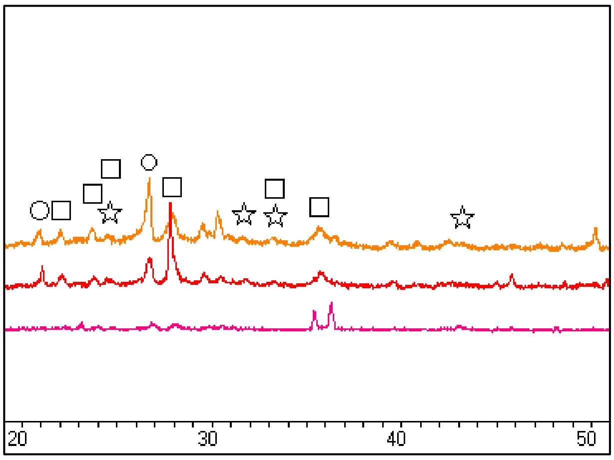

Figure 6. XRD diffractogram of fly ash-based geopolymer with bare curing

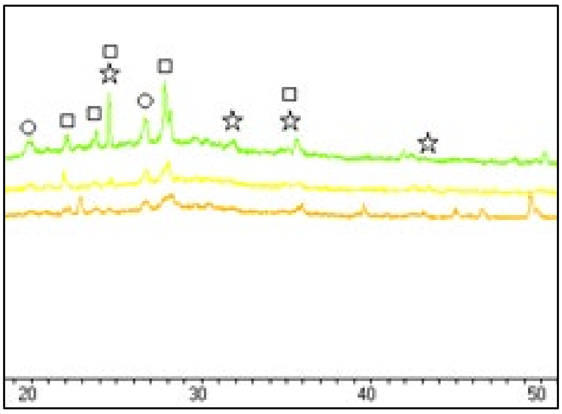

Figure 7. XRD diffractogram of metakaolin-based geopolymer with sealed curing

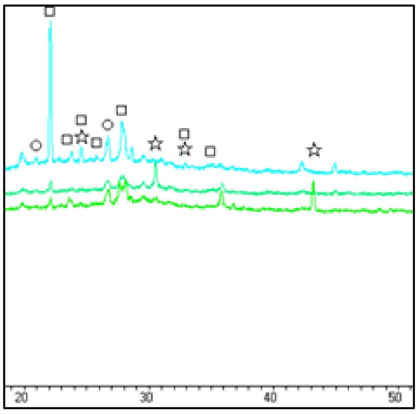

Figure 8. XRD diffractogram of metakaolin-based geopolymer with bare curing

3.3. FTIR Analysis

The result of FTIR is transmittance data for a wavelength. Each functional group or bond will have a characteristic of absorbing a specific wavelength. The resulting bonds for fly ash and metakaolin-based geopolymers were summarized in Table 5, while the wavelength versus transmittance was presented in Figure 9, Figure 10, Figure 11, and Figure 12. FTIR results have proven that the geopolymerization has successfully occurred due to Si-O-Si and Si-O-Al bonds in the samples.

The stretching Si-O-Si/Si-O-Al on fly ash base material is at wavenumber 1076.08 cm-1, while on fly ash based geopolymer with sealed curing or bare curing conditions, stretching Si-O-Si/Si-O-Al appeared at wavenumber 1012–1024 cm-1. This wavenumber shift indicates the dissolution of Si and Al elements or can be considered as geopolymerization. This result strengthens the previous XRD analysis that even though the water replaces the activator up to 40%, geopolymerization will still occur but not as well as the pure alkali activator and also explains why the compressive strength of the hardened sample is reduced.

The FAS4060 and FAB4060 samples can be seen to have different wavenumber values from other samples for stretching –OH that was caused by the excess water content in the batch, which was 40% of the weight of the activator solution, so it had a –OH bond that looked different from the others, which is the O-C-O bond. The formation occurs due to the reaction of geopolymer with CO_2 from free air when the geopolymer is treated by bare curing. The peak formed at FTIR results for the bare cured has a sharper peak at a wavenumber of about 1400 cm-1 than the sealed cured sample. The sharpness of this peak proves that the presence of O-C-O bonds is more significant in the bare cured sample because the sample interacts directly with free air.

Adding water and bare curing conditions will reduce the compressive strength due to excess -OH bonds and O-C-O bonds, both of which have compressive strength below the compressive strength of the Si-OSi and Si-O-Al geopolymer chains. The metakaolin-based geopolymer samples showed peaks in the wavenumber around 1000 cm-1, which indicated the presence of stretching Si-O-Si/Si-O-Al. There are also peaks in the wavenumbers range of 500-700 cm-1, indicating symmetric vibration Si-O-Al. The bending vibration Si-O-Si & O-Si-O appeared at wavenumber 400 cm-1. This result proves that a geopolymerization reaction has occurred, although the quantitative value is unknown.

Table 5. Summartized FTIR test results

No	Code	Stretching OH- (cm^{-1})	Bending H-O-H (cm^{-1})	Stretching O-C-O (cm^{-1})	Stretching Si-O-Si/ Si-O-Al (cm^{-1})	Symmetric Vibration Si-O-Al (cm^{-1})	Bending Vibration Si-O-Si & O-Si-O (cm^{-1})
1	FAS100	3450,65	1656,85	1413,82	1014,56	771,53	453,27
2	FAS2080	3450,65	1656,85	1413,82	1012,63	771,53	449,41
3	FAS4060	3448,72	1647,21	1406,11	1016,49	775,38	455,20
4	FAB100	3450,65	1647,21	1440,83	1016,49	775,38	447,49
5	FAB2080	3450,65	1656,85	1417,68	1016,49	773,46	457,13
6	FAB4060	3448,72	1637,56	1417,68	1024,20	775,38	447,49
7	MKS100	3448,72	1656,85	1404,18	1010,70	684,73	441,70
8	MKS2080	3448,72	1654,92	1406,11	1006,84	686,66	451,34
9	MKS4060	3450,65	1656,85	1400,32	1020,34	688,59	443,63
10	MKB100	3450,65	1656,85	1415,75	1010,70	682,80	451,34
11	MKB2080	3448,72	1656,85	1433,11	1010,70	688,59	443,63
12	MKB4060	3448,72	1656,85	1450,47	1026,13	686,66	457,13

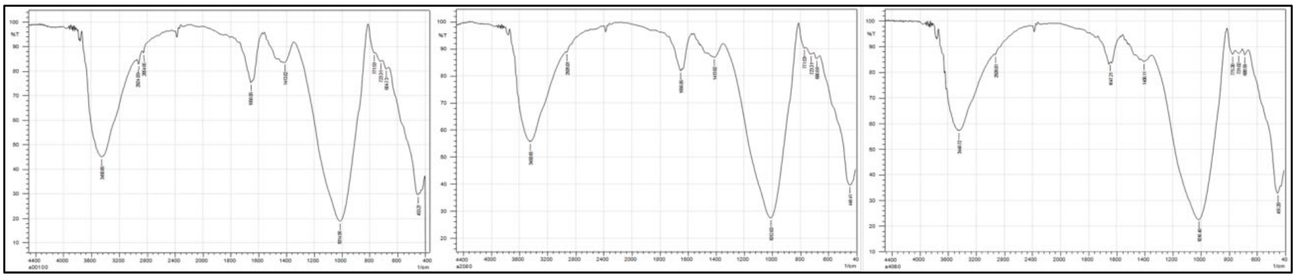

Figure 9. FTIR test results of FAS100, FAS2080, and FAS4060, left to right

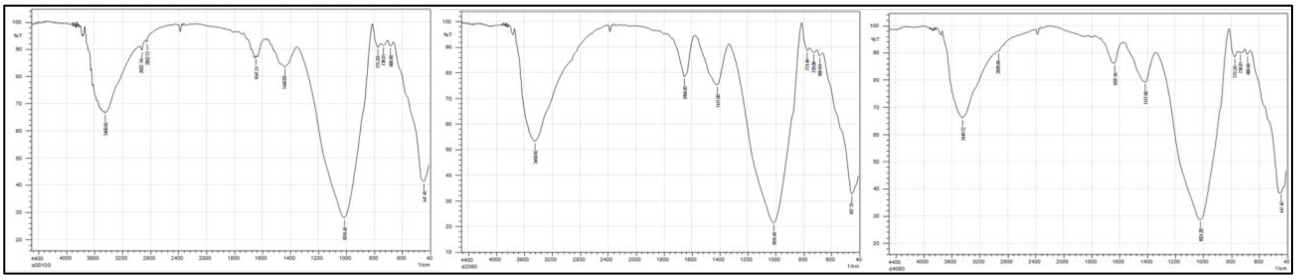

Figure 10. FTIR test results of FAS100, FAB2080, and FAB4060, left to right

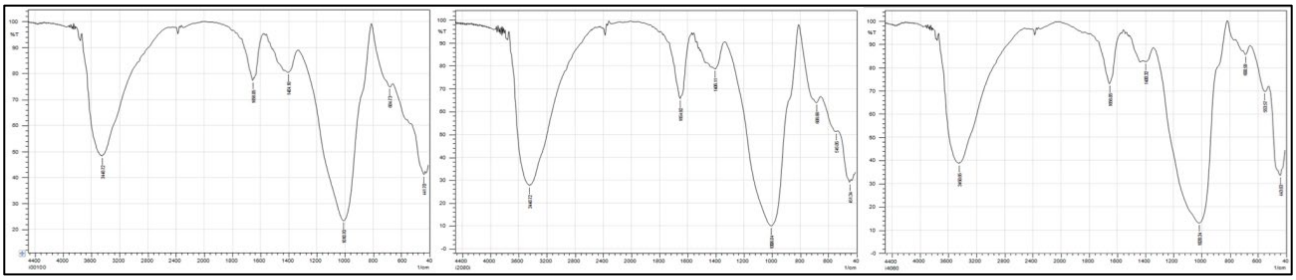

Figure 11. FTIR test results of MKS100, MKS2080, and MKS4060, left to right

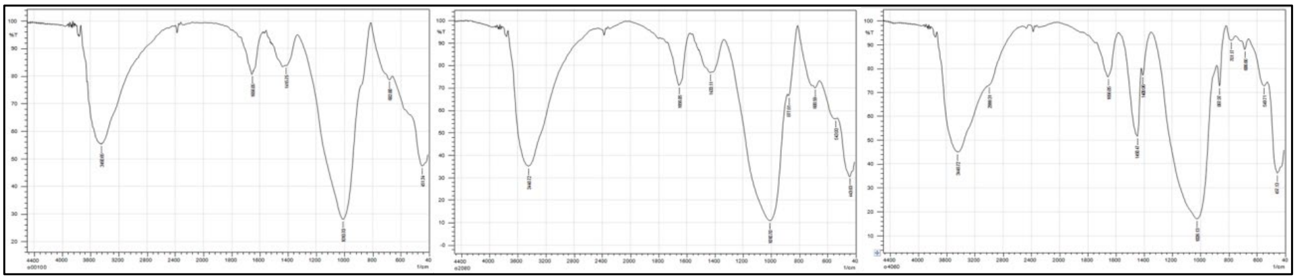

Figure 12. FTIR test results of MKB100, MKB2080, and MKB4060, left to right

The increase in –OH and H-O-H bonds are due to the reaction with water from the free air and the water content in the activator solution in the bare curing and water-containing batch. Trona or sodium bicarbonate is also formed, indicated by stretching O-C-O in each sample. This bond most likely occurs due to the interaction of the sample with CO_2 gas contained in the free air. These bonds were detected in all samples at the wavenumber of around 1400 cm-1 on the bare cured metakaolin-based geopolymer sample. It has sharper peaks than the geopolymer cured by the sealed method. The sharper peak indicates a more significant O-C-O bond due to the bare curing condition, which reacts directly with free air.

4. CONCLUSION

From this study, it can be concluded that the compressive test results have shown that the maximum water replacement for the activator solution in fly ash-based geopolymer was 20% under both curing conditions since the addition of higher water content will sharply decrease the compressive strength. However, the activator solution in metakaolin-based geopolymer can be substituted by water up to 30% before undergoing a significant compressive strength decrease. Generally, when water partially replaces the alkali activator, the compressive strength of metakaolin and fly ash-based geopolymer will decrease, except for substituting 10% water in fly ash-based geopolymer, which increases the compressive strength to 17.20 MPa. The difference is due to water having lowered the molarity of NaOH, which is better suited for the fly ash for geopolymerization than a pure alkali activator.

The fly ash-based and metakaolin-based geopolymer compression tests showed that the sealed curing condition resulted in higher compressive strength. The geopolymerization is proven by the XRD characterizations, which showed the formation of NASH and Albite compounds. FTIR characterizations showed the presence of O-C-O bonds as the representation of Trona formed, reducing the compressive strength of Geopolymers.

ACKNOWLEDGEMENT

We thank Advanced Materials Processing Laboratory, Institut Teknologi Bandung the support for this study.

REFERENCE

Aliabdo, A. A., Abd Elmoaty, A. E. M., & Salem, H. A. (2016). Effect of water addition, plasticizer and alkaline solution constitution on fly ash based geopolymer concrete performance. Construction and Building Materials, 121, 694–703.

Alterary SS, Marei, NH. Fly ash properties, characterization, and applications: A review. Journal of King Saud University – Science 2021; 33(6), p. 101536.

Amran, M, Al-Fakih, A, Chu, SH, Fediuk, R, Haruna, S, Azevedo, A, Vatin, N. Long-term durability properties of geopolymer concrete: An in-depth review. Case Studies in Construction Materials 2021;15, e00661.

Belaid F. How does concrete and cement industry transformation contribute to mitigating climate change challenges?. Resources, Conservation & Recycling Advances. 2022;15, 200084.

Castillo H, Collado H, Droguett T, Sánchez S, Vesely M, Garrido P, Palma S. Factors Affecting the Compressive Strength of Geopolymers: A Review. Minerals. 2021; 11(12):1317

Castillo, H, Collado, H, Droguett, T, Vesely, M, Garrido, P and Palma, S. State of the art of geopolymers: A review. e-Polymers 2022;22(1), pp. 108-124.

de Oliveira, L. B., de Azevedo, A. R. G., Marvila, M. T., Pereira, E. C., Fediuk, R., & Vieira, C. M. F. Durability of geopolymers with industrial waste. Case Studies in Construction Materials 2022;16, e00839.

Fayomi GU, et al. Perspectives on environmental CO2 emission and energy factor in Cement Industry IOP Conf. Ser.: Earth Environ. Sci. 2019;331 012035.

Harmaji, A.. Seawater as Alkali Activator in Fly Ash Based Geopolymer. Engineering, MAthematics and Computer Science (EMACS) Journal 2022; 4(2), 45–49.

Jindal, B.B., Alomayri, T., Hasan, A. et al. Geopolymer concrete with metakaolin for sustainability: a comprehensive review on raw material's properties, synthesis, performance, and potential application. Environ Sci Pollut Res 2022.

Kaze CR, Tchakouté HK, Mbakop TT, Mache JR, Kamseu E, Melo UC, Leonelli C, Rahier H. Synthesis and properties of inorganic polymers (geopolymers) derived from Cameroon-meta-halloysite. Ceram. Int. 2018;44, pp. 18499-18508.

Klima, KM, Schollbach, K, Brouwers, HJH, & Yu, Q. Thermal and fire resistance of Class F fly ash based geopolymers – A review. In Construction and Building Materials 2022;323, p. 126529.

Luukkonen, T, Tolonen, ET, Runtti, H et al. Optimization of the metakaolin geopolymer preparation for maximized ammonium adsorption capacity. J Mater Sci 2017;52, 9363–9376.

Monteiro PJ, Miller SA, Horvath A. Towards sustainable concrete. Nat. Mater. 2017;16 (7), pp. 698-699.

Morla P, Gupta R, Azarsa P, Sharma A. Corrosion Evaluation of Geopolymer Concrete Made with Fly Ash and Bottom Ash. Sustainability. 2021; 13(1):398.

Rajini, B, Rao, AVN, Sashidhar, C. COST ANALYSIS OF GEOPOLYMER CONCRETE OVER CONVENTIONAL CONCRETE. International Journal of Civil Engineering and Technology (IJCIET) 2020; 11(2), pp. 23-30.

Sanjuán MÁ, Andrade C, Mora P, Zaragoza A. Carbon Dioxide Uptake by Cement-Based Materials: A Spanish Case Study. Applied Sciences. 2020; 10(1):339.

Shcherban' EM, Stel'makh SA, Beskopylny A, Mailyan LR, Meskhi B. Increasing the Corrosion Resistance and Durability of Geopolymer Concrete Structures of Agricultural Buildings Operating in Specific Conditions of Aggressive Environments of Livestock Buildings. Applied Sciences. 2022; 12(3):1655.

Sun, Q, Peng, Y, Georgolamprou, X, Li, D, Kiebach, R. Synthesis and characterization of a geopolymer/hexagonal-boron nitride composite for free forming 3D extrusion-based printing. Applied Clay Science 2020;199, 105870

Verma M, Dev N, Rahman I, Nigam M, Ahmed M, Mallick J. Geopolymer Concrete: A Material for Sustainable Development in Indian Construction Industries. Crystals. 2022; 12(4):514.

Vilakazi AQ, Ndlovu S, Chipise L, Shemi A. The Recycling of Coal Fly Ash: A Review on Sustainable Developments and Economic Considerations. Sustainability. 2022; 14(4):1958.

Vol. 14 No. 1 (2023) 29-39

Jurnal Riset
Teknologi Pencegahan Pencemaran Industri

Journal homepage : https://www.jrtppi.id

Evaluation of Diesel Engine Performance Using Biodiesel from Cooking Oil Waste (WCO)

Suardi*[1], Wira Setiawan[1], Andi Mursyd Nugraha[1], Alamsyah[1], Rodlian Jamal Ikhwani[1]

[1] Shipping Engineering Study Program, Institut Teknologi Kalimantan, Balikpapan, Indonesia.

ARTICLE INFO

Article history:
Received August 1, 2022
Received in revised form December 28, 2022
Accepted February 09, 2023
Available online May 02, 2023

Keywords :
Biodiesel
Diesel Engine
Engine Performance
Fuel Temperature
Waste Cooking Oil (WCO)

ABSTRACT

The increasing use of fossil fuels will cause the world's oil reserves to be depleted. In this case, it is necessary to increase the use of alternative renewable fuels, one of which is biodiesel waste cooking oil (WCO). The method used is an experimental test with a mixture of used cooking oil biodiesel and fuel. Before testing, the temperature of each fuel is increased to determine the effect of temperature on the density and viscosity values. The highest density value is found in B50 fuel at 26 °C, with a density of 0.854 gr/ml, while the lowest density is found in diesel fuel at 60 °C, with a density of 0.822 gr/ml. The highest viscosity value is found in B50 fuel at 26 °C and 60 °C, which is 3.26 cSt. After that, testing was carried out on a diesel engine, which produced the highest thermal efficiency value of 21.16% on B50 fuel with a temperature of 60 °C at 1000 rpm rotation and a load of 4000 watts. The lowest thermal efficiency of 6.43% was found in B50 fuel with a temperature of 26 °C at 800 rpm and a load of 1000 watts. The lowest consumption was found in B30 with a temperature of 60 °C at 1200 rpm, which was 420.78 gr/kWh. From the results of the tests that have been carried out, it can be concluded that the lower the density and viscosity of the fuel, the better the performance of the diesel engine on average. High temperatures effectively make the engine performance value better than normal temperatures (26 °C), and the performance of diesel engines is better with WCO fuel, especially in SFC.

1. INTRODUCTION

The purpose of machines is to facilitate and support work activities to meet human needs. With the passage of time, the need for machines is increasing, especially in the fields of industry and transportation. The known types of engines are gasoline engines and diesel engines. In the world of marine transportation, such as ships, the engine can function as a generator or as a prime mover system. In principle, diesel engines and gasoline engines (internal combustion engines) can be interpreted as energy converters that convert the energy from fuel combustion into mechanical energy (effective work) (Tschoeke, 2006).

Diesel engines have different characteristics from other internal combustion engines because the method of ignition in the combustion chamber on a diesel engine does not use spark plugs, but instead fuel is injected into the combustion chamber and then compressed with high-pressure air (Tschoeke, 2006). This has an impact on the level of thermal efficiency of the diesel engine or compression ignition engine (CI engine), which is better than that of the gasoline engine or spark ignition engine (SI engine), resulting in higher fuel efficiency (Fil & Akansu, 2022). However, even though the level of fuel use is quite efficient, the use of diesel engines has greatly increased, and the amount of diesel fuel used is also increasing, which, on the other hand, is depleting fossil fuel supplies. Therefore, many efforts have been made to find renewable and

---

*Correspondence author.
E-mail : suardi@lecturer.itk.ac.id (Suardi)

doi : https://10.21771/jrtppi.2023.v14.no.1.p29-39

Accreditation number : (Ristekdikti) 158/E/KPT/2021

environmentally friendly fuels. One of these is biodiesel, which is a renewable biofuel and has more environmentally friendly properties (Duhovnik, 2008).

Currently, Indonesia is implementing the EURO-4 standard regarding engine exhaust emission restrictions, to reduce the level of environmental pollution caused by engine exhaust gases (Kementerian ESDM, 2021). Several studies have been carried out related to fuel modification to produce low emissions. One study found that the mixing of Methanol into biodiesel fuel can reduce engine exhaust emissions (Fathallah et al., 2022). Another study states that the addition of Methanol is effective in reducing hydrocarbon levels and carbon monoxide emissions because the fuel can burn completely when injected into the combustion chamber (Panda & Ramesh, 2021). Considering the fact that petroleum is increasingly scarce, biodiesel has the potential to replace fossil fuels in the future.

Various types of food, such as soybeans and corn, can serve as raw materials for the production of biodiesel fuels, as evidenced by studies conducted by Bernard Freedman (1986) and Lang et al. (2001). Additionally, waste cooking oil (WCO) and palm oil waste can also be utilized as viable alternatives for biodiesel fuel production. In Indonesia, the use of WCO as a raw material for biodiesel production shows significant potential as it falls under alternative renewable fuels. Furthermore, this biodiesel can be a viable substitute for diesel fuel due to its comparable composition and properties. Given the high domestic demand for cooking oil in Indonesia, which amounts to 78,294 tons every 14 days (Kementerian Perindustrian RI, 2022), the use of WCO for biodiesel production can potentially mitigate waste and provide an alternative fuel source.

There are five major palm oil producing countries in the world, with Indonesia ranking first. Southeast Asian countries, namely Indonesia, Malaysia, and Thailand, as well as two other countries, namely Colombia and Nigeria, dominate palm oil production (Indexmundi, 2022). Indonesia's oil palm plantation areas expand annually, resulting in an increase in palm oil production, which indirectly contributes to the increasing amount of WCO. Indonesia alone produces approximately 6.46-9.72 million kiloliters of WCO per year (Direktorat Jenderal EBTKE, 2022). Apart from its relatively abundant availability, the waste of WCO in the environment can cause environmental pollution in the form of an increase in Chemical Oxygen Demand (COD) and Biochemical Oxygen Demand (BOD) in water bodies, which can lead to a foul odor (Hosseinzadeh-Bandbafha et al., 2022; Prasetyo, 2018).

Transesterification is a chemical process that is carried out to convert triglycerides in vegetable oil into biodiesel. This process removes the triglycerides and results in a lower viscosity of the biodiesel (SRS Biodiesel, 2022). The viscosity and density of the fuel are crucial factors to consider for proper distribution to the injector for injection. High viscosity can cause the engine to work harder. The viscosity grade of fuel for diesel engines should be between 2 mm^2/s to 5 mm^2/s, and the density should be between 815 kg/m^3 to 880 kg/m^3 (Direktorat Jenderal ESDM, 2020).

2. METHODS

This research is based on references from Google Scholar (Google Scholar, 2022) and ScienceDirect (ScienceDirect, 2022) that are related to the process of producing and using WCO biodiesel and measuring engine performance using WCO biodiesel. Two methods will be used in this research, namely the transesterification method (Suzihaque et al., 2022) for the production of WCO biodiesel and an experimental method to test the performance of diesel engines. Based on previous research on fuel temperature variations, it has been shown that increasing fuel temperature has a positive effect on engine performance because it improves fuel spraying and evaporation, resulting in better flame and engine efficiency, and lower exhaust emissions (Choi et al., 2022).

In this study, six fuel samples were prepared. The six samples including 100% diesel oil at room temperature (26 °C) and 60 °C, 30% WCO biodiesel with temperature variations of 26 °C and 60 °C, and 50% WCO biodiesel with temperature variations of 26 °C and 60 °C. The use of temperature variations of 26 °C and 60 °C is intended to increase the viscosity level of the fuel, thereby optimizing the fuel injection process and improving the process of fuel atomization and combustion in the engine cylinder.

Upon completion of the biodiesel production process, the fuel underwent viscosity and density testing according to the domestic diesel fuel specifications standards outlined by the Ministry of Energy and Mineral Resources Republic of Indonesia (Direktorat Jenderal ESDM, 2020). Subsequently, the performance of WCO biodiesel fuel was directly tested on a 4-stroke diesel engine, where a generator and lights were utilized as a load. Engine power, torque, Specific Fuel Oil Consumption, and Thermal Efficiency were among the parameters assessed. The Yanmar TF 85-MH 4 Stroke diesel engine (YANMAR Indonesia, 2022) was employed for the test. Although other vegetable oils such as corn oil, coconut oil, candlenut oil, and animal fat-derived oils are available, this research primarily focuses on the use of WCO or used cooking oil. The abundance of WCO as a raw material and its potential to reduce waste are some of the reasons for this emphasis. The research setting is presented in Figure 1.

Stages of testing are carried out in four stages, such as:

a) The test was carried out in three variations of engine speed, namely (800 Rpm, 1000 Rpm, and 120 Rpm)
b) For each variation of engine speed, the lamp load used when testing the machine will be determined (the load is carried out in stages starting from zero load or no lights are on, 1000 watts of load, 2000 watts of load, 3000 watts of load, and 4000 watts of load)
c) The more the load increases, the engine speed decreases, so during the loading process, the engine speed must be set at 800 Rpm or 1000 Rpm, or 1200 Rpm.
d) In the process of running the engine, measurements of voltage, current, amount of fuel consumption, fuel consumption time, and engine speed are measured.

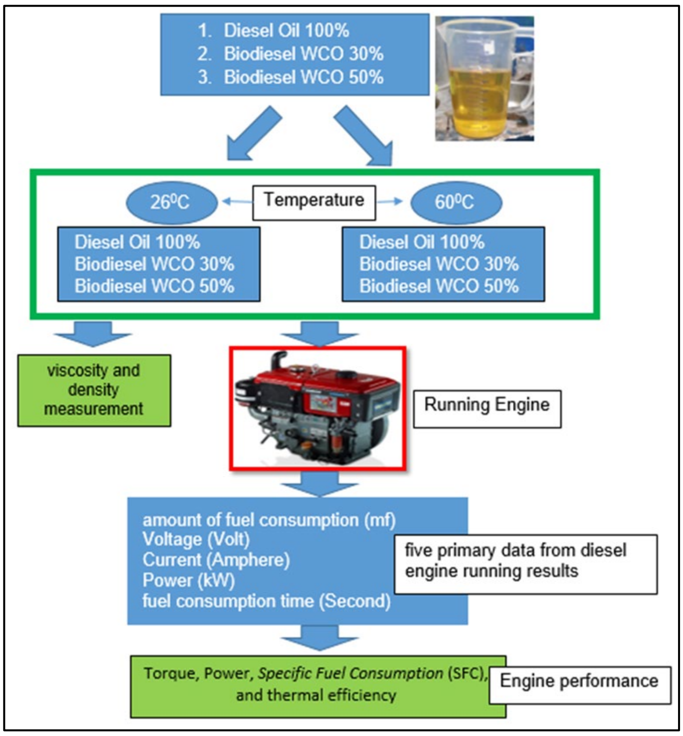

Figure 1. Research Setting

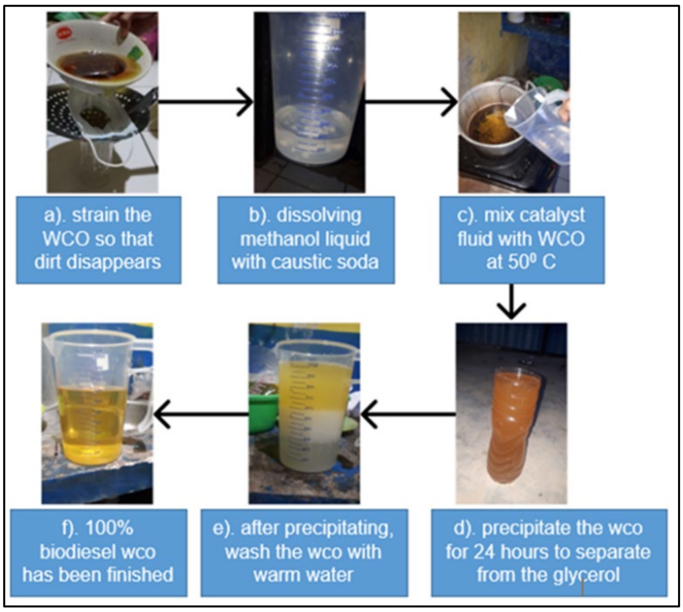

Figure 2. WCO biodiesel Manufacturing Process

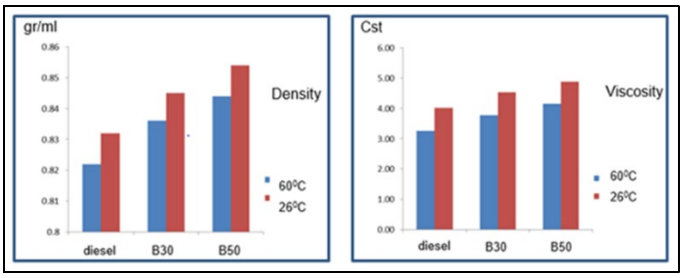

Figure 3. Graphics The results of density and viscosity testing on diesel, B30, and B50 with variations temperature 26 °C and 60 °C

Before biodiesel is tested on a diesel engine, the process of making biodiesel WCO is carried out first. The process for making WCO biodiesel can be seen in Figure 2. The process of producing biodiesel from WCO begins with filtering WCO to separate oil and frying residue, in this study the amount of WCO used is 1 liter, the next step is to dissolve the catalyst methanol (CH_3OH) and caustic soda (NaOH) as much as 200 ml. The filtered WCO is then heated until the temperature reaches 50 °C and mixed with the catalyst liquid that has been made previously. The filtered WCO is then heated until the temperature reaches 50 °C and mixed with the catalyst liquid that has been made previously, after that, the WCO is then allowed to stand for 24 hours to separate the oil and glycerol (fat), then the WCO oil that has been precipitated for 24 hours is separated from glycerol and washed using warm water. The washing process is carried out two to three times to obtain WCO biodiesel which is clearer and lighter in color.

3. RESULT AND DISCUSSION

3.1. Testing the Density and Viscosity of Diesel and Biodiesel Fuels with Variations of Heating

The viscosity and density of the fuels were tested using a viscometer and aerometer. Table 1 shows the results of the density and viscosity tests for Diesel Oil, WCO B30, and WCO B50 at both 26 °C and 60 °C.

The graph of the test results of the properties of Diesel oil, B30, and B50 fuels in two temperature variations 26 °C and 60 °C can be seen in Figure 3.

The graph depicted in Figure 3 demonstrates that viscosity and density values of the fuel decrease as the fuel temperature rises. Additionally, the density and viscosity values of the fuel are influenced by the quantity of WCO mixture used, whereby increasing the amount of WCO mixed raises the density and viscosity of the fuel. It should be noted that the density value obtained from the aforementioned tests remains within the range of limits set by the Ministry of Energy and Mineral Resources Republic of Indonesia, as detailed in Table 2 below.

3.2. Engine Testing

This stage is conducted to evaluate the performance of the diesel engine using conventional fuel, namely diesel. In this study, a 4-stroke Yanmar TF 85-MH diesel engine with 1 cylinder was utilized (YANMAR Indonesia, 2022). The complete specifications of the diesel engine used in the experiment can be found in Table 3.

The experimental setting of engine used can be seen in Figure 4.

Table 1. Properties of Diesel Oil, B30, and B50 with variations temperature 26 °C and 60 °C

Fuel Oil	Temperature	Density (gr/ml)	Viscosity (cSt or mm^2/s)
Diesel	26 °C	0.832	4.01
B30	26 °C	0.845	4.53
B50	26 °C	0.854	4.89
Diesel	60 °C	0.822	3.26
B30	60 °C	0.836	3.77
B50	60 °C	0.844	4.15

Table 2. Biodiesel Specifications set by Ministry of Energy and Mineral Resources Republic of Indonesia

Characteristic	Unit	Min Value	Max Value	Methods
Density	gr/ml	0.815	0.88	ASTM D4052/1298
Viscosity	cSt or mm^2/s	2	5	ASTM D445

(Source : Direktorat Jenderal ESDM, 2020)

Table 3. Diesel Engine specifications

Main Engine	Value	Unit
Model	1 cylinder, 4 Stroke	Vertical
Type	Yanmar, TF 85 MH	
Continous Power	7,5	Kw
Engine Speed	2200	Rpm
Displacement	493	cc
Compression Ratio	18	
Dimention	672x330x496	mm
Weight	87,0	Kg
Main Engine	Value	unit

(Source : YANMAR Indonesia, 2022)

Torque Comparison Analysis with Load at 800 RPM

Based on the test results data above, it can be calculated the torque generated on the diesel engine with the following equation:

$$P = 2\ (\pi n/60)\ T \qquad (1)$$

Where:

P = Power (W)
n = Engine speed (Rpm)
T = Torque generated (Nm)

So to get the torque value, the equation is:

$$T = (P \times 60)/(2\pi n) \qquad (2)$$

With the above equation, it can be calculated torque as follows:

$$T = ((258.85)\ x\ 60)/(2(3.14)(800))$$
$$T = 3.0886\ Nm$$

Based on the calculations above, a graph of the comparison between torque and load at 800 RPM rotation with fuel variations is obtained, namely diesel fuel, B30, and B50 in 26 °C and 60 °C temperatures as shown in Figure 5 below:

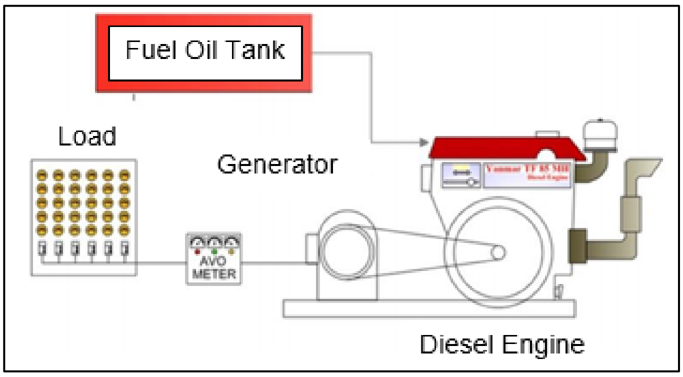

Figure 4. Schematic diagram of diesel engine testing (Source : Suardi, 2019)

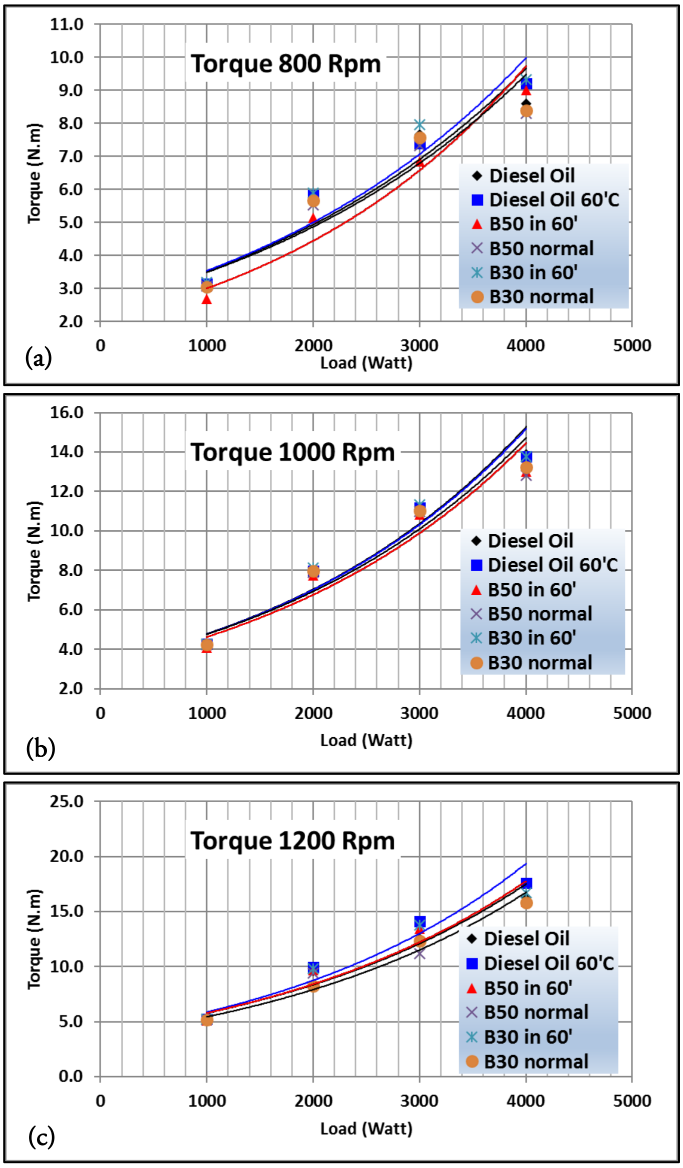

Figure 5. Torque comparison graph with load for each RPM (a) 800 RPM, (b) 1000 RPM, (c) 1200 RPM.

Table 4. Torque in various RPM and Load

RPM	Load (Watt)	Torque (N.m)					
		Diesel Oil	Diesel Oil (60^0)	B50 (26^0)	B50 (60^0)	B30 (26^0)	B30 (60^0)
800	1000	3.09	3.15	3.08	2.68	3.05	3.18
	2000	5.72	5.82	5.52	5.15	5.66	5.88
	3000	7.66	7.40	7.32	6.86	7.56	7.95
	4000	8.59	9.20	8.31	9.01	8.38	9.32
1000	1000	4.27	4.26	4.22	4.10	4.22	4.29
	2000	8.01	7.98	7.89	7.75	7.96	8.11
	3000	11.21	11.17	10.99	10.83	11.03	11.33
	4000	13.90	13.77	12.82	13.01	13.26	13.77
1200	1000	5.18	5.25	5.18	5.10	5.18	5.26
	2000	9.63	9.98	9.43	9.67	8.22	9.83
	3000	12.52	14.08	11.20	13.42	12.34	13.78
	4000	16.29	17.57	12.25	15.91	15.78	16.67

The calculation results for torque at load variations and RPM can be seen in Table 4.

Table 4 presents the torque-to-load ratio of diesel, B30, and B50 fuels at 800 RPM rotation and variations in temperature, namely 26°C and 60°C. The highest torque value is obtained from the B30 fuel at a temperature of 60°C and a load of 4000 watts, with a torque value of 9.32 Nm for 1000 RPM rotation. The highest value is found in the diesel fuel graph at 26°C with a load of 4000 watts and a torque value of 13.90 Nm for 1200 RPM rotation. The graph of diesel fuel with a temperature of 60°C at a load of 4000 watts yields the highest value, with a torque value of 17.57 Nm.

Based on the graph and table above, it can be inferred that there is a direct proportionality between the magnitude of load applied and the corresponding increase in torque. This observation is consistent with other studies on engine performance, which also report that increasing engine load leads to a corresponding increase in torque (Fathallah et al., 2022; Panda & Ramesh, 2021). The highest average torque value across all RPM ranges is observed in diesel fuel with a temperature of 60°C, which measures 9.14 Nm. Conversely, the lowest average torque value is seen in B50 fuel with a temperature of 26°C, which measures 8.19 Nm. This observation aligns with visual observations of diesel engines, which often produce higher vibration and noise, and exhibit unstable engine speed at lower torque values.

Comparative Analysis of SFC with Load at 800 RPM

Based on the data from the research above, it can be calculated the SFC generated in the diesel engine with the following equation:

$$SFC = mf/P\ 10^3 \qquad (3)$$

Where:

SFC = Specific Fuel Consumption (g/kWh)
mf = Fuel flow rate (kg/hour)
P = Power generated (kW)

In which case, the value of the fuel flow rate can be calculated by the following equation:

$$mf = (\rho.vf)/tf \times 3600 \qquad (4)$$

Where:

ρ = Density (kg/liter)
vf = Volume of fuel (liters)
tf = Time for fuel consumption as much as vf (hours)

With the above equation, it can be calculated SFC as follows:

$$mf = ((0.832).(0.02))/(175\ x\ 3600)$$
$$mf = 0{,}3423$$

then get the value of SFC

$$SFC = 1030.3423/0.2589$$

$$SFC = 1322.42\ gr/kWh$$

Based on the above calculations, a comparison graph between SFC and load at 800 RPM rotation with fuel variations is obtained, namely diesel fuel, B30, and B50 with 26 °C and 60 °C temperature as shown in Figure 6 below:

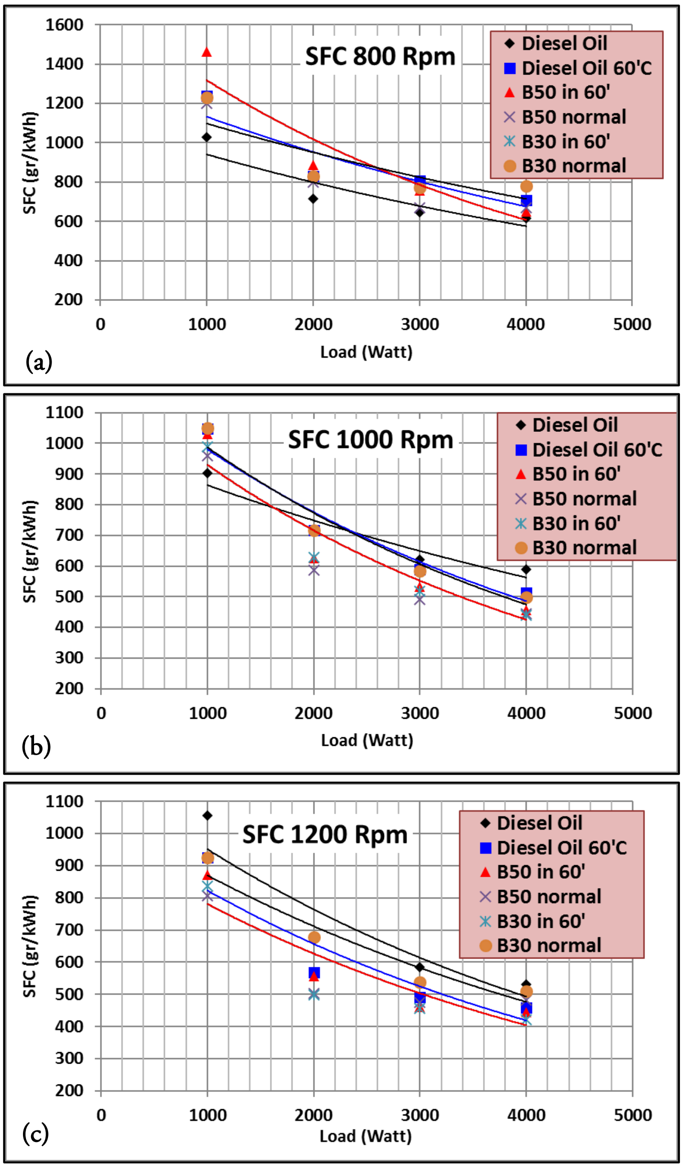

Figure 6. Comparison graph of SFC with Load for each RPM (a) 800 RPM, (b) 1000 RPM, (c) 1200 RPM

The calculation results for SFC on load variations and RPM can be seen in Table 5.

Figure 6 and Table 5 present a comparison of specific fuel consumption (SFC) to the load with variations in diesel fuel, B30, and B50 at 26 °C and 60 °C and 800 RPM rotation. The graph shows that the highest SFC value is found in the B50 fuel graph with a temperature of 60 °C at a load of 1000 watts with an SFC value of 1461.83 gr/kWh. Meanwhile, for 1000 RPM rotation, the highest SFC value is found on the graph of B30 with 26 °C at a load of 1000 watts with an SFC value of 1051.25 gr/kWh. For 1200 RPM rotation, the highest SFC value is found on the graph of diesel fuel at a load of 4000 watts with an SFC value of 1056.55 gr/kWh.

Based on the graph and table above, it can be concluded that lower SFC values are generally achieved at engine speeds of 1000 RPM and above. This is consistent with previous research on engine performance, and the current study also demonstrates that biodiesel is more efficient than Diesel Oil. Furthermore, the thermal efficiency of the diesel engine can be calculated using the data obtained from the engine running results with the following equation:

$$t = W/Ep \times 100\% \qquad (5)$$

Where :

W = Work done by the engine (kJ)

Ep = Fuel energy in a given time (kJ)

Meanwhile, the chemical potential energy of the fuel can be calculated by the formula:

$$Ep = mf \times LHV \times t \qquad (6)$$

Where LHV is the lower calorific value of the fuel in kJ/kg. It is known that the LHV value of Diesel Oil is 41,915 kJ/kg, B30 is 39,735 kJ/kg, and B50 is 38,283 kJ/kg.

So, the equation of thermal efficiency becomes as follows:

$$t = W/Ep \times 100\%$$

$$= 100\%\ (P.t)/(mf.LHV)$$

$$= 100\%\ (P.3600)/(mf.LHV)$$

Where P is in units of kW, mf is in units of kg/hour, and LHV is in units of kJ/kg.

Table 5. SFC in various RPM and Load

RPM	Load (Watt)	SFC (gr/kWh)					
		Diesel Oil	Diesel Oil (60^0)	B50 (26^0)	B50 (60^0)	B30 (26^0)	B30 (60^0)
800	1000	1028.55	1239.65	1201.15	1461.83	1228.75	1146.39
	2000	714.07	830.40	800.18	885.52	828.09	757.29
	3000	647.86	805.26	667.74	759.04	773.96	686.69
	4000	616.56	706.03	669.22	651.26	780.19	628.02
1000	1000	904.00	1048.74	958.32	1030.66	1051.25	988.56
	2000	713.72	716.15	585.93	625.82	715.51	628.19
	3000	622.01	588.31	489.87	531.50	584.98	517.89
	4000	587.76	512.51	444.42	455.85	497.83	439.19
1200	1000	1056.55	926.42	806.41	871.03	924.32	835.83
	2000	668.61	568.56	503.73	555.58	676.89	497.40
	3000	585.48	490.58	474.56	461.36	537.45	456.06
	4000	531.95	459.60	481.05	445.57	511.09	420.78

Table 6. Efficiency in various RPM and Load

RPM	Load (Watt)	Eff thermal (%)					
		Diesel Oil	Diesel Oil (60^0)	B50 (26^0)	B50 (60^0)	B30 (26^0)	B30 (60^0)
800	1000	8.35	6.93	7.83	6.43	7.37	7.90
	2000	12.03	10.34	11.75	10.62	10.94	11.96
	3000	13.26	10.67	14.08	12.39	11.71	13.19
	4000	13.93	12.16	14.05	14.44	11.61	14.45
1000	1000	9.50	8.19	9.81	9.12	8.62	9.16
	2000	12.03	11.99	16.05	15.03	12.66	14.42
	3000	13.81	14.60	19.20	17.69	15.49	17.49
	4000	14.61	16.76	21.16	20.63	18.20	20.63
1200	1000	8.13	9.27	11.66	10.80	9.80	10.84
	2000	12.85	15.11	18.67	16.93	13.38	18.21
	3000	14.67	17.51	19.82	20.38	16.86	19.87
	4000	16.15	18.69	19.55	21.10	17.73	21.53

With the above equation, it can be calculated thermal efficiency as follows:

$$t = \frac{0.259\ kW}{0.342\ kg/jam} \times 41915\ kJ/kg \times 3600 \times 100$$

$$t = 6.49\%$$

Based on the calculations presented above, a graph was generated to compare thermal efficiency with load at 800 RPM rotation using different fuel variations, including diesel fuel, B30, and B50 at temperatures of 26°C and 60°C. The resulting graph is shown in Figure 7.

The calculation results for Thermal Efficiency on load variations and RPM can be seen in Table 6.

Based on the results presented in Figure 7 and Table 6, it can be observed that the highest thermal efficiency values are obtained when using B30 and B50 fuels with temperatures of 60°C and load of 4000 watts. Specifically, the B30 fuel with 60°C temperature shows the highest thermal efficiency value of 14.45% at 800 RPM rotation. At 1000 RPM rotation, the B50 fuel with 60°C temperature and load of 4000 watts shows the highest thermal efficiency value of 21.16%.

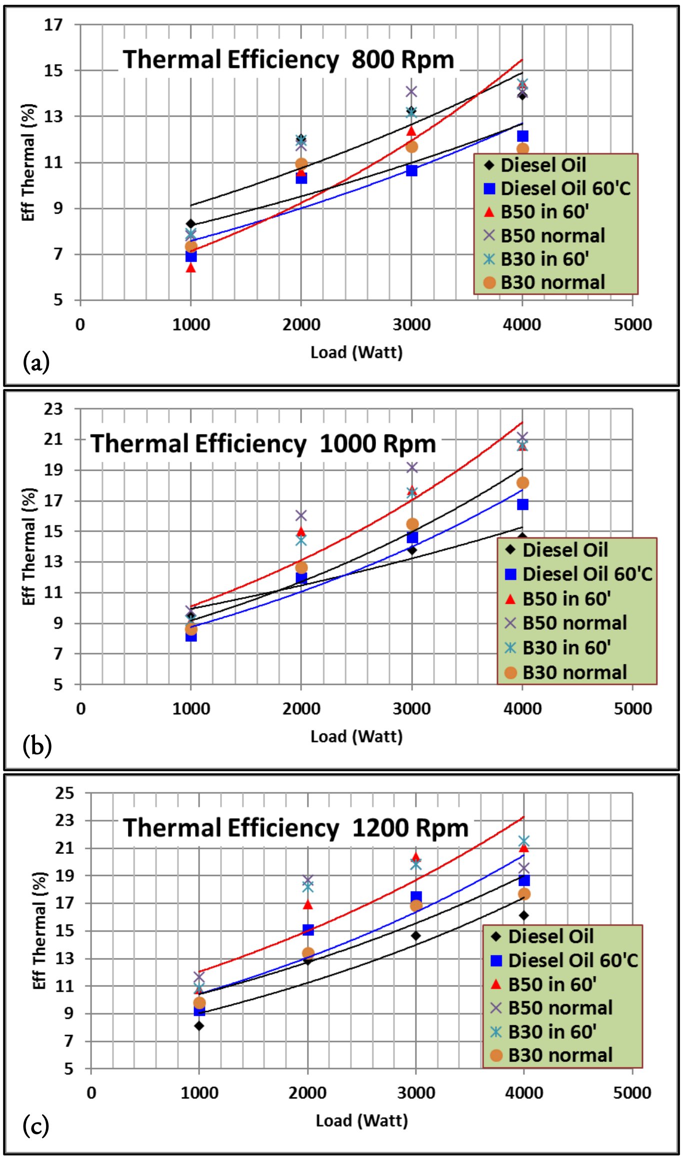

Figure 7. Comparison graph of Thermal Efficiency with Load for each RPM (a) 800 RPM, (b) 1000 RPM, (c) 1200 RPM.

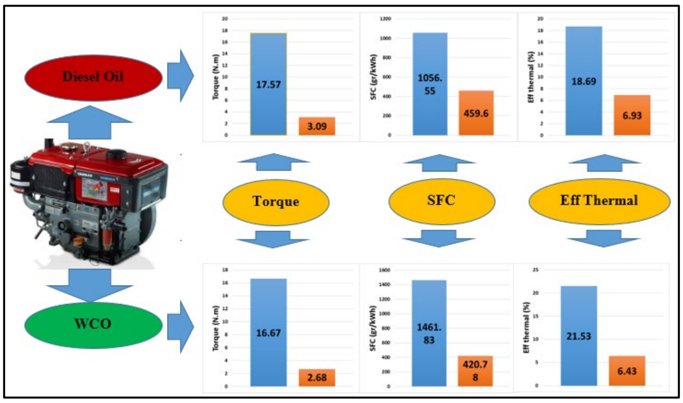

Figure 8. Comparison between torque, sfc, and thermal efficiency between Diesel oil and WCO

Based on the graph presented in Figure 7, it can be inferred that an increase in fuel temperature results in higher thermal efficiency values. This can be attributed to the decrease in fuel density and viscosity, leading to enhanced fuel combustion and improved efficiency. The maximum average thermal efficiency value was recorded for B30 fuel at a temperature of 60 °C across all RPM ranges, at 15.30%, while the minimum was found in diesel fuel at 26 °C, with a value of 11.46%. These findings are consistent with prior research investigating the use of biodiesel derived from palm oil mill effluent (POME), which yielded comparable results, with higher thermal efficiency values recorded for POME biodiesel compared to diesel oil, and an increase in thermal efficiency with increasing fuel temperature (Suardi et al., 2022).

In order for a fuel to be suitable for distribution, it must undergo testing for its properties and engine performance. In this study, B30 and B50 were used and their results were found to be within the standards set by the Biodiesel Specifications set by the Ministry of Energy and Mineral Resources of the Republic of Indonesia, particularly in terms of viscosity and density. Engine testing also showed good performance values in terms of torque, power, SFC, and thermal efficiency. These results suggest that using waste cooking oil (WCO) in biodiesel has potential for further development as a diesel engine fuel in the future.

The addition of WCO biodiesel to diesel fuel oil has an impact on the torque, power, Specific Fuel Consumption (SFC), and thermal efficiency of the diesel engine. The performance of the diesel engine increases with the increase in the blend of biodiesel from WCO to B30. Figure 8 shows that the highest torque value is found in diesel fuel with a temperature of 60 °C at 1200 Rpm with a load of 4000 watts, which is worth 17.57 Nm, while the lowest value is found in B50 fuel at 800 Rpm with a load of 1000 watts at 26 °C, which is 2.68 Nm. The lowest Specific Fuel Consumption (SFC) value is found in B30 fuel with a temperature of 60 °C at 1000 rpm rotation with a load of 4000 watts, which is 439.19 gr/kWh, while the highest SFC value is found in B50 fuel with 26 °C at 800 Rpm with a load of 1000 watts, which is 1461.83 gr/kWh. Meanwhile, the highest thermal efficiency value is found in B50 fuel with a temperature of 60 °C at 1000 rpm rotation with a load of 4000 watts, which is 21.16%, whereas the lowest efficiency value is found in B50 fuel with 26 °C at 800 rpm rotation with a load of 1000 watts, which is 6.43%. Torque and engine power with diesel fuel are still higher than those with WCO fuel, but the SFC and thermal efficiency of engines with WCO fuel are better than those with diesel fuel.

4. CONCLUSION

Based on the engine performance testing, the results indicate that WCO biodiesel can be used as an alternative fuel for diesel engines. B30 and B50 biodiesel properties are still within the standards set by the Ministry of Energy and Mineral Resources of the Republic of Indonesia for biodiesel fuel properties. Fuel temperature variations affect the fuel density and viscosity, with higher fuel temperature resulting in lower density and viscosity values. The density values of diesel fuel oil, B30, and B50 at 26 °C are 0.832 gr/ml, 0.845 gr/ml, and 0.854 gr/ml, respectively, while the viscosity values are 4.01 cSt, 4.53 cSt, and 4.89 cSt. The highest torque value is observed in diesel fuel oil at 60 °C with a value of 17.57 Nm, the lowest SFC value is found in B30 at 60 °C fuel with a value of 439.19 gr/kWh, and the highest thermal efficiency value is found in B50 at 1000 RPM rotation and 60 °C fuel with a value of 21.16%. Therefore, this study demonstrates that WCO biodiesel fuel exhibits better performance in terms of specific fuel consumption and thermal efficiency.

ACKNOWLEDGEMENT

The researcher expresses his gratitude to the ITK Kalimantan integrated laboratory which provides a place for testing engines and fuel properties

REFERENCE

Bernard Freedman, R. O. B. and E. H. P. (1986). Transesterification Kinetics of Soybean Oil. JAOCS, 63(10), 1375–1380. https://doi.org/10.1016/B978-1-893997-62-2.50006-1

Choi, J. Y., Unnikrishnan, U., Hwang, W. S., Jeong, S. M., Han, S. H., Kim, K. H., & Yang, V. (2022). Effect of fuel temperature on flame characteristics of supersonic turbulent combustion. Fuel, 329(March), 125310. https://doi.org/10.1016/j.fuel.2022.125310

Direktorat Jenderal Energi Baru Terbarukan dan Konservasi Energi - Kementerian ESDM. (n.d.). Waste cooking oil: A Promising Energy Business Potential. Retrieved August 1, 2022, from https://ebtke.esdm.go.id/post/2020/12/07/2725/minyak.jelantah.sebuah.potensi.bisnis.energi.yang.menjanjikan

Duhovnik, J. (2008). Journal of Mechanical Engineering: Editorial. Strojniski Vestnik/Journal of Mechanical Engineering, 54(1), 39–46.

Fathallah, A. Z. M., Iswantoro, A., Semin, S., Cahyono, B., Ariana, I. M., & Pratama, A. R. B. (2022). Analysis of The Injection Pressure Effect on Single Cylinder Diesel Engine Power with Diesel Fuel-Methanol Blend. International Journal of Marine Engineering Innovation and Research, 7(2), 50–58. https://doi.org/10.12962/j25481479.v7i2.12884

Fil, H. E., & Akansu, S. O. (2022). The impact of modified injection timing methods on performance , combustion and pollution emissions in CI engine using diesel-gasoline mixtures. Fuel, 328(April), 125268. https://doi.org/10.1016/j.fuel.2022.125268

Hosseinzadeh-Bandbafha, H., Nizami, A. S., Kalogirou, S. A., Gupta, V. K., Park, Y. K., Fallahi, A., … Tabatabaei, M. (2022). Environmental life cycle assessment of biodiesel production from waste cooking oil: A systematic review. Renewable and Sustainable Energy Reviews, 161(March), 112411. https://doi.org/10.1016/j.rser.2022.112411

Indonesia, R. Keputusan Direktur Jenderal Minyak dan Gas Nomor 146.K/10/DJM/2020 Tentang Standar dan Mutu (Spesifikasi) Bahan Bakar Jenis Minyak Solar Yang Dipasarkan Di Dalam Negeri (2020). Retrieved from https://migas.esdm.go.id/uploads/regulasi/regulasi-kkkl/2020/146.K-10-DJM-2020.pdf

Kemenperin: Average Distribution of Bulk Cooking Oil Increased by 800 Tons / Day in March – April 2022. (n.d.). Retrieved August 1, 2022, from https://www.kemenperin.go.id/artikel/23239/Rata-rata-Penyaluran-Minyak-Goreng-Curah-Bertambah-Sebesar-800-TonHari-di

Kementerian ESDM dan Stakeholder Siap Terapkan Standar Euro 4 pada April 2022 | Situs Ditjen Migas. (2021). Retrieved October 18, 2022, from https://migas.esdm.go.id/post/read/kementerian-esdm-dan-stakeholder-siap-terapkan-standar-euro-4-pada-april-2022

Lang, X., Dalai, A. K., Bakhshi, N. N., Reaney, M. J., & Hertz, P. B. (2001). Preparation and characterization of bio-diesels from various bio-oils. Bioresource Technology, 80(1), 53–62. https://doi.org/10.1016/S0960-8524(01)00051-7

Palm Oil Production by Country in 1000 MT - Country Rankings. (n.d.). Retrieved August 1, 2022, from https://www.indexmundi.com/agriculture/?commodity=palm-oil

Panda, K., & Ramesh, A. (2021). Diesel injection strategies for reducing emissions and enhancing the performance of a methanol based dual fuel stationary engine. Fuel, 289(December 2020), 119809. https://doi.org/10.1016/j.fuel.2020.119809

Prasetyo, J., Teknologi, P., Energi, S., & Unpam, J. I. T. K. (2018). STUDI PEMANFAATAN MINYAK JELANTAH SEBAGAI BAHAN BAKU PEMBUATAN BIODIESEL Studi On The Utilization of Used Oil As Raw Material For Biodiesel PENDAHULUAN Sumber energi minyak bumi saat ini mulai menipis seiring meningkatnya pembangunan dan penggunaannya di , 2(2).

Suardi, Purwanto, M., Kyaw, A. Y., Setiawan, W., & Pawara, M. U. (2022). Biodiesel Production from POME (Palm Oil Mill Effluent) and Effects on Diesel Engine Perfor- mance. International Journal of Marine Engineering Innovation and Research, 7(4), 292–299. https://doi.org/10.12962/j25481479.v7i4.14492

Suardi, S. S. (2019). Analisa Penggunaan Biodiesel Minyak Jagung Sebagai Campuran Bahan Bakar Alternatif Mesin Diesel. Inovtek Polbeng, 9(2), 280. https://doi.org/10.35314/ip.v9i2.1041

Suzihaque, M. U. H., Alwi, H., Kalthum Ibrahim, U., Abdullah, S., & Haron, N. (2022). Biodiesel production from waste cooking oil: A brief review. Materials Today: Proceedings, 63, S490–S495. https://doi.org/10.1016/j.matpr.2022.04.527

TF Series | Horizontal Water-cooled Diesel Engines | Industrial Engine | YANMAR Indonesia. (n.d.). Retrieved August 1, 2022, from https://www.yanmar.com/en_id/engine/products/diesel/h_watercooled/tfseries/

Transesterification - SRS BiodieselSRS Biodiesel. (2022). Retrieved October 18, 2022, from https://www.srsbiodiesel.com/technologies/transesterification/

Tschoeke, K. M. H. (2006). Handbook of Diesel Engines. Springer Heidelberg Dordrecht London New York (Vol. 1999).

waste cocking oil - Search | ScienceDirect.com. (2022). Retrieved October 19, 2022, from https://www.sciencedirect.com/search?qs=waste cocking oil

waste cooking oil - Google Scholar. (2022). Retrieved October 19, 2022, from https://scholar.google.com/scholar?hl=en&as_sdt=0%2C5&q=waste+cooking+oil&oq=waste+co

Vol. 14 No. 1 (2023) 40-52

Jurnal Riset
Teknologi Pencegahan Pencemaran Industri

Journal homepage : https://www.jrtppi.id

Kementerian
Perindustrian
REPUBLIK INDONESIA

The Potency of Biodiesel Production from The Local Used Frying Oil Through The Electrocatalysis Method

Haris Numan Aulia[1]*

[1]Polytechnic of Energy and Mineral (PEM) Akamigas, Cepu, Indonesia.

ARTICLE INFO

Article history:
Received September 8, 2022
Received in revised form January 18, 2023
Accepted March 7, 2023
Available online May 02, 2023

Keywords :
Biodiesel
Electrocatalyst
Methanol
Used Frying Oil
Yield

ABSTRACT

The objective of this study was to optimize the operating conditions for an electrocatalytic method of producing biodiesel from local used frying oil (UFO). The effects of electrical voltages (5-30 V), methanol-to-oil molar ratios (4:1-8:1), KOH catalyst concentrations (0.5-1.25% w/w), and electrolysis time (30-120 min) on biodiesel yield were investigated. The highest biodiesel yield of 95.3% was obtained at a voltage of 30 V, methanol-to-oil molar ratio of 6:1, catalyst concentration of 1% w/w, and electrolysis time of 120 min. A regression model was developed to predict the optimum operating conditions, resulting in a maximum biodiesel yield of 95.54%. The predicted optimum operating conditions were a voltage of 24.4 V, methanol-to-oil molar ratio of 5.8:1, catalyst concentration of 1% w/w, and electrolysis time of 120 min. The net profit of the biodiesel business using local UFO as a feedstock was estimated to be IDR 738,000 per month based on a simple economic calculation. These findings demonstrate the potential for using electrocatalytic methods to produce biodiesel from local UFO, and the economic feasibility of producing biodiesel in small-scale industries.

1. INTRODUCTION

The high demand and consumption of fossil fuels around the world have attracted the attention of researchers to look for alternative energy sources because the availability of fossil fuels is decreasing and emissions resulting from the burning of fossil fuels are one of the causes of environmental pollution. Therefore, it is necessary to find alternative energy sources that are renewable, economically competitive, technically feasible, and environmentally friendly. Biodiesel, a renewable alternative liquid fuel derived from triglycerides, is one of the most promising fuels to meet the diesel oil need.

The year 2005 is a crucial year and the beginning of a massive biodiesel research development in Indonesia. At that time, the price of fossil fuels raises more than 100%, which was from 60 to 148 USD per barrel. Furthermore, the Indonesian government is looking for alternative fuels. The government issued the Presidential Regulation Number 5 Year 2006 concerning the national energy policy and Presidential Instruction Number 1 Year 2006 concerning the provision and utilization of biofuels as alternative fuels, thereby further spurring the development of biodiesel research in Indonesia. The government has gradually set the mandatory use of biodiesel in blends with diesel, which are B10 in 2015, B20 in 2018, and B30 in 2020. Furthermore, the government will increase the mandatory use of biodiesel in the coming year with a target of B80 in 2030 which is in line with Indonesia's commitment to reduce greenhouse gas (GHG) emissions by 41% in 2030.

---

*Correspondence author.
E-mail : harisnumanaulia@yahoo.com (Haris Numan Aulia)

doi : https://10.21771/jrtppi.2023.v14.no.1.p40-52

Accreditation number : (Ristekdikti) 158/E/KPT/2021

Biodiesel, containing mono-alkyl esters of long chain fatty acids, is an alternative fuel resulting from vegetable oils or animal fats. It can be used as a fuel for diesel engines. The high price of crude vegetable oil as a raw material for biodiesel can increase production costs. Overall, around 75-90% of the price of biodiesel fuel comes from the purchase of crude vegetable oil. In addition, the use of crude vegetable oil as biodiesel feedstock can increase the cost of the food chain. Therefore, the use of wastes as raw materials for biodiesel can reduce production costs so that it is more effective in the industrialization and commercialization of biodiesel fuel. An increase in biodiesel fuel demand significantly encourages efforts to produce biodiesel from wastes. One of the potential wastes, that can be utilized as a raw material for biodiesel, is used frying oil (UFO). This waste is often dumped directly into the environment by restaurants and other similar facilities.

The selection of biodiesel production technology plays a major role in determining the overall economic feasibility. Therefore, the use of UFO as a biodiesel feedstock can be considered a more economical and sustainable solution. Production of biodiesel from the UFO has been carried out by several researchers through the process of transesterification and acid-catalyzed esterification, heterogeneous base-catalyzed transesterification, transesterification by enzymatic process, transesterification via non-catalyzed subcritical methanol, microwave-assisted transesterification, ultrasonic wave-assisted transesterification, and electrolysis method. The alkaline-catalyzed process has low catalyst and energy efficiencies. The acid-catalyzed process has a low reaction rate and can form by-products. The enzymatic process is expensive. The process via non-catalyzed subcritical methanol is expensive and complicated and requires high pressure and temperature. The microwave-assisted process results in low yields. The ultrasonic wave-assisted process is expensive and cannot be run at room temperature. Compared to the other methods, the electrolysis method has many advantages in which it has lower energy consumption because it can be operated at room temperature, it needs a short reaction time when using co-solvents, it eliminates the waste oil refining and dewatering steps, it reduces water consumption in biodiesel washing, and it produces less waste.

This study employed local used frying oil (UFO) obtained from the Student Dormitory of Vyatra PEM Akamigas (Cepu, Blora, Central Java, Indonesia) as a biodiesel feedstock. As the UFO has not undergone any treatment, it was used as it is in this study. The electrolysis method for producing biodiesel is affected by various factors such as electrical voltage, molar ratio of methanol-to-oil, catalyst concentration, and electrolysis time. Therefore, optimization of the operating conditions is required to enhance the production of biodiesel using local UFO as a feedstock. This study presents a novel approach, as it is the first to optimize the operating conditions in the electrolysis process for producing biodiesel from local UFO. The study aimed to investigate the effect of electrical voltage, molar ratio of methanol-to-oil, catalyst concentration, and electrolysis time on the production of biodiesel using the electrolysis method. Additionally, optimization was carried out to predict the optimal conditions that would result in maximum biodiesel yield using a regression model. A simple economic analysis was performed to estimate the net profit of producing biodiesel from local UFO.

2. METHODS

2.1. Materials

The local UFO was collected from the Student Dormitory of Vyatra PEM Akamigas, in Cepu, Blora Regency, Central Java, Indonesia. Chemicals such as KOH, acetone (99.9%), TetraHydroFuran (99.9%), and methanol (99.9%) were purchased from Merck (Germany).

2.2. Experimental set-up

The equipment used included graphite anode-cathode, magnetic stirrer, hotplate, power direct current (DC) supply, oven, glass beaker, separating funnel, analytical balance, measuring cylinder glass, stative, and clamps. The experimental set-up of the biodiesel production reactor can be seen in the Figure 1.

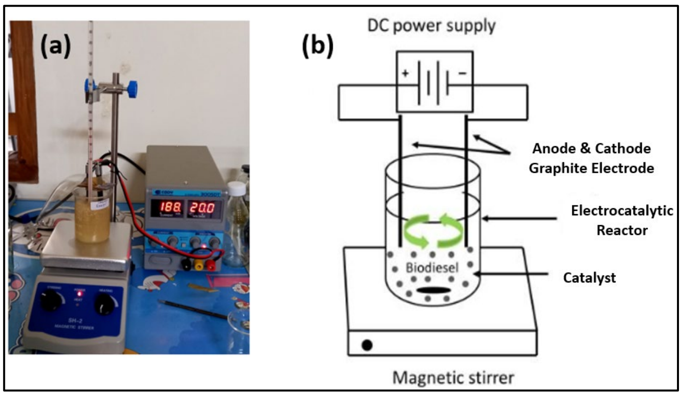

Figure 1. The design of the biodiesel production reactor. (a) a series of tools (b) components that make up the tool.

2.3. *Research procedures*

This research was conducted at the Laboratory of Fundamentals and the Laboratory of Downstream Oil and Gas at PEM Akamigas (Cepu, Blora, Central Java, Indonesia). The local UFO was utilized as the feedstock for biodiesel production via the electrolysis method, which involved variations in electrical voltage, molar ratios of methanol-to-oil, catalyst concentrations, and electrolysis times. Graphite electrodes were employed in the electrolysis process as they are inert. The inter-electrode distance was maintained at 1 cm. The catalyst employed in the process was KOH, which was mixed with CH_3OH until completely dissolved. The research flow chart is presented in Figure 2, which is described in detail in sections 2.3.1 to 2.3.3.

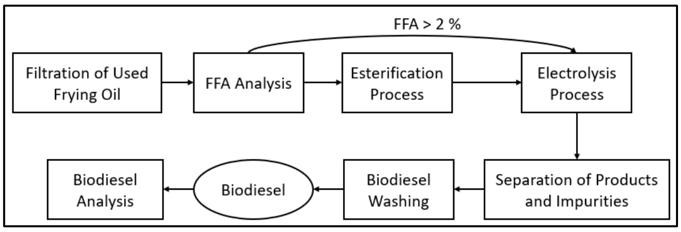

Figure 2. Research Flowchart.

2.3.1. *Preparation of biodiesel feedstock*

Initially, a vacuum filter was assembled, and a filter paper with a diameter of 125 mm was positioned on a buchner funnel. Subsequently, the local UFO was poured into the buchner funnel, and the vacuum pump was switched on until the local UFO screening process was finished. The filtered local UFO was then collected and stored in a bottle.

2.3.2. *Analyzing the feedstock*

5 grams of local UFO and 50 ml of KOH solution were put into the erlenmeyer flask and then stirred. The mixture was heated to 40 oC. Then, 2-3 drops of PP indicator were added. Furthermore, the mixture was titrated with 0.1 N KOH solution until the colour of the mixture turned pink and did not disappear for 30 seconds. Finally, the free fatty acid content (%FFA) of local UFO was calculated using equation (1).

$$\%FFA = \frac{25.6 \times Titrant\ Volume \times Titrant\ Normality}{Weight\ of\ the\ UFO} \quad (1)$$

2.3.3. *Electrolysis process*

First, a solution of KOH (1% w/w oil) was prepared by mixing it with methanol. A solution of acetone (10% w/w oil) was also prepared by mixing it with distilled water (2% w/w oil). Next, 50 grams of local UFO were mixed with the KOH-methanol solution and the acetone-water solution in a beaker glass. The molar ratio of methanol to oil was varied from 4:1 to 8:1. The electrolysis process was carried out at different voltages (5, 10, 20, and 30 V) with an agitation speed of 300 rpm, using graphite electrodes as both cathode and anode. The anode-cathode distance was maintained at 1 cm. The electrolysis process was carried out for 30, 60, 90, and 120 minutes. The resulting biodiesel was separated using a separatory funnel and left to stand for 24 hours. The biodiesel was then washed with hot distilled water at a temperature of 50 °C until the last wash was clean. The water content of the biodiesel was reduced by heating it in an oven at 110 °C for approximately 2 hours. Finally, the yield of biodiesel was calculated.

2.4. *Analysis*

2.4.1. *Free Fatty Acid (FFA)*

Ten grams of the local UFO were placed into a 250 ml Erlenmeyer flask containing 50 ml of 95% ethanol. The mixture was heated to boiling on a hot plate and allowed to cool to room temperature. Next, phenolphthalein was added to the cooled solution for titration with 0.1 N KOH to the equivalence point.

2.4.2. *Kinematic Viscosity*

The kinematic viscosity was carried out by measuring the time required to drain the local UFO in a capillary tube from “a” to “b”. The sample was placed in a viscometer and placed on a thermostat. The liquid was then drawn into the viscometer above the “a” mark using a pump, and allowed to flow down to point “b”. The time taken for the liquid to flow from point “a” to point “b” was recorded using a stopwatch. The viscosity test was conducted at a temperature of 40 °C using an Ostwald viscometer. The principle of the test was to compare the viscosity of the sample with that of a reference fluid, in this case, distilled water (aquadest).

2.4.3. *Density*

Density testing was performed using the measuring cylinder glass method. A clean and empty 10 mL measuring cylinder glass was first weighed, and then 5 mL of the local UFO was added to the cylinder using a digital balance measuring instrument. The density of the local UFO was then calculated.

3. RESULT AND DISCUSSION

The FFA level in the local UFO was 1% (Table 1). If the FFA value < 2%, the esterification process does not required. The esterification process is only needed to reduce the free fatty acid content contained in the raw material because it affects the yield of biodiesel. The results of the local UFO characteristics can be seen in Table 1.

Table 1. Characteristics of the local UFO

Parameters	Values
FFA (%)	1.0
Kinematic Viscosity (cST)	80.55
Density (g/cm^3)	0.912

3.1. *The effect of the electrical voltage*

The increase in electrical voltage in the electrolysis process increased the energy content in the reaction, so the reaction rate increased. The hydroxyl ions (OH-), which were produced during electrolysis, also increased along with the increase in electrical voltage. Methoxide ions can be formed when methanol reacted with the hydroxyl ions, so the higher the electrical voltage, the more the methoxide ions were formed and the more the biodiesel yield was produced. Based on the Figure 3, the highest biodiesel yield was obtained at a voltage of 20 V, which was 95%. When the voltage was increased to 30 V, the biodiesel yield remained at 95% because there was no increase in the OH- ion concentration, so the reaction rate remained constant. Figure 3 shows the biodiesel yield at various electrical voltages, while Figure 4 shows the biodiesel yield obtained at various electrical voltages.

In this study, an increase in electrical voltage can increase the electrical current flowing in the cell. According to previous research, hydroxide ions were continuously formed at the cathode during the electrolysis process. The interaction between hydroxide ions and methanol facilitated the transesterification of the oil, indicating that the oil transesterification reaction occurred near the cathode. Reyero et al reported that biodiesel yield increased with an increase in the OH- ion concentration, but decreased with a decrease in voltage. Results from other studies also showed that increasing the electrolysis voltage led to a significant increase in biodiesel production. Consistent with the result of this study, a previous study reported that the biodiesel yield increased from 88% to 93% with increasing electrolysis voltage from 20 to 40 V. The result of this study was better than the previous study, which might be caused by differences in the free fatty acid contents of the raw materials used.

3.2. *The effect of the molar ratio of methanol-to-oil*

Based on Figure 5, the optimal methanol-to-oil molar ratio is 6:1. Increasing the methanol-to-oil molar ratio from 4:1 to 6:1 resulted in an increase in the biodiesel yield from 93% to 95.1%. However, when the molar ratio was increased to 7:1 and 8:1, the biodiesel yield decreased to 95% and 91%, respectively. Excess methanol acted as an emulsifier, causing some of the biodiesel to enter the water phase during washing, which reduced the biodiesel yield.

The methanol-to-oil molar ratio is one of the most significant factors in biodiesel production. An increase in the ratio has a positive impact on yield during the biodiesel production process. The excess methanol resulted in an increase in the methanol content in the final product. During the settling step, a layer of excess methanol formed on top of the oil. The optimum point of the molar ratio of triglyceride to methanol was found to be 1:6 as not all the methanol added reacted with the triglycerides in the oil. Figure 5 shows the biodiesel yield obtained at different molar ratios of methanol-to-oil, while Figure 6 displays the biodiesel obtained for the variation of the methanol-to-oil molar ratio. Previous research reported that the optimum methanol-to-oil molar ratio was 7:1. When the ratio exceeded 7:1, the electrical conductivity decreased, as the catalyst concentration was determined by the weight of the oil. Furthermore, an increase in the methanol-to-oil molar ratio resulted in a decrease in biodiesel yield, which may be due to the dilution of the oil reactant by methanol. However, other studies reported that a maximum biodiesel yield of 98% was obtained at a molar ratio of methanol-to-oil of 4:1, using a NaOH catalyst concentration of 1% v/v. Similarly, a maximum biodiesel yield of 97% was obtained at a molar ratio of methanol-to-oil of 21:1. The difference in the optimum molar ratio of methanol-to-oil between the previous studies and this study might be due to the different free fatty acid contents in the raw materials used.

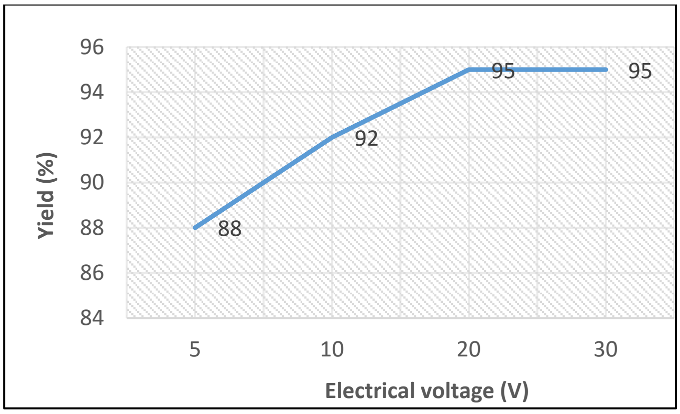

Figure 3. Effect of electrolysis voltages on biodiesel yield. Molar ratio of methanol-to-oil = 6:1, catalyst = 1 %w/w, time = 120 minutes.

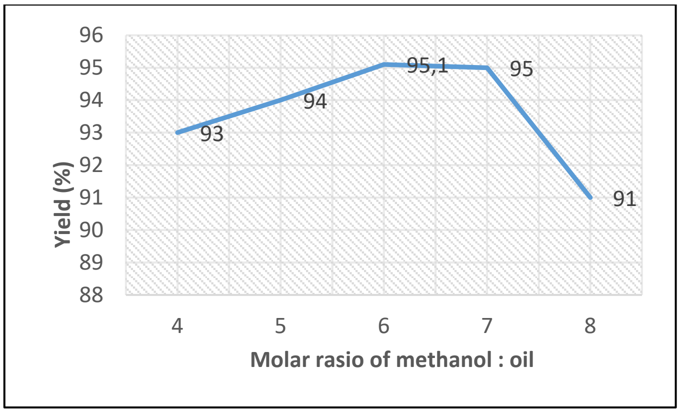

Figure 5. Effect of methanol-to-oil molar ratio on biodiesel yield. Voltage = 20 V, catalyst = 1 %w/w, time = 120 minutes.

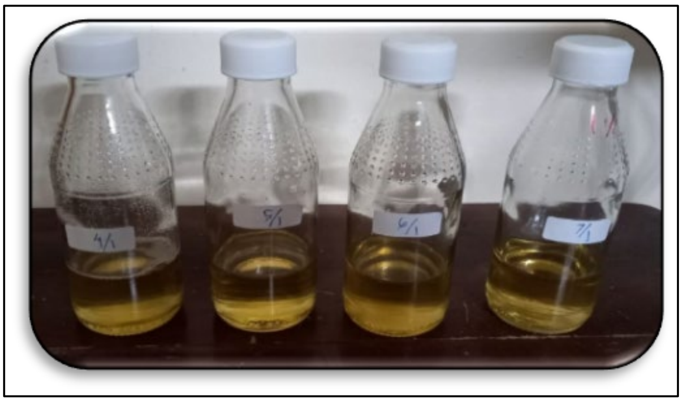

Figure 4. Biodiesel yield at various electrolysis voltages.

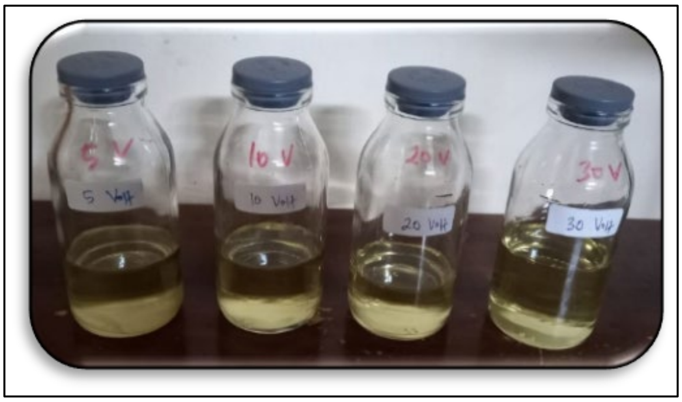

Figure 6. Biodiesel yield at various methanol-to-oil ratios.

3.3. The effect of the catalyst concentration

The transesterification reaction is difficult to occur without the help of a catalyst. The biodiesel yield reaches the optimal value when the KOH concentration is at the right level. The mechanism of transesterification of the local UFO oil with an alkaline catalyst can be seen in Figure 7. The entire process is a series of three reaction sequences and a reversible reaction, in which di- and mono-glycerides are produced as intermediates. The first step (Equation 2) is the reaction between the base and the alcohol, which produces an alkoxide and a protonated catalyst. Nucleophilic attack of the alkoxide on the carbonyl group of the triglyceride produces an intermediate (Equation 3), which results in the formation of an alkyl ester and a triglyceride anion (Equation 4). In the final step, deprotonation of the catalyst occurs, which produces a new active catalyst (Equation 5). The catalyst reacts again with other alcohol molecules until monoglycerides are formed, and undergo the same reaction to produce alkyl esters and glycerol (Schuchardt et al., 1998).

The presence of the KOH catalyst facilitated the reaction to move more quickly towards equilibrium and increased the oil conversion. The catalyst enhanced the solubility of methanol, thereby increasing the reaction rate, leading to an increase in biodiesel production with an increase in the KOH concentration. However, the amount of catalyst had to be optimized to avoid soap formation, as it could cause two problems: reduction of biodiesel yield and difficulty in separating biodiesel from glycerol. According to Figure 8, increasing the catalyst concentration from 0.5 to 1%w/w resulted in an increase in biodiesel yield from 93 to 95%. But, exceeding a catalyst concentration of 1%w/w led to a reduction in biodiesel yield. This was due to an increase in the saponification reaction caused by the catalyst concentrations above 1%w/w. The formation of soap increases the solubility of the produced methyl ester, resulting in the formation of an emulsion between the two phases and increased viscosity of the reactants, leading to difficulties in separating the two phases and reducing the biodiesel yield. Figure 8 shows the biodiesel yield at various concentrations of the KOH catalyst, while Figure 9 shows the biodiesel produced at varying catalyst concentrations. Previous studies reported similar results as this study, where the maximum biodiesel yield was obtained at a catalyst concentration of 1%w/w. Adding more catalysts to the system will cause the unwanted saponification reaction to develop further, reducing the yield. Other previous studies reported the maximum biodiesel yield at a catalyst concentration of 1%w/w using an ultrasonic-assisted reactor with a value of 97.12% and using a microvace-assisted reactor with a value of 90%. Based on the findings of these studies, the presence of ultrasound during the process can increase biodiesel yield. Hence, an ultrasonic-assisted reactor for the local UFO can be employed in the future to enhance biodiesel yield.

In the saponification reaction, triglycerides react with alkali (potassium hydroxide), causing the bonds between the oxygen atoms in the carboxylate group and the carbon atoms in the glycerol to break apart. The oxygen atom then binds to potassium from the potassium hydroxide, causing the end of the carboxylic acid chain to dissolve in water. This potassium salt of the fatty acid is what is then referred to as soap. Meanwhile, the OH group in the hydroxide will bond with the glycerol molecule, and if the three fatty acid groups are released, the saponification reaction is considered complete. Figure 10 illustrates the saponification reaction.

3.4. The effect of electrolysis time

The longer the reaction time, the longer the contact between the catalyst, methanol, and oil, which increases the conversion of oil into biodiesel. The reaction involved in biodiesel production is reversible. Therefore, when the equilibrium is reached, the synthesis process should be stopped to ensure efficient energy use. This is supported by the fact that when the reaction was continued for up to 120 minutes, the biodiesel yield conversion tended to be constant compared to the reaction time of 90 minutes (Figure 11). The yield value was constant because the reversible transesterification reaction had reached an equilibrium state. Figure 11 shows the biodiesel yield at various electrolysis times, while Figure 12 shows the biodiesel produced at various electrolysis times. A previous study [21] also reported that the optimal time to complete the reaction was 120 minutes, so the results of this study corroborate the previous study. Furthermore, another study [15] stated that the maximum biodiesel yield (34.2%) from used frying oil was obtained at a chitosan catalyst concentration of 10%w/w and an electrolysis time of 4 hours, but the yield decreased by 5.1% as the electrolysis time increased to 6 hours. The result of this study was much better than the previous study, which might be due to the different free fatty acid contents in the raw materials used.

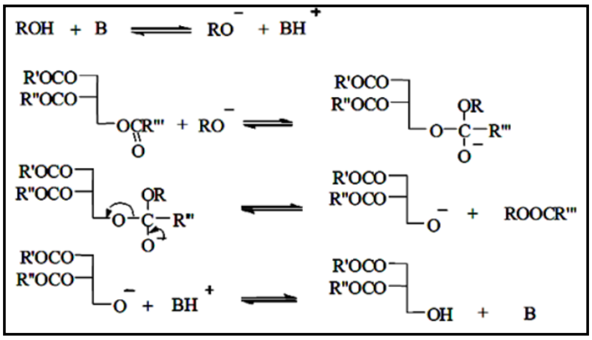

(2)

(3)

(4)

(5)

Figure 7. Reaction Mechanism for the Stage of Biodiesel Formation.

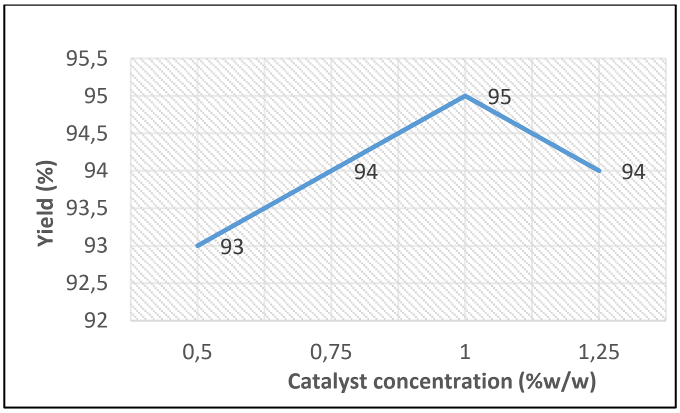

Figure 8. Effect of catalyst concentration on biodiesel yield. Voltage=20 V, Methanol-to-oil = 6:1, time = 120 minutes.

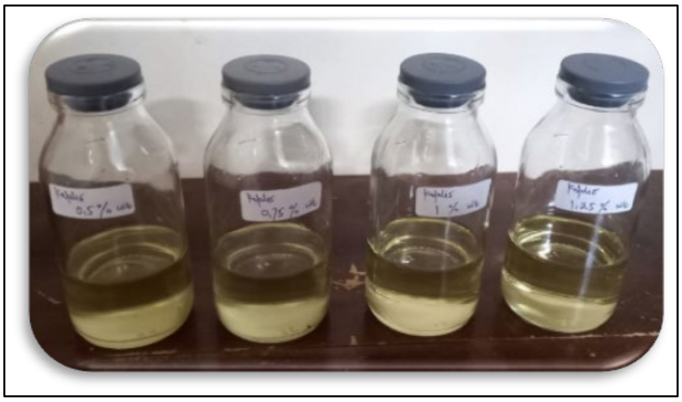

Figure 9. Biodiesel Yield on Variable % wt KOH Catalyst.

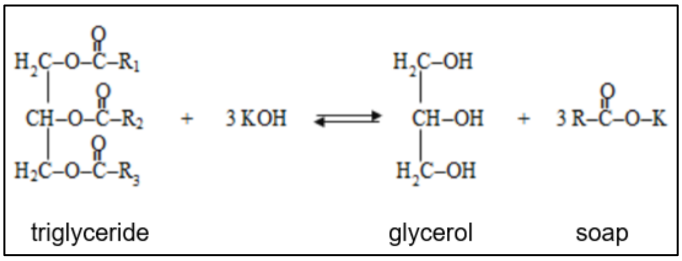

Figure 10. Saponification Reaction.

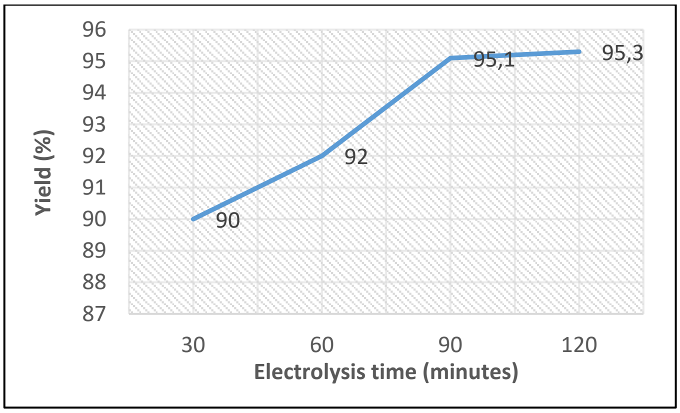

Figure 11. Effect of electrolysis time on biodiesel yield. Voltage = 20 V, Methanol-to-oil = 6:1, catalyst = 1 %w/w.

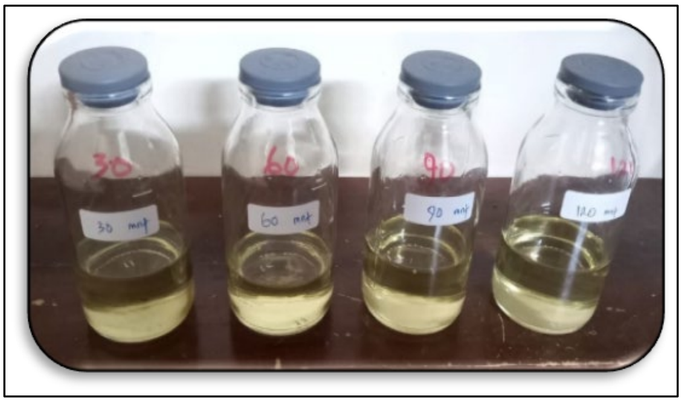

Figure 12. Biodiesel Yield on Variable Electrolysis Time.

3.5. Mathematical model

In this study, four affecting factors in biodiesel production (electrical voltage, methanol:oilmethanol-to-oil molar ratio, catalyst concentration, and electrolysis time) were examined. The summary of the experimental results in this study is shown in the Table 2. The correlation between the affecting factors and the biodiesel yield can be expressed using a regression model. By using the Microsoft Excel software, the regression model was found and written in equation (6).

Table 2. Experimental results

	Electrical voltage (V)	Methanol : oil	Catalyst concentration (%w/w)	Time (minutes)	Biodiesel yield (%)
Run	X1	X2	X3	X4	Y
1	5	6	1	120	88
2	10	6	1	120	92
3	20	6	1	120	95
4	30	6	1	120	95
5	20	4	1	120	93
6	20	5	1	120	94
7	20	6	1	120	95.1
8	20	7	1	120	95
9	20	8	1	120	91
10	20	6	0.5	120	93
11	20	6	0.75	120	94
12	20	6	1	120	95
13	20	6	1.25	120	94
14	20	6	1	30	90
15	20	6	1	60	92
16	20	6	1	90	95.1
17	20	6	1	120	95.3

$$Y = 38.454 + 0.938X_1 + 8.975X_2 + 21.361X_3 + 0.150X_4 - 0.019X_1^2 - 0.772X_2^2 - 11.113X_3^2 - 0.0006X_4^2 \qquad (6)$$

Where :

Y = Biodiesel Yield (%)

X_1 = Voltage (V)

X_2 = Methanol-to-oil molar ratio

X_3 = Catalyst concentration (%w/w)

X_4 = Electrolysis Time (minutes)

The model can predict the biodiesel yield with a high R2 value which was 0.9515. The correlation between the experimental data dan modeled data is shown in the Figure 13. Therefore, the model was very potential to be used to predict the optimum condition in the biodiesel production of the local UFO in this study.

The regression statistics are shown in Table 3. Furthermore, the significance of the model to the biodiesel yield can be determined by the value of "significance F" in Table 4. If the "significance F" value is less than 0.05, then the biodiesel yield is significantly affected by the model presented in equation (6).

Moreover, the test of significance of each factor on the response (biodiesel yield) is shown in Table 5. The factors, having a p-value < 0.05, had a significant effect on the predicted biodiesel yield obtained using the model. Based on Table 5, all factors (X_1, X_2, X_3, X_4) had a p-value < 0.05. It means that all factors were significant in the model in predicting the response (biodiesel yield). The less the p-value, the more significant the factors are. Therefore, the factors of X_1 (electrical voltage) and X_2 (molar ratio of methanol-to-oil) gave more significant effects in the model in predicting the biodiesel yield than the factors of X_3 (catalyst concentration) and X_4 (electrolysis time).

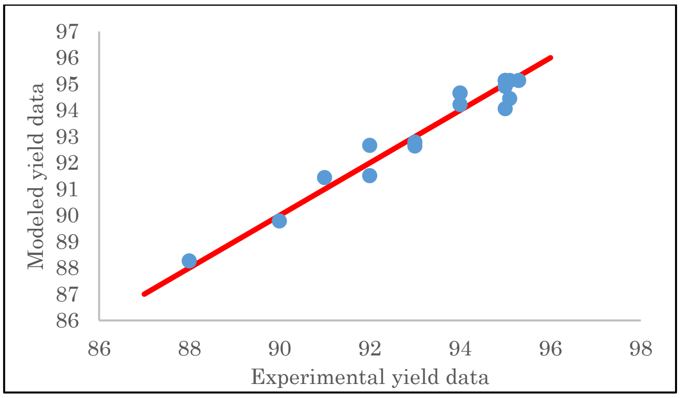

Figure 23. Correlation between the experimental yield data dan modeled yield data

Table 3. Regression Statistic

Multiple R	0.975463
R Square	0.951527
Adjusted R Square	0.903055
Standard Error	0.657417
Observations	17

Table 4. Test of significance of the model on the response (biodiesel yield)

	df	*SS*	*MS*	*F*	*Significance F*
Regression	8	67.87301	8.484126	19.63020303	0.000172
Residual	8	3.457581	0.432198		
Total	16	71.33059			

3.6. Prediction of the optimum conditions

The model shown in the equation (6) was able to make resulted in goodmore accurate predictions compared to the experimental biodiesel data, as shown in the Figure 13. Based on the Table 3, the model resulted in a high R2 value of 0.9515. FurthermoreIn addition, based on the Table 4 demonstrate that the 4, the model can significantly predict the biodiesel yield significantly because it had awith a “significance F“ value < 0.05. Therefore, the model can be confidently utilized to forecast the optimal conditions for maximum biodiesel yield within the constraints presented in Table 6. These constraints were obtained from the minimum and maximum values of each factor examined in this study, as shown in Table 2.

By using the model with the constraints shown in the Table 6, the maximum biodiesel yield was successfully predicted with a help of MS. Excel. The predicted maximum yield was 95.54% which was obtained at optimum conditions of a voltage of 24.4 V, molar ratio of methanol:oilmethanol-to-oil of 5.8:1, a catalyst concentration of 1 %w/w, and an electrolysis time of 120 minutes.

3.7. Economic analysis

Financial analysis or feasibility of biodiesel production from the local UFO was analyzed in this study for small-scale business production. The analysis was based on several assumptions regarding production scale and other factors, and included a summary of the feasibility indicators of small industrial-scale biodiesel production businesses designed by the author. The indicators used were as follows: biodiesel production was calculated based on the local UFO volume per month, with an average price of IDR 3000/L from the collector. The study found that 0.5 L of local UFO can be converted to 0.477 L of biodiesel. 100 L of local UFO was needed per day, or 3000 L per month, to produce 2.862 L of biodiesel per month. The selling price of biodiesel was IDR 9,000/L, with additional income potential from selling glycerol at a price of IDR 20,000/L.

Investment Cost

Investment cost calculation is as follows: Drum (oil storage area) = IDR 200,000. One set of 10 L capacity biodiesel reactor = IDR 8,000,000. Total cost = IDR 8,200,000.

Fixed cost

Fixed costs are costs that must be incurred and the amount is not affected by the number of products produced. Fixed costs for producing biodiesel from used cooking oil are as follows: Electricity = IDR 1.000,000. Manpower (1 man) = IDR 2,500,000. Total cost = IDR 3,500,000.

Variable cost

Variable costs are those whose amount is influenced by the number of products produced. The variable costs are as follows: Cooking oil 100 L @ IDR 3,500 × 30 days = IDR 10,500,000. Potassium hydroxide (KOH) 1 kg @35.000 x 30 days = IDR 2.400,000. Methanol 10 L x @35.000 x 30 days = IDR 10,500,000. Total cost = IDR 23,400,000.

Total production costs

Total production costs = fixed costs + variable costs = IDR 3,500,000 + IDR 23,400,000 = IDR 26,900,000.

Income and Profits

The by-product in the form of glycerol can be another source of income. Biodiesel 2.862 L @ IDR 9,000 = IDR 25,758,000. Glycerol 98 L @ IDR 20,000 = IDR 1,960,000. Total income = IDR 27,718,000.

Profit = Total income – Total production cost = IDR 27,718,000/month – IDR 26,900,000/month = IDR 818,000/month

Business Feasibility Analysis

The business feasibility analysis used the break even point (BEP), and the pay back period (PBP). BEP is utilized to determine the sales volume required for a company to cover all costs and break even without incurring losses or profits. It is achieved when the total production cost is equal to the selling value of biodiesel from used cooking oil. The BEP is formulated as follows: BEP = total production costs per month / selling price per liter = IDR 26,900,000 per month / IDR 9,000 per liter = 2,989 liters per month. The calculated BEP indicates that producers will break even if they sell 2,989 liters of biodiesel per month at a selling price of IDR 9,000 per liter. The estimated PBP value can be calculated to show the payback period for an industrial investment. PBP is the expected time required by the industry to recover the invested capital. An industry is deemed feasible if its PBP value is lower than the project's economic life. PBP can be calculated using the formula: PBP = investment value ÷ profit per month = IDR 8,200,000 ÷ IDR 818,000 per month = 10.02 months.

Table 6. Constraints in optimization

Factors	Minimum	Maximum
Electrical voltage	5	30
Methanol-to-oil molar ratio	4	8
Catalyst concentration	0.5	1.25
Electrolysis time	30	120

Table 5. Test of significance of each factor in the model on the response (biodiesel yield)

	Coefficients	*Standard Error*	*t Stat*	*P-value*	*Lower 95%*	*Upper 95%*
Intercept	38.45409	7.296649	5.27010	0.000755	21.62799	55.2802
X_1	0.938234	0.125629	7.46828	7.1393E-05	0.648533	1.227935
X_2	8.975848	1.653184	5.42943	0.000623761	5.163599	12.7881
X_3	21.36066	7.453212	2.86596	0.020958374	4.17352	38.54779
X_4	0.150728	0.052133	2.89121	0.020161411	0.030509	0.270947
X_1^2	-0.01922	0.003636	-5.2846	0.000742059	-0.0276	-0.01083
X_2^2	-0.77299	0.136672	-5.655	0.000478199	-1.08815	-0.45782
X_3^2	-11.1139	4.328551	-2.5675	0.033252885	-21.0955	-1.13221
X_4^2	-0.00061	0.000323	-1.8858	0.096034088	-0.00135	0.000136

4. CONCLUSION

The local UFO contains triglycerides and FFA content <2%, allowing it to be directly electrolyzed with methanol to produce biodiesel. This study evaluated the effects of various factors on biodiesel yield, including electrical voltage, molar ratio of methanol-to-oil, catalyst concentration, and electrolysis time. Results showed that increasing the voltage from 5 to 20V increased the biodiesel yield from 88% to 95%, but higher voltages did not improve yield. Similarly, an increase in the methanol-to-oil molar ratio from 4:1 to 6:1 increased the yield from 93% to 95.1%, but ratios above 6:1 decreased the yield to 91%. The highest biodiesel yield (95%) was obtained with a 1%w/w KOH catalyst concentration, and using lower or higher concentrations decreased yield. Yield increased with longer electrolysis times, with the highest yield (95.54%) obtained at 120 minutes. The model developed had an R2 of 0.9515, and predicted optimum conditions were a voltage of 24.4 V, a methanol-to-oil molar ratio of 5.8:1, a catalyst concentration of 1%w/w, and an electrolysis time of 120 minutes, resulting in a maximum biodiesel yield of 95.54%. Small-scale production utilizing 300 liters of local UFO per month generated a monthly profit of IDR 818,000.

ACKNOWLEDGMENT

I thank the Research and Community Service Unit of PEM Akamigas Cepu for funding this research. To Mr. Iqbal Syaichurrozi, thank you for your advices in increasing the quality of this article.

REFERENCE

A. A. Hassan and J. D. Smith, “Investigation of microwave-assisted transesterification reactor of waste cooking oil,” Renew. Energy, vol. 162, pp. 1735–1746, 2020, doi: 10.1016/j.renene.2020.09.123.

A. Talebian-Kiakalaieh, N. A. S. Amin, and H. Mazaheri, “A review on novel processes of biodiesel production from waste cooking oil,” Appl. Energy, vol. 104, pp. 683–710, 2013, doi: 10.1016/j.apenergy.2012.11.061.

D. Lauka and D. Blumberga, “Electrolysis Process Analysis by Using Low Carbon Content Additives: A Batch Test Study,” Energy Procedia, vol. 72, pp. 196–201, 2015, doi: 10.1016/j.egypro.2015.06.028.

D. Singh, D. Sharma, S. L. Soni, S. Sharma, P. Kumar Sharma, and A. Jhalani, “A review on feedstocks, production processes, and yield for different generations of biodiesel,” Fuel, vol. 262, no. October, p. 116553, 2020, doi: 10.1016/j.fuel.2019.116553.

D. Widayat, H. N. Aulia, D. Hadiyanto, and S. B. Sasongko, “Kinetic study on ultrasound assisted biodiesel production fromwaste cooking oil,” J. Eng. Technol. Sci., vol. 47, no. 4, pp. 374–388, 2015, doi: 10.5614/j.eng.technol.sci.2015.47.4.3.

E. Kurniawan and N. Nurhayati, “Transesterfication Process of Waste Cooking Oil Catalyzed by Na/CaO Derived from Blood Clam (Anadara Granosa) Shells,” EKSAKTA J. Sci. Data Anal., vol. 1, no. 1, pp. 1–6, 2020, doi: 10.20885/eksakta.vol1.iss1.art1.

E. H. Pryde, “Vegetable oils as diesel fuels: Overview,” J. Am. Oil Chem. Soc., vol. 60, no. 8, pp. 1557–1558, 1983, doi: 10.1007/BF02666584.

F. Cao et al., “Biodiesel production from high acid value waste frying oil catalyzed by superacid heteropolyacid,” Biotechnol. Bioeng., vol. 101, no. 1, pp. 93–100, 2008, doi: 10.1002/bit.21879.

G. Guan and K. Kusakabe, “Synthesis of biodiesel fuel using an electrolysis method,” Chem. Eng. J., vol. 153, no. 1–3, pp. 159–163, 2009, doi: 10.1016/j.cej.2009.06.005.

I. A. Mohammed-Dabo, M. S. Ahmad, A. Hamza, K. Muazu, and A. Aliyu, “Cosolvent transesterification of Jatropha curcas seed oil,” J. Pet. Technol. Altern. Fuels, vol. 3, no. 4, pp. 42–51, 2012, doi: 10.5897/JPTAF11.038.

I. Nurfitri, G. P. Maniam, N. Hindryawati, M. M. Yusoff, and S. Ganesan, "Potential of feedstock and catalysts from waste in biodiesel preparation: A review," Energy Convers. Manag., vol. 74, pp. 395–402, 2013, doi: 10.1016/j.enconman.2013.04.042.

I. Reyero, G. Arzamendi, S. Zabala, and L. M. Gandía, "Kinetics of the NaOH-catalyzed transesterification of sunflower oil with ethanol to produce biodiesel," Fuel Process. Technol., vol. 129, pp. 147–155, 2015, doi: 10.1016/j.fuproc.2014.09.008.

J. J. Lin and Y. W. Chen, "Production of biodiesel by transesterification of Jatropha oil with microwave heating," J. Taiwan Inst. Chem. Eng., vol. 75, pp. 43–50, 2017, doi: 10.1016/j.jtice.2017.03.034.

J. Lie, M. B. Rizkiana, F. E. Soetaredjo, Y. H. Ju, S. Ismadji, and M. Yuliana, "Non-catalytic Transesterification of Waste Cooking Oil with High Free Fatty Acids Content Using Subcritical Methanol: Process Optimization and Evaluation," Waste and Biomass Valorization, vol. 11, no. 11, pp. 5771–5781, 2020, doi: 10.1007/s12649-019-00889-2.

L. C. Meher, D. Vidya Sagar, and S. N. Naik, "Technical aspects of biodiesel production by transesterification - A review," Renew. Sustain. Energy Rev., vol. 10, no. 3, pp. 248–268, 2006, doi: 10.1016/j.rser.2004.09.002.

L. Fereidooni and M. Mehrpooya, "Experimental assessment of electrolysis method in production of biodiesel from waste cooking oil using zeolite/chitosan catalyst with a focus on waste biorefinery," Energy Convers. Manag., vol. 147, pp. 145–154, 2017, doi: 10.1016/j.enconman.2017.05.051.

L. Zhang, Q. Jin, K. Zhang, J. Huang, and X. Wang, "The optimization of conversion of waste edible oil to fatty acid methyl esters in homogeneous media," Energy Sources, Part A Recover. Util. Environ. Eff., vol. 34, no. 8, pp. 711–719, 2012, doi: 10.1080/15567030903567709.

M. Abdollahi Asl, K. Tahvildari, and T. Bigdeli, "Eco-friendly synthesis of biodiesel from WCO by using electrolysis technique with graphite electrodes," Fuel, vol. 270, no. March, p. 117582, 2020, doi: 10.1016/j.fuel.2020.117582.

M. Aghbashlo et al., "Development and evaluation of a novel low power, high frequency piezoelectric-based ultrasonic reactor for intensifying the transesterification reaction," Biofuel Res. J., vol. 3, no. 4, pp. 528–535, 2016, doi: 10.18331/BRJ2016.3.4.7.

M. Tabatabaei et al., "Reactor technologies for biodiesel production and processing: A review," Prog. Energy Combust. Sci., vol. 74, pp. 239–303, 2019, doi: 10.1016/j.pecs.2019.06.001.

M. Tariq et al., "Identification, FT-IR, NMR (1H and 13C) and GC/MS studies of fatty acid methyl esters in biodiesel from rocket seed oil," Fuel Process. Technol., vol. 92, no. 3, pp. 336–341, 2011, doi: 10.1016/j.fuproc.2010.09.025.

O. Babajide, "Novel zeolite Na-X synthesized from fly ash as a heterogeneous catalyst in biodiesel production," Catal. Today, vol. 201, no. 1, p. 210, 2013, doi: 10.1016/j.cattod.2012.09.006.

R. Betha, S. Pavagadhi, S. Sethu, M. P. Hande, and R. Balasubramanian, "Comparative in vitro cytotoxicity assessment of airborne particulate matter emitted from stationary engine fuelled with diesel and waste cooking oil-derived biodiesel," Atmos. Environ., vol. 61, pp. 23–29, 2012, doi: 10.1016/j.atmosenv.2012.06.086.

R. S. Putra, P. Hartono, and T. S. Julianto, "Conversion of Methyl Ester from Used Cooking Oil: The Combined Use of Electrolysis Process and Chitosan," Energy Procedia, vol. 65, pp. 309–316, 2015, doi: 10.1016/j.egypro.2015.01.057.

R. S. Putra, A. Liyanita, N. Arifah, E. Puspitasari, Sawaludin, and M. N. Hizam, "Enhanced Electro-Catalytic Process on the Synthesis of

FAME Using CaO from Eggshell," Energy Procedia, vol. 105, no. May, pp. 289–296, 2017, doi: 10.1016/j.egypro.2017.03.316.

S. Hama, A. Yoshida, N. Tamadani, H. Noda, and A. Kondo, "Enzymatic production of biodiesel from waste cooking oil in a packed-bed reactor: An engineering approach to separation of hydrophilic impurities," Bioresour. Technol., vol. 135, pp. 417–421, 2013, doi: 10.1016/j.biortech.2012.06.059.

S. Rezania et al., "Review on transesterification of non-edible sources for biodiesel production with a focus on economic aspects, fuel properties and by-product applications," Energy Convers. Manag., vol. 201, no. October, p. 112155, 2019, doi: 10.1016/j.enconman.2019.112155.

W. P. Wicaksono, S. A. Jati, I. Yanti, and P. K. Jiwanti, "Co-Solvent Free Electrochemical Synthesis of Biodiesel Using Graphite Electrode and Waste Concrete Heterogeneous Catalyst: Optimization of Biodiesel Yield," Bull. Chem. React. Eng. Catal., vol. 16, no. 1, pp. 179–187, 2021, doi: 10.9767/bcrec.16.1.10310.179-187.

Y. Zhang, M. A. Dubé, D. D. McLean, and M. Kates, "Biodiesel production from waste cooking oil: 2. Economic assessment and sensitivity analysis," Bioresour. Technol., vol. 90, no. 3, pp. 229–240, 2003, doi: 10.1016/S0960-8524(03)00150-0.

9 772503 501001

9 772087 096504